VII International Pontecorvo Neutrino Physics School

Proceedings

of the Student Poster Session

Edited by F. Šimkovic

JOINT INSTITUTE FOR NUCLEAR RESEARCH

VII INTERNATIONAL PONTECORVO NEUTRINO PHYSICS SCHOOL

Prague, Czech Republic
August 20 – September 1, 2017

Proceedings of Student Poster Session

Edited by F. Šimkovic

УДК 539.123(063)539.1.07(063)
ББК 22.382.4я431
22.381.5я431
I69

The financial support was provided by grants of the JINR Directorate and the Plenipotentiaries of the Governments of the Czech Republic and Romania, by the programme of cooperation between JINR and Comenius University in Bratislava, and by IEAP CTU in Prague, and by European Regional Development Fund-Project No. CZ.02.1.01/0.0/0.0/16_013/0001733.

Composed by *A. Babič* and *A. V. Malykh.*

Title page design by *A. V. Malykh.*

The contributions are reproduced directly from the originals presented by the Organizing Committee.

VII International Pontecorvo Neutrino Physics School (Prague, Czech I69 Republic, August 20 – September 1, 2017): Proceedings of Student Poster Session / Ed. F. Šimkovic. — Dubna: JINR, 2018. — 177 p.; 11 p. of photos.

ISBN 978-5-9530-0484-8

The VII International Pontecorvo Neutrino Physics School, which was organized by the Joint Institute for Nuclear Research in Dubna, Institute of Experimental and Applied Physics, Czech Technical University in Prague, Charles University in Prague, Comenius University in Bratislava, and Institute of Nuclear Physics in Krakow, was held at the Conference Hall of the National Library of Technology (Prague) on August 20 – September 1, 2017.

The School covered a broad range of topics in neutrino physics and neutrino cosmology. The purpose of the School was to review the present status of experimental and theoretical neutrino physics. 22 outstanding lecturers drew attention of 65 students and young scientists to prominent neutrino physics experiments and unsolved problems concerning fundamental properties and interactions of neutrinos. Three evening discussion sessions were organized covering the problems of oscillation mechanism, the effect of matter, and the nature of neutrino masses. 33 students and young scientists presented results of their research during the Student Poster Session, 22 of them contributed to this Proceedings.

УДК 539.123(063)539.1.07(063)
ББК 22.382.4я431
22.381.5я431

ISBN 978-5-9530-0484-8

Organizing Committee

Chairman:

V.A. Matveev (JINR Dubna)

Scientific program:

S.M. Bilenky (JINR Dubna)

Vice-chairmen:

I. Štekl (IAEP CTU, Prague)
A.G. Olshevskiy (JINR Dubna)
F. Šimkovic (Comenius U., Bratislava/JINR Dubna)
M. Jeżabek (INP Krakow)

Members:

V.A. Bednyakov (JINR Dubna)
R. Leitner (Charles U., Prague)
A. Zalewska (INP Krakow)
V.B. Brudanin (JINR Dubna)
E.A. Kolganova (JINR Dubna)

Secretaries:

R. Hodák (IAEP CTU, Prague)
E. Rusakovich (JINR Dubna)
E. Rukhadze (IAEP CTU, Prague)
M. Vanišová (IAEP CTU, Prague)

VII International Pontecorvo Neutrino Physics School (group photo)

Contents

PREFACE

GENERAL INFORMATION

The VII International Pontecorvo Neutrino Physics School continued the tradition of Pontecorvo Neutrino Physics Schools, which were held in Dubna, Alushta and Horný Smokovec in 1998, 2003, 2007, 2010, 2012 and 2015. The information about all editions of the Pontecorvo neutrino schools can be reached through the web site `http://pontecorvosch.jinr.ru`.

The Schools are named after a prominent scientist, Bruno Pontecorvo (called Mr. Neutrino), who is well known for his important contributions to the world science. Bruno Pontecorvo was working in Dubna within the period 1950–1993, where in 1957 suggested the idea of neutrino oscillations, a phenomenon which was experimentally discovered about 40 years later and which remains one of the most intriguing subjects of the modern particle physics nowadays.

The compelling evidence for neutrino oscillations caused by small masses and mixing of neutrinos has opened new windows for further fundamental discoveries in the field of neutrino physics, astroparticle physics and cosmology. It might be that we are close to exclusive research findings concerning absolute mass scale of neutrinos, type of neutrino mass hierarchy, CP-violation in the lepton sector and the problem of the nature, Dirac or Majorana, of massive neutrinos. The observation of tiny masses of neutrinos and lepton mixing constitutes the first confirmed evidence for physics beyond the Standard Model and plays key role in development of the particle physics theory. The interest to neutrino physics is growing and bringing young people to the field.

The purpose of the school was to review the present experimental and theoretical situation in neutrino physics. The lecture courses at the school were given by the world's experts and included phenomenology and theory reviews, discussion of experimental results and future program in the field of massive neutrinos.

PRESENT SCHOOL

The VII Pontecorvo Neutrino Physics School was held in Prague, Czech Republic, one of the most beautiful cities in Europe, within a period August 20 – September 1, 2017 (`http://theor.jinr.ru/~neutrino17/`).

The VII Pontecorvo Neutrino Physics School covered a broad range of topics in neutrino physics, astroparticle physics and cosmology. The purpose of the School was to review the present status of experimental and theoretical neutrino physics. In total the School accepted 92 participants including 22 lecturers, 65 PhD students and young scientists from countries around the world. The priority for participation in the school was given to the applicants with a strong neutrino physics background and interests.

ORGANIZERS

The VII Pontecorvo Neutrino Physics School was organized by Joint Institute for Nuclear Research in Dubna (JINR Dubna), Institute of Experimental and Applied Physics, Czech Technical University in Prague (IEAP CTU, Prague), Charles University in Prague (Charles U., Prague), Comenius University in Bratislava (Comenius U., Bratislava) and Institute of Nuclear Physics in Krakow (INR Krakow).

The financial support was provided by grants of the JINR Directorate and the Plenipotentiaries of the Governments of the Czech Republic and Romania, by the programme of cooperation between JINR and Comenius University in Bratislava, IEAP CTU in Prague, and by European Regional Development Fund-Project No. CZ.02.1.01/0.0/0.0/16_013/0001733.

VENUE

The venue of the School was the Conference Hall of the Czech National Library of Technology (Czech: Národní Technická Knihovna, abbreviated as NTK). The building also houses a branch of the Municipal Library of Prague. The former site of the National Library of Technology was the Clementinum in the Old Town of Prague, from which all books and materials were moved to the library's current location after completion of the current building in 2009. The building was designed by architects Roman Brychta, Adam Halíř, Ondřej Hofmeister and Petr Lešek after winning first prize in an architectural competition held in 2000. Construction of the current building began in 2006 and was completed in January 2009. The library opened to the public on 9 September 2009 and now boasts the most extensive collection of Czech and international documents in the field of technology and applied natural and social sciences related to technology in the Czech Republic. Address: Technická 2710/6, 160 80 Praha 6, Czech Republic. It is situated in a walking distance to the Masaryk College, where participants of the School were accommodated.

PROGRAM OF THE SCHOOL

In the formation of the Pontecorvo School programmes, much credit goes to Samoil Bilenky, an outstanding expert and international authority in neutrino physics, well acquainted with the subject and the scientists working in all fields related to neutrinos. He is not only the founder of the School but also its permanent organizer, the scientific programme supervisor, and excellent lecturer.

Program of the School covered modern topics of neutrino physics, astroparticle physics and cosmology:

- Theory of neutrino mixing and masses
- Solar, atmospheric, reactor and geo neutrino experiments
- Direct neutrino mass measurements
- Neutrinoless double-beta decay (theory and experiment)
- Neutrino-nucleus interactions
- Sterile neutrinos
- Neutrino cosmology and astronomy
- Dark matter
- Leptogenesis and baryogenesis

- Gravitational waves
- Statistics for nuclear and particle physics

LECTURERS AND LECTURES AT THE SCHOOL

During 9 working days outstanding lecturers from the field of neutrino physics, astroparticle physics and cosmology drew attention of the students and young scientists to prominent neutrino physics experiments and unsolved problems concerning fundamental properties and interactions of neutrinos.

The next day after the opening of the School, August 22, marked the 104^{th} birthday of Bruno Pontecorvo. A special session was held in memory of this outstanding scientist, where the participants watched the film about Bruno Pontecorvo, and Samoil Bilenky shared his memories about this man, whose scientific achievements and human qualities largely affected the currently formed image of Dubna, JINR, and world science.

- Samoil Bilenky (JINR, Dubna)
  Introduction to Neutrino
- Boris Kayser (Fermilab, Batavia)
  Neutrino Oscillation Phenomenology
- Gary Feldman (Harvard Univ., Cambridge)
  Long-Baseline Neutrino Oscillation Experiments
- Alexei Smirnov (MPI, Heidelberg)
  Solar Neutrinos: Theory and Experiment
- Barry Barish (Caltech, Pasadena)
  Gravitational Waves
- Igor Tkachev (INR, Moscow)
  Measuring of Neutrino Mass with Tritium Beta Decay
- Steve King (Univ. of Southampton)
  Theory of Neutrinos, Masses and Mixings
- Yifang Wang (IHEP, Beijing)
  Reactor Neutrino Experiments
- Carlo Giunti (INFN, Torino)
  Oscillations beyond Three-Neutrino Mixing (Light Sterile Neutrinos)
- Jonathan Link (Virginia Tech, Blacksburg)
  Hunting for Sterile Neutrinos
- Nicolao Fornengo (Univ. of Torino/INFN, Torino)
  How Dark is Dark? How to Unveil the Hidden Nature of Dark Matter
- Gianpiero Mangano (INFN, Naples)
  Topics in Neutrino Cosmology
- Sacha Davidson (IPN de Lyon)
  Of Cookbooks and Fairy Tales: How Neutrinos Could Make the Universe We See
- Loredana Gastaldo (Kirchhoff Inst. for Physics, Heidelberg)
  Electron-Neutrino Mass Determination Using ^{163}Ho *Electron Capture*

- Alexander Barabash (ITEP, Moscow)
  Neutrinoless Double-Beta Decay Experiments
- Christian Spiering (DESY, Zeuthen)
  High-Energy Neutrino Astronomy
- Irene Tamborra (Niels Bohr Inst., Univ. of Copenhagen)
  Supernova Neutrinos
- Petr Vogel (Caltech, Pasadena)
  I. Neutrinoless Double-Beta Decay. What Its Observation Would Prove, and Its Nuclear Matrix Elements
  II. Spectra of Neutrinos from Reactors: Issues and Challenges
- David A. van Dyk (Imperial College, London)
  Statistical Quantification of Discovery in Physics
- Jan T. Sobczyk (Wrocław Univ.)
  Neutrino Interactions
- Eckhard Elsen (CERN, Geneva)
  CERN Physics Programme and Neutrinos
- Alain Blondel (Univ. of Geneva)
  Future Facilities

The highlight of the School programme were two lectures on the discovery of gravitational waves delivered by Barry Barish (Caltech). A month later he and his two col-

leagues have been awarded the 2017 Nobel Prize in Physics for this discovery. Currently, the Pontecorvo School can boast having two Nobel Prize winners among its lecturers. The 2015 Nobel Prize in Physics awarded for the discovery of neutrino oscillations, which shows that neutrinos have mass, went to Takaaki Kajita (University of Tokyo), who talked about those results in his lecture on physics of atmospheric neutrinos in Alushta in 2007.

Three evenings the participants were invited to freely take part in discussion sessions at which lecturers together with the students thoroughly examined the oscillation mechanism, the effect of matter, and the nature of neutrino masses. These events were found very useful to stimulate vitality for discussion, dialogue and debate on the topic covered.

PARTICIPANTS:

Among 65 participants (not including 22 lecturers and 5 members of organizing committee), there were 14 young scientists from JINR and Russia, 24 from the JINR Member States (Poland, Romania, Slovakia, Czech Republic), 20 from European countries (UK, Germany, Denmark, Spain, Portugal, France, Switzerland), and 7 from China, the United States, Turkey, and Chile. This year not only 48 postgraduates, 10 Masters, and 3 Bachelors but also 4 postdoctoral scientists took an interest in the School.

ACCOMMODATION:

Accommodation of students and young scientists was organized at the Masaryk College (Czech: Masarykova Kolej) owned by the Czech Technical University in Prague.

The Masaryk College is situated in a strategic location in Dejvice, Prague 6, just 20 minutes away from the international Václav Havel Airport Prague, with excellent public-transport access to the city center, and with good motorway links.

The Masaryk Dormitory was founded in 1925, thanks to moral and financial support provided by Tomáš Garrigue Masaryk, the first president of Czechoslovakia. It was built according to the design of Antonín Engel in Sadová Street, nowadays called Thákurova Street, in parallel with the preparations for constructing the adjacent campus of the Czech Technical University in Prague (www.cvut.cz).

POSTER SESSION:

At a special session, 33 participants presented their poster reports. Twenty-two of them contributed to this Proceedings of the student poster session.

EXCURSION

The School programme included a day-off for getting acquainted with Prague, one of the most beautiful towns in Europe. In addition, the participants were offered historical excursions to Kutná Hora, a medieval silver-mining town with one of the most beautiful Gothic cathedrals in the country, and Český Krumlov (a designated UNESCO World Heritage Site), one of the undoubted gems of Southern Bohemia.

SUMMARY

By all accounts the school was a great success. The lecturers and students reported a high level of satisfaction with the school. In particular, students were very enthusiastic both in terms of outstanding lecturers, beautiful location, excellent venue, very professional organization and on social interaction and networking among participants. The unanimous opinion of the participants was that the School clearly manifested the raising significance of neutrino physics research and achievements within physical community and human society. The results and the opinions of the participants indicate that the sci-

entific programme of the School, its format, and lecturer membership keep improving, becoming more and more attractive for young scientists.

The JINR neutrino programme was well presented at the School and attracted a lot of attention of all participants. Due to its excellence it is a basement for a fruitful collaboration of the Czech Republic, Slovakia, Romania, Poland and other countries with the JINR Dubna in this field.

THE NEXT EDITION OF PONTECORVO SCHOOL

The School geography grows wide: the first School was held in Dubna; the next four, in its twin city Alushta in the Crimea (`http://pontecorvosch.jinr.ru`); the sixth School moved to Horný Smokovec, High Tatras mountain region of Slovakia (`http://theor.jinr.ru/~neutrino15/`) and the seventh School was held in Prague, the capital of the Czech Republic (`http://theor.jinr.ru/~neutrino17/`). The next VIII Pontecorvo Neutrino Physics School in Romania is scheduled for the summer or fall 2019, and the preparation of its scientific programme is well under way.

Bruno Pontecorvo: Pioneer of Neutrino Oscillations

S. M. Bilenky

JINR Dubna

Figure 1. Bruno Pontecorvo (B. P.).

Bruno Pontecorvo (B. P.) was born on August 22, 1913, in Pisa (Marina di Pisa), Italy. His father was an owner of a textile factory founded by Pellegrino Pontecorvo, Bruno's grandfather. After the war, for many years the factory was closed and the building was not used. Today, it is a home to the Pisa department of INFN. The square in front of the building is called *Largo di Bruno Pontecorvo.* There were eight children in the family: five brothers and three sisters, all of them were very successful. Guido (the eldest brother) became a famous biologist, Bruno became a famous physicist and Gillo was a very well known film director.

B. P. joined the Faculty of Engineering at the University of Pisa. He had good marks, but he did not like mechanical drawing. After two years, he decided to study physics. From his autobiography: *My brother Guido declared authoritatively: "Physics! I would like to say that you must go to Rome. In Rome there are Fermi and Rasetti."* B. P. passed an exam with Fermi and Rasetti. After the exam, Fermi made the following remark: *"While there is only one physics, today's physicists are divided into two categories: theorists and experimentalists. If a theorist is not gifted with extraordinary abilities, his work is pointless. As to the experimental physics, there are opportunities for some useful work even for an averagely skilled individual."* B. P. was accepted to the Faculty of

Figure 2. **Left panel**: B. P. with wife Marianna and first-born son Gil (Paris, 1940).
Right panel: B. P. with brother Gillo (Moscow, 1961).

Physics and Mathematics at the University of Rome with specialization in experimental physics. First as a student and later as a researcher, from 1931 till 1936 B. P. worked in the Fermi group (famous *gruppo dei "ragazzi di via Panisperna"*) with Fermi, Rasetti, Amaldi and Segrè.

In 1934, Amaldi and B. P. performed a series of experiments aimed at the measurement of radioactivity of different elements irradiated by neutrons. They observed that if the distance between the source and the detector is small and both are enclosed in lead, some irregularities occurred; in particular, the inverse-square law $1/r^2$ was not valid. Amaldi and B. P. were sure that this effect had something to do with the lead. They told about their results to Rasetti and Fermi; Rasetti did not believe the results and Fermi did not seem much interested. In fact, this impression was wrong. Fermi had been thinking about the anomalies and a few days later he proposed to perform an experiment with paraffin (and water) placed between the source and the detector. The effect was enormous: radioactivity was hundreds of times larger than before. When they discovered this effect, Fermi stopped the excitement of his colleagues and said a famous phrase: *"Let's go and have a lunch."* After the lunch, Fermi explained everything: this effect was due to the slowing down of neutrons caused by their scattering on protons in the paraffin (water). B. P. remembered that Fermi said: *"How stupid of us to have discovered this phenomenon by chance and not having been able to predict it!"* The effect of slowing down of neutrons opened the road to all applications of neutrons (reactors, radioisotopes in medicine, atomic bombs). Professor Corbino convinced the group (E. Fermi, E. Amaldi, B. P., E. Segrè, F. Rasetti, and D'Agostino) to secure a patent for this invention.

In 1936, B. P. received a prize of the Italian Ministry of Education and went for Paris to work with F. Joliot-Curie. In Paris, he studied nuclear isomers, i.e., metastable nuclear states with high spins. He performed the first experiments aimed at the observation of conversion electrons in decays of isomers, produced nuclear isomers in process of the

irradiation of nuclei by high-energy photons (nuclear phosphorescence), etc. For the study of the nuclear isomerism, B. P. was awarded the Curie-Carnegie prize. Fermi congratulated B. P. with excellent results, which made him very happy and proud (he joked that Fermi, who usually called him a great champion, had respect to him only as a tennis expert). In 1940, before the Germans occupied Paris, B. P. escaped together with his family (wife and son) to US. From 1940 till 1942, he worked in a private oil company in Oklahoma. He developed a method of neutron well logging for oil (and water) prospering. This was the first practical application of neutrons. The method of neutron well logging is widely used nowadays. In 1943, B. P. took the position of a researcher in the Anglo-Canadian Uranium Project in Canada (first, in Montreal Research Laboratory and afterwards in the Chalk River Laboratory). He was a scientific leader of the project of the research reactor which was built in 1945 and was the first nuclear reactor outside of USA.

While in Canada, B. P. started his research in the elementary particle physics. Soon after the publication of the famous Fermi's paper on the theory of the β decay (1934), Bethe and Pierls estimated the cross section of the interaction of the postulated by Pauli neutrino with a nucleus. The estimated cross section was extremely small; at $\sim$ MeV energies: $\sigma < 10^{-44}\,\mathrm{cm}^2$. For many years the neutrino was considered an "undetectable particle."

B. P. was the first physicist who challenged this opinion. He proposed the first method of neutrino detection [1] (Canada, 1946), based on the observation of the decay of daughter nucleus produced in the reaction: $\nu + (A, Z) \longrightarrow e^- + (A, Z+1)$. As the most promising he considered the process $\nu_e + {}^{37}Cl \longrightarrow e^- + {}^{37}Ar$, which has the following advantages:

- C_2Cl_4 is a cheap, non-inflammable liquid.
- ${}^{37}Ar$ nuclei are unstable (K-capture) with a convenient half-life (34.8 days).
- A few atoms of ${}^{37}Ar$ (rare gas), produced during the exposition time, can be extracted from a large detector.
- K-capture is accompanied with the energy release of 2.8 keV. This gives a possibility to use low-background proportional counters.

The B. P. *Cl-Ar* radiochemical method was exploited by R. Davis in the first experiment on the detection of solar neutrinos. In 2002, R. Davis was awarded the Nobel Prize for the discovery of solar neutrinos. Furthermore, the radiochemical method of neutrino detection based on observation of the reaction $\nu_e + {}^{71}Ga \longrightarrow e^- + {}^{71}Ge$, proposed by V. Kuzmin, was used in the GALLEX/GNO and SAGE solar neutrino experiments in which the most abundant pp neutrinos were detected.

In order to detect neutrinos, it was necessary to find intensive sources. In the seminal Chalk-River paper [1], B. P. for the first time paid attention to the following sources: the Sun, the nuclear reactors, and the radioactive materials produced inside the reactors. In 1948, B. P. invented the low-background proportional counter with high amplification. This counter proved crucial for the detection of solar neutrinos in the Homestake (Davis), GALLEX and SAGE experiments.

After the famous Conversi–Pancini–Piccioni experiment (1947), from which it followed that the muon weakly interacts with nuclei, B. P. together with E. Hincks started a


Figure 3. **Left panel**: B. P. with N. S. Isaeva and B. G. Kadyshevskij (Dubna, 1964).
Right panel: B. P. with sons Tito (left) and Antonio (Dubna, 1960s).

series of brilliant pioneering experiments on the investigation of the fundamental properties of muon. They proved that:

1. The charged particle emitted in the muon decay is an electron.
2. The muon decays into three particles.
3. The muon does not decay into an electron and a photon.

B. P. suggested that the muon is a particle with spin $1/2$ and the muon capture by a proton is accompanied by an emission of a neutrino: $\mu^- + p \longrightarrow \nu + n$. B. P. was the first to pay attention to the deep analogy between the electron and muon [2]. He compared the probabilities of the processes: $\mu^- + (A, Z) \longrightarrow \nu + (A, Z-1)$ and $e^- + (A, Z) \longrightarrow \nu + (A, Z-1)$, and concluded that the coupling constants which characterize the strength of these two processes are of the same order of magnitude: *"There is a fundamental analogy between the β processes and the absorption of muons."* Thus, in 1947, B. P. came to the idea of universal weak interaction of e-ν and μ-ν pairs. Later, the idea of e-μ universality was proposed by Puppi, Klein, Tiomno and Wheeler.

In 1950, B. P. moved with his family (wife and three sons) from England to USSR. He started to work in Dubna, which at that time hosted the largest accelerator in the world (460 MeV, later upgraded to 680 MeV). Together with his group, he performed experiments on the investigation of the production of π^0 mesons in neutron-proton and neutron-nucleus collisions, on the pion-nucleon scattering, etc.

B. P. was always thinking about the neutrino. Towards the end of the 1950s, in Dubna there was a project of a meson factory which, however, was never realized. In connection to this project, B. P. contemplated the feasibility of neutrino experiments with neutrinos originating from the decays of pions and kaons produced in high-intensity accelerators. At that time, the reactor neutrinos had been detected in the famous Reines and Cowan experiment. B. P. came to the conclusion that experiments with accelerator neutrinos are possible (independently, M. A. Markov and M. Schwartz came to the same conclusion). B. P. started to think about fundamental problems of neutrino physics which could be solved in such experiments. He always remembered that people who had worked with muons in the early days had in mind that neutrinos which is produced together with muon and electron could be different.

In 1958, Feinberg showed that if ν_e and ν_μ are identical, the probability of the process: $\mu \longrightarrow e + \gamma$, calculated within the theory with W-boson and cut-off, should be many orders of magnitude higher than the existed at that time upper bound. B. P. was the first who understood that the experiments with high-energy neutrinos from the $\pi \longrightarrow \mu + \nu_\mu$ decays allow to probe the existence of the second type of neutrino in a direct, model-independent way [3]. His proposal was realized in the famous Brookhaven experiment (1962) which proved that: $\nu_\mu \neq \nu_e$. In 1988, Lederman, Schwartz and Steinberger, the participants of the Brookhaven experiment, were awarded the Nobel Prize for *"the discovery of the muon neutrino leading to the classification of elementary particles into families."*

We come now to a very bright idea of B. P. which led to the creation of a new field in the neutrino physics: idea of neutrino masses, mixing and oscillations. B. P. came to the idea of neutrino oscillations in 1957–58. He was impressed by a possibility of $K^0 \rightleftarrows \overline{K^0}$ oscillations suggested by Gell-Mann and Pais. This phenomenon was based on the following properties:

1. K^0 and $\overline{K^0}$ are different particles. They possess a strangeness $+1$ and -1, respectively. The strangeness is conserved in strong interactions.
2. Weak interactions do not conserve the strangeness. As a result, K^0 and $\overline{K^0}$ are "mixed" particles and transitions between them in the vacuum become possible.

In 1957, B. P. put the following question: *"Are there other "mixed" neutral particles (not necessarily elementary ones) which are not identical to their corresponding antiparticles and for which the particle-antiparticle transitions are not strictly forbidden?"* He proposed muonium $(\mu^+ e^-)$ to antimuonium $(\mu^- e^+)$ oscillations [4]. At that time it was not known that ν_e and ν_μ are different particles. B. P. suggested that the transitions $(\mu^+ e^-) \rightleftarrows (\mu^- e^+)$ are allowed and *"induced by the same interaction which is responsible for the μ decay:"* $(\mu^+ e^-) \rightarrow \nu + \overline{\nu} \rightarrow (\mu^- e^+)$. Note that the experiments searching for the muonium-antimuonium transitions, proposed by B. P., are still going on at present. They provide a sensitive way of obtaining information about interactions in which the flavor lepton numbers are changed by two units.

B. P. was also thinking about the neutrino. The problem was that the two-component neutrino theory was perfectly established at that time. According to this theory, only the left-handed neutrino ν_L and right-handed antineutrino $\overline{\nu}_R$ exist in the Nature (only one type of neutrino was known at that time). Transitions between them are forbidden by the conservation of angular momentum. A rumor helped B. P. realize the idea of neutrino oscillations in case of one neutrino flavor. In 1957, R. Davis was searching for ^{37}Ar production in the process: $\overline{\nu}_{\text{reactor}} + {}^{37}Cl \longrightarrow e^- + {}^{37}Ar$. The rumor that Davis had observed such "events" reached B. P. He suggested that these "events" could be due to neutrino oscillations, i.e., transitions of reactor antineutrinos into the right-handed neutrinos on their way from the reactor to the detector. He published the first paper dedicated to neutrino oscillations in 1958 [5]. In this paper, he wrote: *"The neutrino may be a particle mixture, and consequently there is a possibility of real neutrino-antineutrino transitions in vacuum, provided that the lepton (neutrino) charge is not conserved. This means that the neutrino and antineutrino are mixed particles, i.e., a symmetric and antisymmetric combination of two truly neutral Majorana particles*

ν_1 *and* ν_2." And further in the paper: *"This possibility became of some interest in connection with new investigations of inverse* β *processes."* B. P. considered a transition: $\overline{\nu}_R \to \nu_R$ (and similarly $\nu_L \to \overline{\nu}_L$), i.e., he had to assume that the lepton number is not conserved, but also that (in addition to the $\overline{\nu}_R$ and ν_L quanta of the left-handed neutrino field $\nu_L(x)$) the ν_R and $\overline{\nu}_L$ quanta of the right-handed neutrino field $\nu_R(x)$ existed as well. According to the two-component neutrino theory, only the field $\nu_L(x)$ enters the weak-interaction Lagrangian. Thus, ν_R and $\overline{\nu}_L$ must be non-interacting "sterile" particles. In order to explain the Davis "events", B. P. had to assume that *"a definite fraction of particles can induce the reaction."*

In the 1958 paper, B. P. pointed out that in the experiment of Reines and Cowan a deficit of antineutrino events will be observed due to neutrino oscillations: *"The cross section of the process* $\overline{\nu} + p \longrightarrow e^+ + n$ *with* $\overline{\nu}$ *from the reactor must be smaller than expected. This is due to the fact that the neutral lepton beam, which at the source is capable of inducing the reaction, changes its composition on the way from the reactor to the detector."* Later, the anomalous "events" in the Davis' experiment disappeared and only an upper bound for the cross section of the reaction: $\overline{\nu} + {}^{37}Cl \longrightarrow e^- + {}^{37}Ar$ was obtained. B. P. understood that ν_R and $\overline{\nu}_L$ must be non-interacting, sterile particles. The terminology "sterile neutrino," which is standard nowadays, was introduced by B. P. Starting from this first paper, all his life B. P. believed in the existence of neutrino oscillations. He wrote: *"The effects of transformation of the neutrino into antineutrino and vice versa may be unobservable in the laboratory, but will certainly occur, at least, on an astronomical scale."*

The next paper on neutrino oscillations was written by B. P. in 1967 [6]. At that time, the phenomenological V – A theory was established, $K^0 \rightleftarrows \overline{K^0}$ oscillations were observed, and it was proved that (at least) two types on neutrinos ν_e and ν_μ exist in the Nature. B. P. discussed the transitions between active neutrinos $\nu_\mu \rightleftarrows \nu_e$ and also transitions $\nu_e \rightleftarrows \overline{\nu}_{eL}$ and $\nu_\mu \rightleftarrows \overline{\nu}_{\mu L}$, which transform *"the active particles into particles which, from the point of view of ordinary weak processes, are sterile."* He pointed out that not only the disappearance of ν_μ, but also the appearance of ν_e can be observed. In case of transitions of the active neutrinos into the sterile ones, only the disappearance of the initial active neutrinos can be observed.

In the 1967 paper, B. P. discussed the effect of neutrino oscillations for the solar neutrinos: *"From an observational point of view, the ideal object is the Sun. If the oscillation length is smaller than the radius of the solar region effectively producing the neutrinos, direct oscillations will be smeared out and unobservable. The only effect on the Earth's surface would be that the flux of observable solar neutrinos must be two times smaller than the total (active and sterile) neutrino flux."* When the first results of the Davis solar neutrino experiment were obtained (1970), it occurred that the detected flux of the solar neutrinos was about 2–3 times smaller than the predicted flux. This observation became known as the Solar Neutrino Problem and was anticipated by B. P. Soon, his explanation of the Solar Neutrino Problem by the oscillations of solar neutrinos was commonly accepted.

The next paper which appeared after the pioneering papers of B. P. was the paper by Gribov and B. P. [7]. It was based on the assumption that only the left-handed neutrinos ν_e, ν_μ and right-handed antineutrinos $\overline{\nu}_e$, $\overline{\nu}_\mu$ exist in the Nature. The authors assumed

Figure 4. **Left panel**: B. P. with N. N. Bogoliubov (Dubna, 1970s).
Right panel: B. P. as a fisherman.

that, in addition to the V − A interaction, the full Lagrangian $\mathscr{L}$ includes an effective interaction between the neutrinos which violates the lepton numbers L_e and L_μ. After the diagonalization of the effective interaction it was found that:

$$\nu_{eL} = \cos\theta\,\chi_{1L} + \sin\theta\,\chi_{2L},$$
$$\nu_{\mu L} = -\sin\theta\,\chi_{1L} + \cos\theta\,\chi_{2L},$$

where $\chi_{1,2}$ are the fields of Majorana neutrinos with masses $m_{1,2}$, respectively, and θ is the mixing angle. The neutrino masses and mixing angle are determined by three parameters of the effective interaction. For the $\nu_e \to \nu_e$ transition probability in vacuum it was obtained (in modern notations):

$$P(\nu_e \to \nu_e) = 1 - \frac{1}{2}\sin^2 2\theta\left(1 - \cos\frac{\Delta m^2 L}{2E}\right),$$

with the mass-squared difference $\Delta m^2 = |m_2^2 - m_1^2|$. The authors applied the developed formalism to the solar-neutrino oscillations. The maximal mixing ($\theta = \pi/4$) was considered as the most attractive possibility. In such case, the averaged flux of the solar neutrinos is equal to $1/2$ of the predicted flux.

In 1975, B. P. and myself started a long-term collaboration (about 15 years) on the study and development of the idea of neutrino masses, mixing and oscillations. Our first paper was based on the idea of quark-lepton analogy [8]. At that time, it was established that the quark charged current (CC) in case of four quarks has the form:

$$j_\alpha^{\mathrm{CC}} = 2\left[\bar{u}_L\,\gamma_\alpha\,d_L^c + \bar{c}_L\,\gamma_\alpha\,s_L^c\right],$$

where $d_L^c = \cos\theta_C\,d_L + \sin\theta_C\,s_L$ and $s_L^c = -\sin\theta_C\,d_L + \cos\theta_C\,s_L$ are the Cabibbo–GIM mixed quark fields, and θ_C is the Cabibbo angle. It was known that the lepton CC has

the same form as the quark one:

$$j_\alpha^{\mathrm{CC}} = 2\left[\overline{\nu}_{eL}\gamma_\alpha e_L + \overline{\nu}_{\mu L}\gamma_\alpha \mu_L\right].$$

The question was: *"Are ν_{eL} and $\nu_{\mu L}$ mixed fields?"* We believed in a deep analogy between the quarks and leptons and suggested that:

$$\nu_{eL} = \cos\theta\,\nu_{1L} + \sin\theta\,\nu_{2L},$$
$$\nu_{\mu L} = -\sin\theta\,\nu_{1L} + \cos\theta\,\nu_{2L},$$

where $\nu_{1,2}$ are the fields of neutrinos with definite masses $m_{1,2}$, respectively, and θ is the leptonic mixing angle. In such a scheme, all fundamental fermions have nonvanishing masses and are Dirac particles.

After the great success of the two-component neutrino theory, there was a general belief that the neutrinos are massless particles. Our arguments in favor of nonzero neutrino masses were the following:

- There is no principle (like gauge invariance in case of photons) which requires that the masses of neutrinos must be equal to zero.
- After the V – A theory, which is based on the assumption that the CC Lagrangian contains the L-components of all fields, it was natural to assume that the neutrinos are not special massless particles but—like quarks and charged leptons—have nonzero masses.

We also discussed the possible value of the mixing angle θ. We argued that:

- There is no reason for $\theta = \theta_{\mathrm{C}}$.
- *"It seems to us that the special values of the mixing angles $\theta = 0$ and $\theta = \pi/4$ (maximum mixing) are of the greatest interest."* The probabilities of transitions $\nu_l \to \nu_{l'}$ are the same in the schemes involving the mixing of two Majorana and two Dirac neutrinos.

In our next paper we considered the most general neutrino mixing [9]. In 1977, we wrote the first review of the neutrino oscillations [10]. We characterized the neutrino mixing by neutrino mass terms, which is a common practice nowadays. We showed that in general three types of the neutrino mass terms are possible:

I. Majorana mass term (generalization of Gribov–B. P.):

$$\mathscr{L}_L^{\mathrm{M}} = -\frac{1}{2}\overline{\nu}_L M_L \nu_L^c + \mathrm{H.c.},$$

where $\nu_L = \left(\nu_{eL}, \nu_{\mu L}, \nu_{\tau L}\right)^{\mathrm{T}}$ is a three-component column of the left-handed neutrino fields, $\nu_L^c = C\overline{\nu}_L^{\mathrm{T}}$ is the charge conjugated field, and $M_L = M_L^{\mathrm{T}}$ stands for the (symmetric) complex 3×3 Majorana mass matrix. After diagonalization of the matrix M_L we obtain:

$$\nu_{lL} = \sum_{i=1}^{3} U_{li}\,\nu_{iL},$$


Figure 5. **Left panel**: B. P. with S. M. Bilenky at a "not so boring" seminar (Dubna, 1977). **Right panel**: B. P. with S. M. Bilenky (Dubna, 1983).

where U is the unitary 3×3 Pontecorvo–Maki–Nakagawa–Sakata (PMNS) matrix: $U^\dagger U = 1$, and $\nu_i = \nu_i^c$ is the field of a Majorana neutrino with mass m_i.

II. Dirac mass term:

$$\mathscr{L}^{\mathrm{D}} = -\overline{\nu}_L M^{\mathrm{D}} \nu_R + \mathrm{H.c.},$$

with $\nu_R = \left(\nu_{eR}, \nu_{\mu R}, \nu_{\tau R}\right)^{\mathrm{T}}$ being a three-component column of the right-handed neutrino fields and M^{D} the complex 3×3 Dirac mass matrix. In such scenario, the total lepton number L is conserved. Diagonalization of the matrix M^{D} again yields:

$$\nu_{lL} = \sum_{i=1}^{3} U_{li}\, \nu_{iL},$$

where ν_i is the field of a Dirac neutrino with mass m_i. The total lepton number of neutrino ν_i and antineutrino $\overline{\nu}_i$ is defined as $+1$ and -1, respectively.

III. Dirac–Majorana mass term:

$$\mathscr{L}^{\mathrm{D+M}} = \mathscr{L}_L^{\mathrm{M}} + \mathscr{L}^{\mathrm{D}} + \mathscr{L}_R^{\mathrm{M}}$$

with the right-handed Majorana mass term:

$$\mathscr{L}_R^{\mathrm{M}} = -\frac{1}{2}\overline{\nu_R^c} M_R \nu_R + \mathrm{H.c.}$$

In the case of such mass term there are no conserved lepton numbers. After the diagonalization, the neutrino mixing ($l = e, \mu, \tau$):

$$\nu_{lL} = \sum_{i=1}^{6} U_{li}\, \nu_{iL},$$

$$\nu^c_{lR} = \sum_{i=1}^{6} U_{\bar{l}i}\, \nu_{iL}$$

is realized by a 6×6 generalization of the PMNS matrix U, while $\nu_i = \nu_i^c$ is the Majorana-neutrino fields with masses m_i ($i = 1, \ldots, 6$).

In case of the Dirac and Majorana mass terms, only the transitions $\nu_l \rightleftarrows \nu_{l'}$ between the active flavor neutrinos are possible. On the other hand, the Dirac–Majorana mass term also allows for the transitions $\nu_l \rightleftarrows \bar{\nu}_{l'}$ involving the sterile neutrino flavors.

Our approach to the neutrino oscillations in vacuum is described below. What are the states of flavor neutrinos ν_e, ν_μ and ν_τ produced in the weak decays, captured in the neutrino processes, etc.? For example, a flavor muon neutrino ν_μ is from our point of view a particle which is produced together with μ^+ in the decay: $\pi^+ \longrightarrow \mu^+ + \nu_\mu$, etc. We suggested that the states of flavor neutrinos are given by:

$$|\nu_l\rangle = \sum_i U^*_{li}\, |\nu_i\rangle\,,$$

with $l = e, \mu, \tau$, while $|\nu_i\rangle$ are the states of neutrinos with definite momentum $\vec{p}$ and energy $E_i = \sqrt{\vec{p}^2 + m_i^2} \simeq E + \frac{m_i^2}{2E}$. In accordance with QFT, we assumed that the evolution of states is determined by the Schrödinger equation: $i\partial_t\, |\Psi(t)\rangle = H\, |\Psi(t)\rangle$. If at a time $t = 0$ a flavor neutrino ν_l is produced, at a later instant t we have:

$$|\nu_l(t)\rangle = e^{-iHt}\, |\nu_l\rangle = \sum_i |\nu_i\rangle\, e^{-iE_i t} U^*_{li}.$$

Thus, in case of mixing the neutrino state at a time t is a superposition of states with different energies, i.e., a non-stationary state. From our point of view, this is a basis of neutrino oscillations. The neutrinos are detected via observation of weak-interaction processes in which the flavor neutrinos are participating ($\nu_{l'} + N \longrightarrow l' + X$, etc.). We have:

$$|\nu_l(t)\rangle = \sum_{l'} |\nu_{l'}\rangle \left(\sum_i U_{l'i}\, e^{-iE_i t} U^*_{li} \right).$$

The probability of the transition $\nu_l \to \nu_{l'}$ reads:

$$P(\nu_l \to \nu_{l'}) = \left| \sum_i U_{l'i}\, e^{-iE_i t} U^*_{li} \right|^2 = \left| \delta_{l'l} + \sum_{i \neq k} U_{l'i} \left(e^{-i\frac{\Delta m^2_{ik} L}{2E}} - 1 \right) U^*_{li} \right|^2,$$

where L is the distance source-detector and $\Delta m^2_{ik} = m^2_k - m^2_i$ is a mass-squared difference. This expression for the transition probability became a standard.

For many years, the idea of massless strictly two-component neutrinos prevailed. The situation changed drastically after the appearance of Grand Unified Theories and the seesaw mechanism of neutrino mass generation (by the end of the 1970s). Neutrino masses and mixing started to be considered a signature of new, beyond the Standard Model physics. However, there was (and still is) no theory which could predict the values of neutrino masses and mixing angles. Our approach was the following:

- It is plausible that the neutrinos are massive and mixed.
- Search for neutrino oscillations, which is an interference phenomenon, is the most sensitive way to search for small neutrino masses.
- Neutrino oscillations must be searched for in experiments with neutrinos from all sources (reactor, accelerator, cosmic rays, the Sun, etc.), which have sensitivity to different values of Δm^2_{ik}.

This strategy brought success. At present, there is a proof that the neutrinos are massive and mixed particles. This proof was first obtained in the Super-Kamiokande atmospheric neutrino experiment, and later in the SNO solar neutrino experiment and the KamLAND reactor experiment. It was first verified in the K2K and MINOS accelerator experiments, and later in other neutrino oscillation experiments.

Starting from 1957, B. P. became a great enthusiast of the neutrino oscillations. For the rest of his life, the neutrino masses and oscillations remained his beloved research subject. The discovery of neutrino oscillations was a great triumph of B. P. who came to the idea of neutrino oscillations at a time when the common opinion favored massless neutrinos and no neutrino oscillations. From my point of view, the history of neutrino oscillations is an illustration of the importance of analogy in physics. It is also an illustration of the importance of new courageous ideas which are not always in agreement with the general opinion.

B. P. was a big fan of underwater fishing. In autumn, he usually went to some place about 100 km from Dubna next to a small, very clear river Nerl. Frequently, he invited my wife and myself for such trips. While he was in the river looking for fish, we usually made fire (to cook fish if available) and picked mushrooms. After about two hours in the river, B. P. returned happy, frozen, but often without fish... Yet, the fire and mushrooms were there. I remember that only once during a very hot and dry summer, when fires were forbidden, he caught a lot of fish... Alas, we could not prepare it and gave it to the local people.

We started our collaboration on neutrino oscillations in the car during one such trip. The Cabibbo–GIM mechanism of quarks was firmly established at that time. I asked B. P.: *"Why neutrinos do not do the same?"* It seemed that this approach to neutrino masses and mixing was interesting to him. It concerned a symmetry between the quarks and leptons. After many days of work, we wrote our first paper on neutrino oscillations. It was only five pages long, but I remember that it took a lot of efforts and we were completely exhausted after writing it. Generally, it was always difficult to write papers with B. P. He would never admit any imprecise statements and always required very clear formulations of all assumptions and results. His English (as well as Russian) was perfect, and he always succeeded in finding capacious phrases.

The years of work and friendship with B. P. were the happiest and unforgettable

Figure 6. **Left panel**: B. P. with his secretary I. G. Pokrovskaya (Dubna, 1983).
Right panel: B. P. with H. Langevin-Joliot, daughter of Irène and Frédéric Joliot-Curie (Dubna, 1984).

years in my life. His wide and profound knowledge of physics, his love of physics, his ingenious intuition and his ability to understand complicated problems in a clear and simple way were gifts from God. B. P. was a true scientist in the best, classical sense of the word. When he thought about some problem, he thought about it continuously from early morning till late evening. He devoted all his resources and great intellect to science, and although he was not indifferent to the recognition of his contribution to physics, his main stimulus was the search for truth.

More than 10 last years of his life were for B. P. the years of a courageous struggle against the Parkinson's disease. His love of physics and of the neutrino helped him to overcome the difficult problems related to the illness. He never ceased to work, to think about neutrinos and to continue his active life. Two days before his death, B. P. came to his office at the second floor of the Laboratory of Nuclear Problems in JINR Dubna, where he had been working for 43 years. When he was leaving the laboratory, he looked into the window upon the golden and yellow birches and said to his secretary, Ms. Irina Pokrovskaya: *"Look how beautiful these colors are..."* It was a nice Russian Golden Autumn, September 22, 1993.

Bruno Pontecorvo was one of the first men who understood the importance of neutrinos in elementary particle physics and astrophysics. He felt and understood neutrinos probably better than anybody else in the world. Starting from his time in Canada, he had been thinking about the neutrino his whole life. He was never confined by narrow theoretical frameworks. He was completely open-minded, without any prejudices, very courageous and with very good intuition and scientific taste. He was also a very bright, wise, exceptionally interesting and very friendly personality. People liked him and he had many friends in Italy, Russia, France, Canada and many other countries. The name of Bruno Pontecorvo will be forever connected to the neutrino as the name of the founding father of modern neutrino physics. He will remain with us in our memory and our

hearts as a great and outstanding physicist, as a man of a great impact and humanity.

REFERENCES

1. B. Pontecorvo, *Inverse β-process*, Report PD-205, Chalk River Laboratory, 1946.
2. B. Pontecorvo, *Nuclear capture of mesons and the meson decay*, Phys. Rev. **72**, 246 (1947).
3. B. Pontecorvo, *Electron and muon neutrinos*, Sov. Phys. JETP **10**, 1236 (1960).
4. B. Pontecorvo, *Mesonium and anti-mesonium*, Sov. Phys. JETP **6**, 429 (1957) [Zh. Eksp. Teor. Fiz. **33**, 549 (1957)].
5. B. Pontecorvo, *Inverse β-processes and non conservation of lepton charge*, Sov. Phys. JETP **7**, 172 (1958) [Zh. Eksp. Teor. Fiz. **34**, 247 (1958)].
6. B. Pontecorvo, *Neutrino experiments and the question of the lepton charge conservation*, Sov. Phys. JETP **26**, 984 (1968) [Zh. Eksp. Teor. Fiz. **53**, 1717 (1967)].
7. V. N. Gribov and B. Pontecorvo, *Neutrino astronomy and lepton charge*, Phys. Lett. **B 28**, 493 (1969).
8. S. M. Bilenky and B. Pontecorvo, *Quark-lepton analogy and neutrino oscillations*, Phys. Lett. **B 61**, 248 (1976).
9. S. M. Bilenky and B. Pontecorvo, *Again on neutrino oscillations*, Nuovo Cim. Lett. **17**, 569 (1976).
10. S. M. Bilenky and B. Pontecorvo, *Lepton Mixing and Neutrino Oscillations*, Phys. Rept. **41**, 225 (1978).

PHOTO GALLERY

Welcome party

Lecture hall

Lecture hall

Lectures

Lectures

Poster session

Poster session

Banquet

Banquet

Banquet

POSTER SESSION

Student poster presentations

(31 August 2017, Prague)

1. Allakhverdyan Vladimir (JINR, Dubna): *MC study of strange particle production in the Nova Near Detector before*
2. Almazan Helena (MPI, Heidelberg): *The search for sterile neutrinos with the Stereo experiment*
3. Antoshkina Tatiana (JINR, Dubna): *Optical simulation of PMT*
4. Boschi Tommaso (IPPP, Univ. of Durham): *Searching for MeV-scale neutrinos with the DUNE near detector*
5. Brunst Tim (MPI, Heidelberg): *Detector Development for a sterile neutrino search with the KATRIN experiment*
6. Caracas Ioana Alexandra (JINR, Dubna): *Gigaton Volume Detector Baikal*
7. Centelles Chuliá Salvador (Inst. de Física Corpuscular, Paterna): *Scalar WIMP dark matter from diracness of neutrinos*
8. Cheng Yaping (IKP-2, Forschungszentrum Jülich, Jülich / IHEP, Beijing): *Waveform reconstruction in JUNO*
9. Fajt Lukas (IEAP CTU, Prague): *Baikal GVD - Time calibrations in 2016*
10. Fazliakhmetov Almaz (MIPT, Moscow): *Measurement of muon flux in the Canfranc Underground Laboratory*
11. Inácio Ana Sofia (LIP, Lisbon): *Optical Calibration of the SNO+ Detector*
12. Kerényi Peter (Comenius Univ., Bratislava): *The reactor antineutrino signal maps of Slovakia and the Czech Republic*
13. Khan Amir Nawaz (SYSU, Guangzhou): *PandaX-III Prototype Detector*
14. Kowal Beata (Univ. of Wrocław): *Single pion production in neutrino-nucleon scattering*
15. Lin Heng (SJTU, Shanghai): *PandaX-III: Searching for neutrinoless double-beta decay of* ^{136}Xe
16. Macko Miroslav (IEAP CTU, Prague/Comenius Univ., Bratislava/Univ. de Bordeaux): *Study of Reconstruction Precision of Double Beta Decay Vertex for SuperNEMO Demonstrator*
17. Mantegazzini Federica (Heidelberg Univ., Kirchhoff Inst. for Physics, Heidelberg): *Optimization of metallic magnetic calorimeter arrays with embedded* ^{163}Ho *for the ECHo experiment*
18. Miloradovic Michael (Univ. of Zurich): *Pulse Shape Simulations for the GERDA experiment*

19. Mora Lepin Luis Alberto (Pontificia Univ. Católica de Chile, Santiago): *Limits on Sterile Neutrino Detection at Daya Bay*
20. Nae Ştefan-Alexandru (LIP, Lisbon/ FCUL, Univ. de Lisboa): *Reactor antineutrinos in SNO+*
21. Navas Nicolás Diana (CIEMAT, Madrid): *Measuring the neutrino mixing angle θ_{13} with the Double Chooz experiment*
22. Oliviéro Guillaume (LPC, Caen): *SuperNEMO demonstrator: trigger system*
23. Palušová Veronika (Comenius Univ., Bratislava): *Monte Carlo simulations of HPGe detectors background and development of AMS methods for radiopurity measurements*
24. Pestel Valentin (LPC, Caen) : *Neutron calibration of the SoLid detector*
25. Roca Christian (MPI, Heidelberg): *Sterile neutrinos featuring STEREO experiment - Data analysis*
26. Rong Shu-jun (Shaanxi Univ. of Technology, Hanzhong): *A novel mathematical construct for the family of leptonic mixing patterns*
27. Sicking Philipp (Technische Univ., Dortmund): *Discriminating sterile neutrinos and unitarity violation with CP invariants*
28. Suvorov Sergey (INR RAS, Moscow): *Search for Heavy Neutral Leptons with the near detector complex ND280 of the T2K experiment*
29. Vishneva Alina (JINR, Dubna): *Recent results of Borexino Phase-II solar neutrino program*
30. Wagaarachchi Sachinthya Lapalu (Univ. of California, Berkeley): *Neutrinoless double beta decay search with CUORE*
31. Xie Fang (Univ. College London): *Low Radon Background Techniques for the SuperNEMO Experiment*
32. Żarnecki Grzegorz (NCBJ, Warsaw): *Antimuon selection with the near detector ND280 of the T2K experiment*
33. Zolotarova Anastasiia (CEA, Saclay): *Searching for neutrinoless double beta decay with scintillating bolometers: the CUPID/Mo experiment*

Optical simulation of PMT

Tatiana Antoshkina and Dmitry Naumov

Dzelepov Laboratory of Nuclear Problems, JINR Dubna, 141980 Dubna, Moscow region, Russia

Abstract. JUNO experiment aims to determine the neutrino mass hierarchy by precise measurement of the reactor antineutrino spectrum. The required accuracy of the energy reconstruction is at least 3% at 1 MeV of released energy. In this work we formulate the requirements for methods of measuring the PMT's zonal photodetection efficiency as well as for mass testing techniques. The requirements are formulated based on the simulation of PMT response taking into account its optical properties and light-field distribution of the scanning device. They are intended to obtain proper information from the mass testing results in order to achieve the required energy reconstruction accuracy.

INTRODUCTION

An unique experiment named JUNO for Jiangmen Underground Neutrino Observatory is under construction in southern China by a wide international collaboration. JUNO reactor antineutrino experiment aims to determine the neutrino mass hierarchy at $(3-4)\sigma$ level. To achieve this goal JUNO has to reconstruct $\bar{\nu}_e$ energy with accuracy better than $3\%/\sqrt{E_{\text{vis}}/\text{MeV}}$. This resolution is expected to be reached by maximizing light yield and collection efficiency. One of the ingredients of this unprecedented energy resolution is high quantum efficiency PMTs, produced by Hamamatsu (Japan) and North Vision (China). There are two ways to characterize and test these PMTs. One is to use the scanning station that was made in JINR. It makes very precise test by scanning the surface of all PMT but requires a lot of time to test each PMT separately. Another method utilizes the container that is able to test several PMTs at one time. It studies the response of the entire photomultiplier to the incident light distribution inside the container and its integral measurements need to be studied. In our study we setup the requirements for the container method to guarantee required energy resolution.

OPTICS SIMULATION

PMT is a complex system consisting of the three media, the middle of which — photocathode — is a thin layer (about 25 nm), where the interference of light is possible. Interference of transmitted and back-scattered light in the thin layer requires proper calculation of amplitudes.

The simple case

Let us consider first the simple case — refraction at the boundary between two non-absorbing media. In general light falls on the boundary at an angle θ_0. Part of the light reflects back into the medium from which light is incident and the remaining portion passes to a different medium. Moreover, reflection and refraction of light is different for different polarizations. Let us consider coefficients of reflection R_s, R_p and transmission T_s, T_p depending on the incidence angle θ_0.

$$r_{if}^s = \frac{n_i\cos(\theta_i) - n_f\cos(\theta_f)}{n_i\cos(\theta_i) + n_f\cos(\theta_f)}, \quad t_{if}^s = \frac{2n_i\cos(\theta_i)}{n_i\cos(\theta_i) + n_f\cos(\theta_f)}, \tag{1}$$

$$r_{if}^p = \frac{\frac{1}{n_i}\cos(\theta_i) - \frac{1}{n_f}\cos(\theta_f)}{\frac{1}{n_i}\cos(\theta_i) + \frac{1}{n_f}\cos(\theta_f)}, \quad t_{if}^p = \frac{\frac{2}{n_i}\cos(\theta_i)}{\frac{1}{n_i}\cos(\theta_i) + \frac{1}{n_f}\cos(\theta_f)}. \tag{2}$$

$$R_s = |r_{if}^s|^2 = \left(\frac{n_i\cos(\theta_i) - n_f\cos(\theta_f)}{n_i\cos(\theta_i) + n_f\cos(\theta_f)}\right)^2, \quad T_s = \frac{n_f\cos(\theta_f)}{n_i\cos(\theta_i)}|t_{if}^s|^2, \tag{3}$$

$$R_p = |r_{if}^p|^2 = \left(\frac{n_i\cos(\theta_f) - n_f\cos(\theta_i)}{n_i\cos(\theta_f) + n_f\cos(\theta_i)}\right)^2, \quad T_p = \frac{\frac{1}{n_f}\cos(\theta_f)}{\frac{1}{n_i}cos(\theta_i)}|t_{if}^p|^2. \tag{4}$$

Incidence and refraction angles are related by Snell's law $n_0\sin(\theta_0) = n_1\sin(\theta_1)$. If the medium is not absorbing the transmission coefficients are associated with the reflection ones as $T = 1 - R$. Averaging over the possible polarizations one can get the general reflection and transmission coefficients

$$R = \frac{1}{2}(R_s + R_p), \quad T = \frac{1}{2}(T_s + T_p). \tag{5}$$

Three media with thin absorbing layer

Consider now a more complex system consisting of three media the middle of which is a thin membrane (photocathode) with thickness d_2 where the interference of light is possible. Following the calculation scheme (see left panel of Figure 1) and summing the series we obtain the reflection and transmission amplitudes

$$r = \frac{r_{12} + r_{23}e^{2\imath\beta}}{1 + r_{12}r_{23}e^{2\imath\beta}}, \quad t = \frac{t_{12}t_{23}e^{\imath\beta}}{1 + r_{12}r_{23}e^{2\imath\beta}}, \tag{6}$$

$$\text{where } \beta = \frac{2\pi}{\lambda}d_2 \cdot n_2\cos(\theta_2) = \eta \cdot n_2\cos(\theta_2). \tag{7}$$

The refractive index of the thin layer n_2 is substituted by the combination of the refractive and absorption indices $n_2(1 + \imath k_2)$. After the substitution the refraction angle in the second layer becomes complex which will affect the final result. Following the

parametrization $n_2(1+\imath k_2)\cdot\cos(\theta_2) = u_2 + \imath v_2$ we obtain the formulas for reflection and transmission coefficients

$$R = |r|^2 = \frac{|r_{12}|^2 + |r_{23}|^2 e^{-4v_2\eta} + 2\Re(r_{12}r_{23}^* e^{\imath 2u_2\eta} e^{-2v_2\eta})}{1 + |r_{12}|^2|r_{23}|^2 e^{-4v_2\eta} + 2\Re(r_{12}r_{23} e^{\imath 2u_2\eta} e^{-2v_2\eta})}, \tag{8}$$

$$T = C_t|t|^2 = C_t \frac{|t_{12}|^2|t_{23}|^2 e^{-2v_2\eta}}{1 + |r_{12}|^2|r_{23}|^2 e^{-4v_2\eta} + 2\Re(r_{12}r_{23} e^{\imath 2u_2\eta} e^{-2v_2\eta})}. \tag{9}$$

Logically if the system has a medium with absorption the reflection and transmission coefficients in the sum will be lower than 1. There is an absorption coefficient which is defined as $A = 1 - R - T$. We can easily add any number of thin layers to the system discussed earlier.

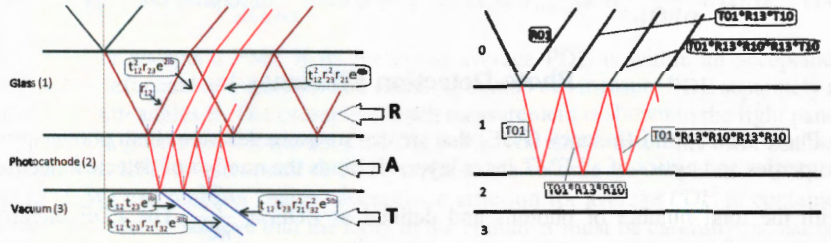

FIGURE 1. Calculation schemes: interference of light in photocathode (**left panel**). Addition of the outer medium (**right panel**).

Four media with thin absorbing layer

Finally let us consider the four media system, e.g. air-glass-photocathode-vacuum system that is the PMT in the air. Glass in this case has a thickness much greater than the length of the incident light, therefore there is no interference of light in it and the effect of the air-glass interface is reduced to a pure energy calculation of multiple reflections in the glass (see right panel of Figure 1).

$$R_{03} = R_{01} + \frac{R_{13}T_{01}^2}{1 - R_{10}R_{13}}, \tag{10}$$

$$T_{03} = \frac{T_{01}T_{13}}{1 - R_{10}R_{13}}, \tag{11}$$

$$A_{03} = 1 - R_{03} - T_{03}. \tag{12}$$

Optical coefficients depend on an incident angle and polarization of light as well as on outer medium. Taking into account interference effects in thin layers such as photocathode in PMT can significantly change optical coefficients, especially absorption coefficient. On the Figure 2 you can see the dependence of the ratio

$$R = \frac{A_{\text{with interference}}}{A_{\text{w/o interference}}}$$

on the photocathode thickness.

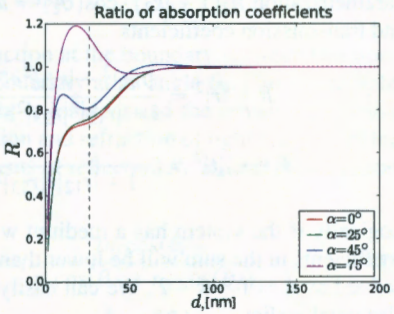

FIGURE 2: Impact of the interference to the absorption coefficient.

Photo-Detection Efficiency

Photo-Detection Efficiency (PDE) that we can measure describes both photocathode properties and optics of all PMT inner layers. It binds the number of detected electrons with the total number of photons and defined as $\text{PDE} = \frac{n_{\text{p.e.}}^{\text{det}}}{n_{\gamma}^{\text{tot}}}$. The PDE therefore depends on both the absorption of light and the collection of charges. After a photon has been absorbed and has generated a photo electron this electron still should be collected. Therefore

$$\text{PDE} = A(\alpha) \cdot P_{\text{p.e.}}(\theta) \cdot \text{CE}(\theta), \tag{13}$$

where $A(\alpha)$ is an absorption coefficient, $P_{\text{p.e.}}$ is probability to produce photoelectron and CE is collection efficiency that binds the number of detected and produced photoelectrons. In order to be accepted PMT requires high PDE which do depend on the PMT illumination via the dependence of A on incident angle α at each point of the surface. We examine below how PDE is sensitive to the known light field distribution (LFD).

OBSERVABLES OF THE SCANNING STATION AND THE CONTAINER

LFD of the scanning station is optimal (normal to surface in each point). On the contrary the container doesn't really provide uniform and isotropic LFD. Measurements made in container should be matched to those made by PMT scanner. This problem is best illustrated by the extreme cases. If only the top of PMT is illuminated but the number of photons is huge, the overall PDE will be high enough and we can accept a bad PMT as we do know nothing about PDE on its periphery.

Acceptance criterion based on the average PDE value measured in the container thus may be misleading. Therefore one has to measure the LFD over PMT surface as a function of incident angles. The properties of the LFD:

- γ field in each point is $\dfrac{d^2\Phi}{d\Omega d\alpha}$;
- $\iint \dfrac{d^2\Phi}{d\Omega d\alpha} d\Omega d\alpha = 1.$

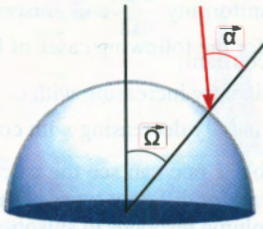

FIGURE 3: Definition of solid angles.

In the container one measures the average PDE from all points of the PMT

$$\overline{\text{PDE}} = \iint \text{PDE}(\Omega, \alpha) \frac{d^2\Phi}{d\Omega d\alpha} d\vec{\Omega} d\alpha = \iint A(\Omega, \alpha) P_{\text{p.e.}}(\Omega, \alpha) \frac{d^2\Phi}{d\Omega d\alpha} d\Omega d\alpha. \quad (14)$$

The container accepts a PMT if its measured average $\overline{\text{PDE}}$ is within an acceptance interval (see left panel of Figure 4). The scanning station can measure PDE separately at different zenith angles θ. The example of such measurement is shown in the right panel of Figure 4. A good PMT should have δ PDE $\leq 3\%$. The container unlike PMT scanner has unknown LFD in each point of PMT surface. It measures the convolution of PDE and LFD. We can repeat a "naive" acceptance criterion for average PDE in container method. In order to achieve that the LFD in the container must be carefully measured. In what follows we examine the required accuracy of LFD in order to guarantee an acceptance of good PMTs.

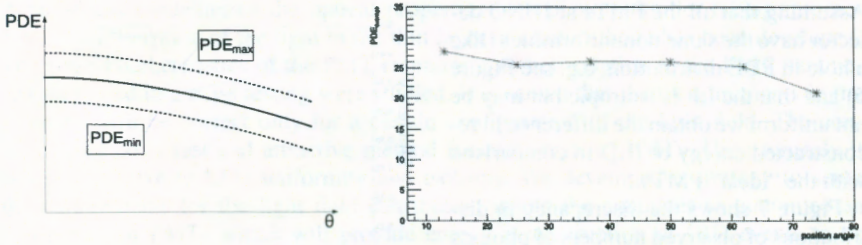

FIGURE 4. Interval of PDE (**left panel**).
Measured PDE (**right panel**).

Scanner to container relative calibration: light field uniformity and isotropy

Let us assume that PDE changes linearly between 27% at $\theta = 0°$ and 21% at $\theta = 90°$. We have tested possible consequences (probably extreme examples) of

non-uniformity $\frac{d\Phi}{d\Omega}$ and anisotropy $\frac{d\Phi}{d\alpha}$ in LFD for the following cases of LFD:

- constant;
- linearly increasing with $\cos\alpha/\cos\theta$;
- linearly decreasing with $\cos\alpha/\cos\theta$.

In Table 1 one can see the calculated PDE intervals for different types of the LFD. The first column responds to anisotropic but uniform (AU) LFD, the third column responds to isotropic but nonuniform (IN) LFD.

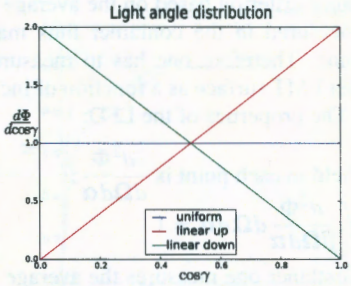

FIGURE 5: Types of the LFD.

TABLE 1. Change of the PDE Interval for different LFDs.

PDE Interval for AU LFD, %	Type of anisotropy or non-uniformity	PDE Interval for IN LFD, %
(17, 22)	constant	(17, 22)
(19, 25)	linear up	(18, 23)
(15, 19)	linear down	(16, 21)

RESULTS

Assuming that all the PMTs at JUNO detector have the same nonuniformities (like a hole in PDE distribution, e.g. see Figure 6) and that the LF is isotropic but may be not uniform we obtain the difference in reconstructed energy of IBD in comparison with the "ideal" PMTs.

Figure 7 shows the discrepancy in distributions of observed numbers of photons for for isotropic uniform and "ascending linear" and "descending linear" LF for the situation when all PMTs have a "hole" from 0° to 30°. The depth of these holes is the greatest possible for satisfying the $\overline{\text{PDE}}_{\text{min}}$.

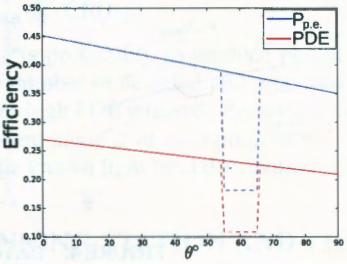

FIGURE 6: How the PDE distribution looks like.

The same situation for the hole from 30° to 40° is shown on Figure 8.

As one can see the presence of the gap may lead to the significant decrease in the number of detected p.e. and therefore to the loss of the energy resolution.

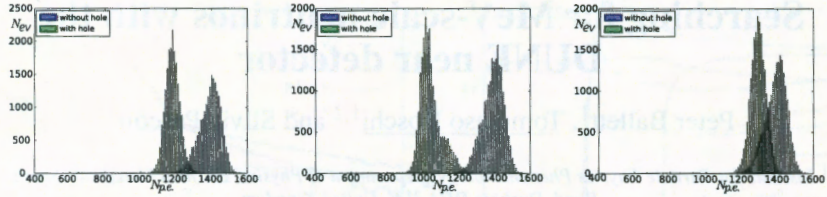

FIGURE 7. Impact of accepted (non-uniform) PMTs on σ_E/E of IBD for uniform, ascending linear and descending linear but isotropic LF ("hole" from 0° to 30°).

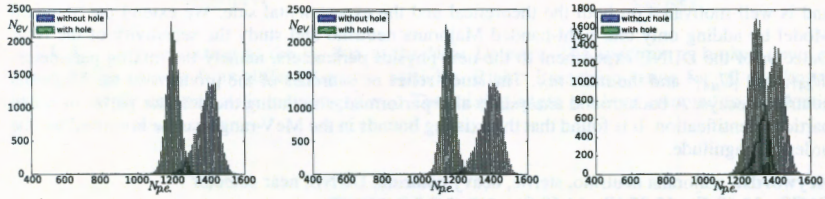

FIGURE 8. Impact of accepted (non-uniform) PMTs on σ_E/E of IBD for uniform, ascending linear and descending linear but isotropic LF ("hole" from 30° to 40°).

CONCLUSION

A numerical modeling of the optical properties of a photomultiplier taking into account the absorption of the light in the thin layer of photocathode has been developed. The zonal characteristics of the PMT response and their relation to the PMT parameters measured in a mass testing were studied. It is shown that the measurements in the container will be correct only for a certain configuration of the light field. The container method is fast and attractive method for mass tests of PMTs. Unfortunately it is very sensitive to LFD uniformity and isotropy. We developed a strategy to setup the requirements for the light field distribution inside the container to guarantee an acceptance of PMTs which will provide energy reconstruction of IBD events to be $\leq 3\%/\sqrt{E_{\text{vis}}/\text{MeV}}$.

REFERENCES

1. M. Born, E. Wolf *Principles of Optics* 1970: Pergamon press.
2. D.Motta, S.Schönert *Optical properties of bialkali photocathodes* 2005: Nuclear Instruments and Methods in Physics Research A 539

Searching for MeV-scale neutrinos with the DUNE near detector

Peter Ballett[1], Tommaso Boschi[1,2] and Silvia Pascoli[1]

[1] *Institute for Particle Physics Phenomenology, Department of Physics, Durham University, South Road, Durham DH1 3LE, United Kingdom*
[2] *Particle Physics Research Centre, School of Physics and Astronomy, Queen Mary University of London, Mile End Road, London E1 4NS, United Kingdom*

Abstract. Adding right-handed neutrinos to the Standard Model is a natural and simple extension and is well motivated on both the theoretical and the experimental side. We extend the Standard Model by adding only one right-handed Majorana neutrino and study the sensitivity of the Near Detector of the DUNE experiment to the new physics parameters, namely the mixing parameters $|U_{e4}|^2$ and $|U_{\mu 4}|^2$ and the mass m_N. The study relies on searches of the products of the Majorana neutrino decays. A background analysis is also performed, simulating the detector performance to particle identification. It is found that the existing bounds in the MeV-range can be improved by one order of magnitude.

Keywords: majorana neutrino, sterile, heavy neutrino, DUNE, near detector
PACS: 12.60.Cn; 13.35.Hb; 14.60.St

INTRODUCTION

The evidence for three neutrino flavour oscillation is well established [1] and can be accounted for only if the neutrino mass splittings are non zero and if the relation between the flavour and mass basis is non trivial. However, the Lagrangian of the Standard Model does not consider a right-handed component for neutrinos and thus does not consider a Dirac mass term either: the neutrino is simply assumed to be massless. In addition to this, a series of experiments reporting anomalous results can properly fit data only in a scenario with 3+1 or 3+2 neutrinos [2]. The experimental evidence strongly suggests amending the structure of the model, possibly including additional fermions.

The simplest modification that can be performed to reach new physics beyond the Standard Model (SM) is to introduce the right-handed counterpart of neutrinos, N. This is well motivated in many theoretical frameworks, which include sterile neutrinos to deal deal with unresolved problems in particle physics. For instance, the widely studied *Neutrino Minimal SM* [3] takes in account three SM-singlet fermions to address the smallness of the neutrino masses with the seesaw mechanism, explain the baryon asymmetry of the Universe and earn a plausible dark matter candidate.

Next-generation neutrino experiments, like DUNE, will be sensitive to the presence of heavy neutrinos through the study of their decays. With this goal in mind, the phenomenology of an extension to multiple fermions does not offer a remarkable difference with respect to a simpler analysis which considers just one right-handed neutrino. Henceforth, this is the extension to the SM we assume in our study.

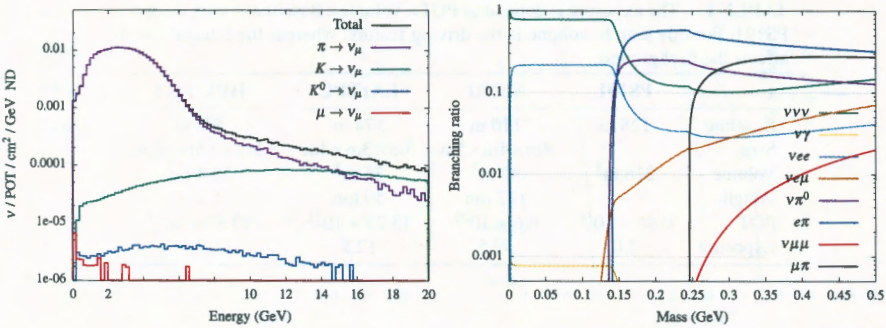

FIGURE 1. Left: prediction of the ν_μ flux at the Near Detector. The spectrum is broken down into the contribution coming from different parent particles. Right: Branching ratios for all the possible decays of a sterile neutrino with mass $m_N < m_K$. The mixing angle are here assumed to be identical, $|U_{e4}|^2 = |U_{\mu 4}|^2 = |U_{\tau 4}|^2$.

THE MODEL

The Lagrangian must include all the terms permitted by gauge symmetries and renormalisability. Given that N is a SM singlet, a Majorana mass term is also allowed and the *minimal model* considered is expressed by the following Lagrangian:

$$\mathscr{L} = \mathscr{L}_{\rm SM} + i\overline{N}\partial\!\!\!/ N + \sum_\alpha Y_\alpha \overline{L}_\alpha \tilde{H} N + \frac{1}{2} M_R \overline{N^C} N + h.c.\,, \tag{1}$$

with $\tilde{H} = i\sigma_2 H$ and the superscript C denoting the charge conjugated field, $\psi^C = C\overline{\psi}^T$. The Yukawa term which couples the new fermion to the Higgs field accommodates a Dirac mass term for the neutrino after Electroweak Symmetry Breaking (EWSB). With the diagonalisation of the mass matrix, the heavy mass state mixes with the light ones into active neutrinos in the following fashion:

$$\nu_\alpha = \sum_{i=1}^{3} U^*_{\alpha i}\, \nu_i + U^*_{\alpha 4}\, N^C\,, \tag{2}$$

where $U_{\alpha i}$ are the entries of the Pontecorvo-Maki-Nakagawa-Sakata matrix and $U_{\alpha 4}$ are the new mixing entries. As the flavour eigenstates are coupled to the electroweak bosons, the new mass eigenstate is also involved in any process in which active neutrinos take part. Feynman rules in the mass basis are derived accordingly [4]. If kinematically allowed, the Majorana neutrinos can be produced in a fixed target experiment, with the same mechanism that generates light neutrinos. A proton beam impinging on a fixed target produces a significant number of light pseudo-scalar mesons, mainly pions and kaons, which in turn decay via leptonic and semi-leptonic channels. The prediction of the ν_μ spectrum broken down by meson parentage is illustrated in figure Fig. 1 on the

TABLE 1. The exposure is defined as POT×Volume×Baseline^{-2} with respect to PS191. For this search, volume is the driving feature, whereas the fiducial weight affects the background.

	PS191	**SBND**	**LArTPC**	**HPArFGT**
Baseline	128 m	110 m	574 m	578 m
Size	–	4m×4m×5m	3m×3m×4m	3.5m×3.5m×6.4m
Volume	216 m^3	80 m^3	36 m^3	78.4 m^3
Weight	–	112 ton	50 ton	8 ton
POT	0.86×10^{19}	6.6×10^{20}	13.23×10^{21}	13.23×10^{21}
Exposure	1.0	39.5	12.7	27.4

left. The deflection of the mesons with magnetic horns into a decay pipe results in a focused neutrino beam, a component of which consists of sterile neutrinos with masses m_N up to the mass of the decaying meson[1]. If the new neutrinos are massive enough, their mass-splittings with the light neutrinos could be larger than the wave packet energy-uncertainty associated with the production mechanism, and so they no longer oscillate [5]. In this scenario, MeV-scale sterile neutrinos can propagate undisturbed from the decay pipe to the detector, where they might decay into visible SM particles. The figure Fig. 1 shows on the right the branching ratio of the possible N decay modes, the decay width of which can be found in [4].

In laboratory searches, no positive evidence of sterile neutrinos has been found so far in the mass range of interest. Searches of N decays can place strong bounds on the free parameters, because the number of unknowns in these experiments is small and the model considered is minimal. These studies typically define an upper and a lower[2] bound on the mixing angle. The current limit in this region is given by the PS191 experiment [6]. The upper bound was set to be $\leq 10^{-8} \sim 10^{-9}$ for both $|U_{e4}|^2$ and $|U_{\mu 4}|^2$. A thorough review of the current constraints is found in [7].

THE EXPERIMENT

The upcoming Deep Underground Neutrino Experiment (DUNE) will study oscillation of neutrinos in great detail, thanks to the 40 kton Liquid Argon Time Projection Chamber (LArTPC) situated 1300 km from the proton target. A smaller and closer detector is needed in order to normalise the flux of neutrinos reaching the far detector. A Near Detector (ND) will be placed 574 m from the target. Even if the final design of the ND has not been decided yet, its active volume will be exposed to an extremely intense neutrino beam during data runs, thanks to its proximity to the target and its size. The ND will be likely a hybrid concept, consisting of a LArTPC in front of a High Pressure Argon TPC (HPArTPC). A summary of the features of the two detector is reported

[1] The heaviest mass that can be yielded is $m_K - m_e \simeq m_K$ for the decay of the charge kaon $K^{\pm} \to Ne^{\pm}$.
[2] If the mixing angle is too large, then the N decays before reaching the detector.

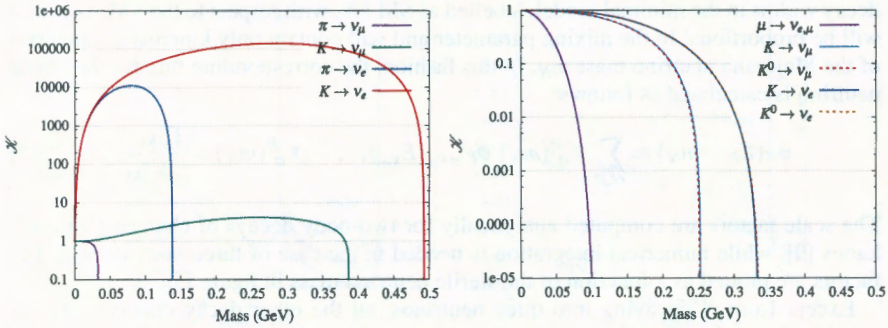

FIGURE 2. Factors $\mathscr{K}$, used to scale the light neutrino flux, plotted as a function of the mass. The mixing parameters are set to one. Left: factors for the two-body decay. The enhancement in the electronic channel is due to the fact that the Majorana neutrinos are not affected by helicity suppression. Right: factors for the three-body decay.

in Tab. 1, where they are compared to PS191 and SBND[3]. We expect a comparable exposure between the ND and SBND.

The expected number of heavy neutrino decays inside the detector for a given channel d can be naively evaluated using the following formula:

$$\mathscr{N}_d = \int \mathrm{d}E \; P_d(E) W_d(E) \frac{\mathrm{d}\phi(N)}{\mathrm{d}E} \,, \tag{3}$$

where $W_d(E)$ is a weighting factor derived from background reduction analyses, and $\mathrm{d}\phi(N)/\mathrm{d}E$ is the number of N expected at the ND. The term $P_d(E)$ accounts for the probability of a Majorana neutrino of energy E to travel the baseline distance and decay inside the near detector. Mathematically, it is expressed in the following form:

$$P_d(E) = e^{-\frac{\Gamma_{\mathrm{tot}} L}{\gamma\beta}} \left(1 - e^{-\frac{\Gamma_{\mathrm{tot}} \lambda}{\gamma\beta}}\right) \frac{\Gamma_d}{\Gamma_{\mathrm{tot}}} \,, \tag{4}$$

where L denotes the baseline, λ the length of detector, Γ_d the partial decay width for the mode d and Γ_{tot} the total decay width. The total effect of P_d is to favour the low-energy bins of the spectrum for which the size of the detector λ is greater than the decay length of the Majorana neutrino, $\beta\gamma\,\Gamma_{\mathrm{tot}}^{-1}$.

The flux $\mathrm{d}\phi(N)/\mathrm{d}E$ is directly related to the SM neutrino spectrum, within reasonable approximation. The flux of light neutrinos ν_α produced from the decay of a given pseudo-scalar meson P can be suitably scaled to obtain a valid heavy neutrino flux. Neglecting energy dependence, a reliable scale factor comes from the ratio of the partial

[3] This detector is part of the *SBN program* at Fermilab and forms an array of detectors together with MicroBooNE and Icarus-600. A similar study to the present one for SBN is found [8].

decay widths in the minimal model, labelled as SM+N, with respect to the SM. The ratio will be proportional to the mixing parameter and will contain only kinematic, functions of the Majorana neutrino mass m_N. In this fashion, the corresponding flux for the sterile neutrino is calculated as follows:

$$\phi_N(E_N - m_N) \approx \sum_{\alpha,P} \mathscr{K}_\alpha^P(m_N)\, \phi_{P\to\nu_\alpha}(E_{\nu_\alpha}) \quad , \quad \mathscr{K}_\alpha^P(m_N) = \frac{\Gamma_{\text{SM}+N}}{\Gamma_{\text{SM}}} \, . \tag{5}$$

The scale factors are computed analytically for two-body decays of charged pions and kaons [9], while numerical integration is needed in the case of three-body decays. The factors are plotted as a function of the sterile neutrino mass in figure Fig. 2.

Except from N decaying into three neutrinos, all the other decay channels are detectable. Some decay modes give a better signature than others thanks to a larger branching ratio and a lower background expectancy. The major source of noise comes from ordinary neutrino-nucleon interaction happening within the fiducial volume of the detector. The most copious events are Charge Current Quasi-Elastic (CCQE) interactions, Neutral Current Elastic (NCE) scatterings, Deep Inelastic Scattering (DIS) and resonance pion production (CC1π). The energy range for these processes overlaps with the expected energies of the Majorana neutrinos. In order to reduce the background, a million neutrino-nucleon events are generated with GENIE and passed to a fast Monte Carlo which accounts for detector smearing effects and mis-identification. Visible hadronic activity or a reconstructed vertex is a conclusive evidence for DIS or QE beam-related scattering event, therefore events with these properties are discarded. The kinematic properties of the remaining background events are compared to simulated signal events. The different behaviours of the two would further help in discriminating signal events from the background. Data analysis cuts are in fact applied to maximise the reduction of background events, while retaining as many signal events as possible. The weighting factors $W_d(E)$ in Eq. 3 are the binned ratio of the N energy spectrum after and before the analysis cuts. The two-body decays $N \to e^\pm\pi^\mp$ and $N \to \mu^\pm\pi^\mp$ are the most promising channels for the detection of a heavy neutrino, being the decay mode with the highest branching ratios and the cleanest signature in the detector.

RESULTS

The plots in Fig. 3 are the combined 90 % C.L. sensitivity lines for the ND (LArTPC + HPArTPC). Only the results for the channels $N \to \mu\pi$ $N \to \nu ee$ for $|U_{\mu 4}|^2$, $N \to e\pi$ and $N \to \nu ee$ for $|U_{e4}|^2$ are shown. They corresponds to exclusion regions that could be placed by the experiment if no signal is observed. The contours are defined following the procedure described in [10] and the results are overlaid with currents bound and the prediction for SBN. An overall improvement up to one order of magnitude in the sensitivity is expected for all the mass range. In the absence of signal, the ND will be able to lower the limits for both mixing parameters:

$$|U_{e4}|^2 \leq 1 \times 10^{-9} \quad \text{for} \quad 0.15\ \text{GeV} \lesssim m_N \lesssim 0.5\ \text{GeV} \tag{6}$$

$$|U_{\mu 4}|^2 \leq 1 \times 10^{-9} \quad \text{for} \quad 0.25\ \text{GeV} \lesssim m_N \lesssim 0.4\ \text{GeV} \tag{7}$$

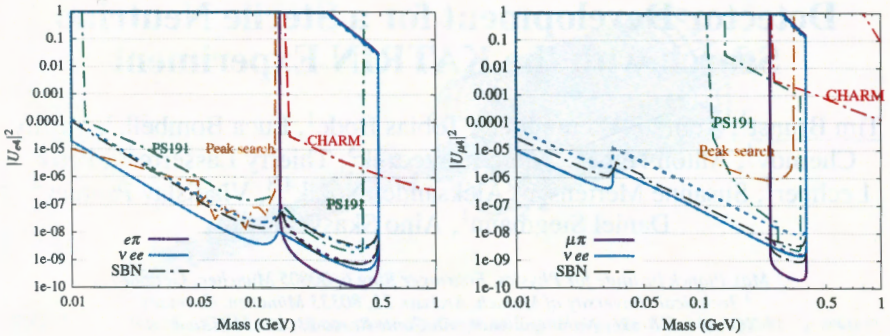

FIGURE 3. Sensitivity to $|U_{e4}|^2$ studying the decay modes $N \to e\pi$ and $N \to \nu ee$ for $|U_{e4}|^2$ (left) and the decay modes $N \to \mu\pi$ and $N \to \nu ee$ for $|U_{\mu 4}|^2$ (right). The solid lines corresponds to the analysis before the background analysis ($W_d = 1$). The dotted lines are drawn after the background analysis. The current limits are also shown for comparison.

The other decay channels have also been studied, leading to similar results, even though they are more challenging from an experimental point of view either because of a lower branching ratio or because they suffer more from irreducible background. Some of the three body decay modes, $N \to \nu ee$, $N \to \nu\mu\mu$ and $N \to \nu\pi^0$, are conducted also by neutral current interaction and are therefore sensitive to the less constrained $|U_{\tau 4}|^2$.

ACKNOWLEDGMENTS

This work is supported by the European Research Council under ERC Grant "NuMass" (FP7-IDEAS-ERC ERC-CG 617143).

REFERENCES

1. Y. Fukuda et al. (Super-Kamiokande Collaboration) *Phys. Rev. Lett.* **81**(5), 1562 (1998).
   B. Aharmim et al. (SNO Collaboration) *Phys. Rev. C* **72**(5), 055502 (2005).
2. S. Gariazzo, C. Giunti, M. Laveder, Y. F. Li, and E. M. Zavanin, *J. Phys. G* **43**(3), 033001 (2016).
3. T. Asaka, M. Shaposhnikov, *Phys. Lett. B* **620**, 17 (2005).
4. A. Atre, T. Han, S. Pascoli, and B. Zhang, *J. High Energ. Phys.* **0905** (2009) 030.
5. E. Kh. Akhmedov, A. Yu. Smirnov, *Phys. Atom. Nucl.* **72**, 1363 (2009).
6. G. Bernardi, G. Carugno, J. Chauveau et al., *Phys. Lett. B* **166**(4), 479 (1986).
   G. Bernardi, G. Carugno, J. Chauveau et al., *Phys. Lett. B* **203**(3), 332 (1988).
7. M. Drewes, B. Garbrecht, *Nucl. Phys. B* **921**, 250 (2017).
8. P. Ballett, S. Pascoli, and M. Ross-Lonergan, *J. High Energ. Phys.* (2017) **2017**, 102.
9. R. E. Shrock, *Phys. Rev. D* **24**, 1275 (1981).
10. G. J. Feldman and R. D. Cousins, *Phys. Rev. D* **57**(7), 3873 (1998)

Detector Development for a Sterile Neutrino Search with the KATRIN Experiment

Tim Brunst[1], Konrad Altenmüller[2], Tobias Bode[1], Luca Bombelli[3], Vasiliy Chernov[4], Anton Huber[5], Marc Korzeczek[5], Thierry Lasserre[2,6], Peter Lechner[7], Susanne Mertens[1,2], Aleksander Nozik[4,8], Vladislav Pantuev[4], Daniel Siegmann[1], Aino Skasyrskaya[4]

[1] *Max Planck Institute for Physics, Föhringer Ring 6, 80805 München, Germany*
[2] *Technical University of Munich, Arcisstr. 21, 80333 München, Germany*
[3] *XGLab srl, Bruker Nano Analytics, Via Conte Rosso 23, 20134 Milano, Italy*
[4] *Institute for Nuclear Research of Russian Academy of Sciences, Prospekt 60-letiya Oktyabrya 7a, Moscow 117312, Russian Federation*
[5] *Karlsruhe Institute of Technology, Hermann-von-Helmholtz-Platz 1, 76344 Eggenstein-Leopoldshafen, Germany*
[6] *Centre CEA de Saclay, 91191 Gif-sur-Yvette cedex, France*
[7] *Halbleiterlabor of the Max Planck Society, Otto-Hahn-Ring 6, 81739 München, Germany*
[8] *Moscow Institute of Physics and Technology, 9 Institutskiy per., Dolgoprudny, Moscow Region, 141700, Russian Federation*

Abstract. The KATRIN (Karlsruhe Tritium Neutrino) experiment investigates the energetic endpoint of the tritium β-decay spectrum to determine the effective mass of the electron anti-neutrino with a precision of 200 meV (90% C.L.) after an effective data taking time of three years. The TRISTAN (tritium β-decay to search for sterile neutrinos) group aims to detect a sterile neutrino signature by measuring the entire tritium β-decay spectrum with an upgraded KATRIN system. One of the greatest challenges is to handle the high signal rates generated by the strong activity of the KATRIN tritium source. Therefore, a novel multi-pixel silicon drift detector is being designed, which is able to handle rates up to 10^8 cps with an excellent energy resolution of < 200 eV (FWHM) at 10 keV. This work gives an overview of the ongoing detector development and test results of the first seven pixel prototype detectors.

Keywords: silicon drift detector, sterile neutrinos, KATRIN, TRISTAN, Troitsk ν-mass
PACS: 07.77.−n, 14.60.St, 29.40.Wk, 95.55.Vj

INTRODUCTION

Sterile neutrinos. The nature of dark matter in our universe is still unknown. Despite overwhelming cosmological evidence for its existence, a direct detection is pending. One promising candidate is a keV-scale sterile neutrino [1]. Several theories predict sterile neutrinos within a minimal extension of the Standard Model of particle physics (SM). These fermions would not even interact weakly, but would mix with active neutrinos. TRISTAN, as an extension of the KATRIN experiment, could therefore be able to discover such a neutrino by observing the signature of the heavy mass-eigenstate mixing in the tritium β-decay spectrum.

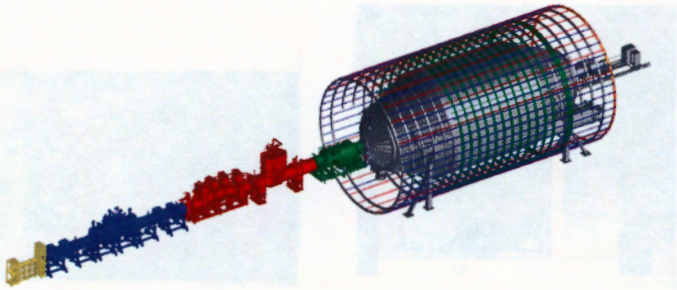

FIGURE 1. The KATRIN experiment consists of rear wall (*yellow*), WGTS (*blue*), pumping section (*red*), pre-spectrometer (*green*), main spectrometer and detector section (both *grey*).

The Karlsruhe Tritium Neutrino experiment. Starting mid 2018 the Karlsruhe Tritium Neutrino (KATRIN) experiment [2] will investigate the endpoint region of the tritium β-decay spectrum in order to determine the absolute neutrino mass (see figure 1). KATRIN combines a high-activity gaseous tritium source with a high-resolution spectrometer. First, tritium gas decays in a windowless gaseous tritium source (WGTS). The electrons are adiabatically guided by magnetic fields throughout the whole setup. The tritium is pumped out by turbo molecular and cryogenic pumps and then recycled. Using the MAC-E filter technique, only β-electrons that pass a certain energy threshold pass the pre- and main spectrometer and are counted by a detector. The rear wall collects all electrons that do not reach the detector and defines the ground potential.

Unlike the neutrino mass, which manifests itself only at the endpoint region of the β-decay, the signature of a keV-scale sterile neutrino may appear anywhere in the spectrum depending on the exact mass of the sterile neutrino. Accordingly, the TRISTAN project aims to detect the entire tritium β-decay spectrum. In this case, electrons of all energies shall pass to the detector. Since the KATRIN detector is not designed to handle such high count rates, a novel detector has to be constructed.

A NOVEL DETECTOR

The novel detector has to fulfill the following requirements:

Excellent energy resolution: In order to be sensitive to the sterile neutrino signal in a differential measurement of the electron energy, an excellent energy resolution of the detector (300 eV full width at half maximum (FWHM) @ 20 keV) and a low detection threshold (1 keV) are required. To this end, a dead layer thickness of less than 100 nm is necessary.

Handling of high rates: In order to reach a statistical sensitivity of 10^{-6} in three years a signal rate of 10^8 cps is necessary. A count rate in the order of 10^5 cps is manageable for modern data acquisition systems. Thus the detector has to be segmented into $\sim 10^3$ pixels with a count rate of 10^5 each.

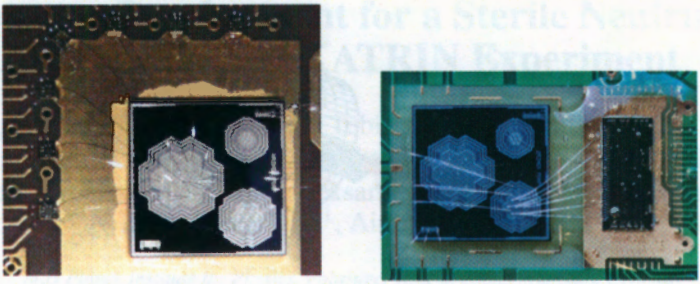

FIGURE 2. Seven pixel prototype detectors of different sizes equipped with XGLab (*left*) and CEA Saclay (*right*) read-out electronics.

Large area coverage: To mitigate charge sharing from neighboring pixels the pixel diameter should not be smaller than 2 mm. In order to maintain a high energy resolution even with these large pixels, a small capacitance for each pixel is required.

These requirements point to a silicon drift detector (SDD) array design.

The silicon drift detector

The silicon drift detector measures the amount of ionization of incoming particles in the detector material. The cathode covers the complete entrance window. The point-like anode, however, provides small capacitance for each pixel and thus low noise at short shaping times, i.e. at high rates. Each pixel is equipped with a number of drift rings operated at different potentials which facilitate the transport of the signal charge carriers to the anode. At the same time, these rings divide the monolithic detector chip into pixels reducing the dead area per chip to a negligible level.

First prototypes

Several silicon drift detector prototype chips with seven hexagonal pixels in different sizes (0.5, 1 and 2 mm in diameter) and a thickness of 450 μm have been produced at the semiconductor laboratory of the Max Planck society in Munich[1]. They were equipped with two different read-out systems from XGLab, Italy, and CEA Saclay, France (see figure 2). In both cases, the measured charge is transferred into a voltage by a charge sensitive amplifier (CSA) placed on an application specific integrated circuit (ASIC) for further processing. The XGLab system is optimized for 1-channel SDD detectors, whereas the CEA system allows to operate all channels synchronously. By comparing

[1] https://www.hll.mpg.de/

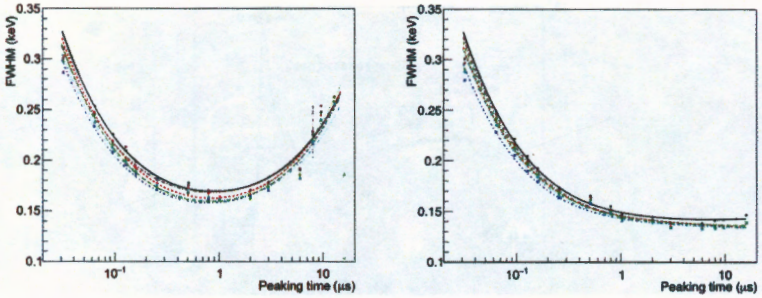

FIGURE 3. Noise curve at room temperature (*left*) and at −30 °C (*right*) for all seven pixels. The noise contribution of leakage current is reduced at low temperature allowing for longer peaking times with better energy resolution.

two different systems, the influence of the read-out electronics on the measured signals and hence systematic effects can be investigated.

Characterization

The characterization of the systems was performed with radioactive ^{55}Fe and ^{241}Am γ-sources (among others). The FWHM was measured as a function of peaking time at different temperatures (see figure 3). The peaking time is defined as the time from 5 % of the maximum to the maximum of the shaped signal. The best energy resolution for 2 mm pixel detectors was obtained with a peaking time of 0.8 μs at room temperature (163 eV FWHM) and 2 μs at −30 °C (142 eV FWHM) respectively.

Systematic effects

The final setup is being designed to measure electrons in the keV-range. These show a different response to the detector than photons. As electrons are massive particles, the systematic effects, such as the influence of the dead layer, back-scattering, charge sharing and others play a major role and are currently investigated. The effect of some of these systematics is depicted in figure 4.

entrance window: The dead layer is a layer on the detector entrance window which consists of an unavoidable SiO_2 oxidation layer ($\sim$ 10 nm) created by contact with air. Furthermore, the p^+ implantation needed for applying the back-contact voltage prevents the electric field to reach the very surface of the detector. Charge carriers that are generated in this layer are not efficiently drifted to the read-out anode. Unlike photons, electrons are not absorbed in their first interaction but continuously lose energy on their way through the detector material. This leads to a certain amount of energy that is always lost in the dead layer.

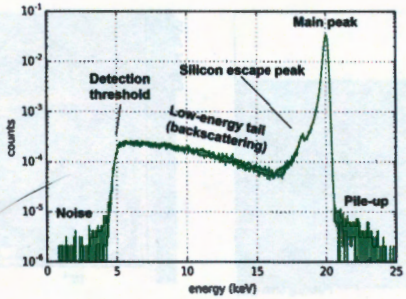

FIGURE 4. Spectrum of mono-energetic electrons with 20 keV. Clearly visible are effects from pile-up, silicon escape energy, back-scattering, detection threshold and noise. Note the logarithmic y-axis.

back-scattering: Electrons have a certain probability to enter the detector, deposit parts of their energy in scattering processes and leave the detector again through the entrance window. Their remaining energy is left undetected. This leads to a low-energy back-scattering background in the measured spectrum.

charge sharing: If an electron hits the detector at the border between two adjacent pixels, the created charge cloud is divided by the electric fields and drifted to the respective anodes. This creates a signal in both pixels with the corresponding part of the initial electron energy. If the effect is well understood, the initial energy can be reconstructed as the sum of energies detected in both pixels.

pile-up: It can happen that two electrons arrive at one pixel within the signal rise time of around 30 ns. This time difference is too short for the read-out electronics to distinguish between the two events. They will be counted as one event with the sum of the energy of both electrons. For a mono-energetic source this leads to a second line in the spectrum at two times the energy.

First tritium data

In May/June 2017 a 1 mm prototype detector with CEA read-out electronics was installed at the Troitsk ν-mass experiment (see figure 5). As one of KATRIN's technological predecessor it offers the possibility to investigate systematic effects in a real experimental environment. First tritium data were taken (see figure 6) as well as mono-energetic electron data from the inner electrode system and an electron gun. This not only allowed for further detector characterization, but also for testing the complete TRISTAN analysis chain including spectral fitting, background control and so forth.

CONCLUSION AND OUTLOOK

The TRISTAN group aims to detect a sterile neutrino signature by measuring the tritium spectrum with an upgraded KATRIN system. Therefore, a novel silicon drift detector

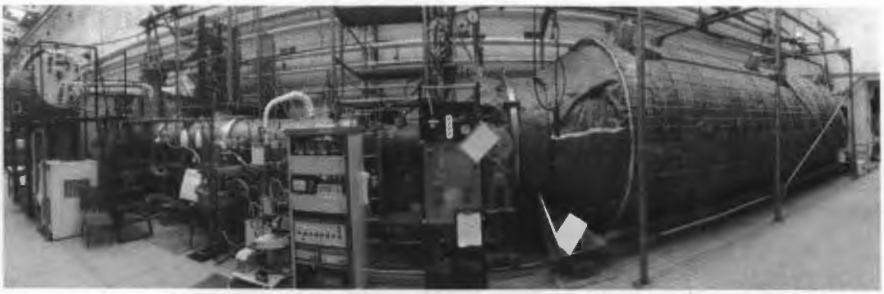

FIGURE 5. The Troitsk ν-mass experiment holds the world leading limit on the neutrino mass from a direct measurement [3]. The collaboration is now searching for a kev-range sterile neutrino.

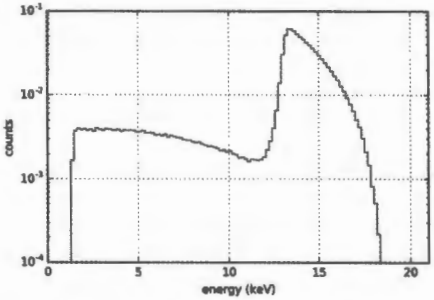

FIGURE 6. A differential tritium spectrum measured at the Troitsk ν-mass experiment. The retarding potential of the spectrometer was set to 13 keV. The back-scattering background is increased by electrons that were back-reflected at the retarding potential or magnetic mirrors in the setup.

system is being developed. First prototypes have been produced. Their functionality has been successfully demonstrated and first detailed measurements to study systematic effects have been performed.

The characterization of the seven-pixel prototype detectors continues with electron and photon source of different types, e.g. an evaporated Rubidium/Krypton source. A second measurement at the Troitsk ν-mass experiment will be performed with the XGLab read-out electronics system in November 2017. The production of the next prototype generation will start in the beginning of 2018 as an array of 166 pixels with 3 mm pixel diameter and integrated JFETs as a first signal amplification stage. The final detector is planned to be an array of 20 of such detector modules. It will be applied to the KATRIN setup in approximately five years when the neutrino mass measurements are completed.

ACKNOWLEDGMENTS

This work was supported by the Max Planck Society (MPG) and the Technical University Munich (TUM). We would like to thank the Institute for Nuclear Research of the Russian Academy of Sciences (INR RAS) and the Halbleiterlabor der Max-Planck-Gesellschaft for the fruitful cooperation. Tim Brunst would like to thank the Joint Institute for Nuclear Research (JINR) and the Czech Technical University (CTU) for their hospitality.

REFERENCES

1. R. Adhikari et al., *Journal of Cosmology and Astroparticle Physics* **2017**, 025 (2017).
2. KATRIN collaboration, J. Angrik et al., KATRIN Design Report 2004, *FZKA Scientific Report 7090*, 025 (2005).
3. V. N. Aseev, A. I. Belesev, A. I. Berlev et al., *Phys. Atom. Nuclei* **75**, 464 (2012).

Simulation of high energy neutrino events for Baikal GVD telescope

Ioana Caracas[1,2] and Rastislav Dvornický[1,3]

[1] *Dzhelepov Laboratory of Nuclear Problems, JINR Dubna, 141980 Dubna, Moscow region, Russia*
[2] *Faculty of Physics, University of Bucharest, Bucharest-Magurele, POBox MG 11, Romania*
[3] *Department of Nuclear Physics and Biophysics, Comenius University, Mlynská dolina F1, SK-842 48 Bratislava, Slovakia*

Abstract. We present Monte Carlo simulations of high energy neutrino events for the underwater neutrino telescope Baikal GVD. The numerical results were obtained by means of the package ANIS. The main aim is to obtain MC simulations for all flavors of neutrinos up to energies as high as 10^{12} GeV.

Keywords: high energy neutrinos, Monte Carlo simulations, Baikal GVD

INTRODUCTION

The natural high-energy neutrino fluxes are produced by physical processes in astrophysical objects characterized by enormous energy release at rates from 10^{39} to 10^{52} erg/s or higher. The main sources of these neutrinos are divided into two categories: Galactic and Extragalactic sources. Among the Galactic sources there are, e.g., supernova remnants, pulsars, the neighborhood of a black hole at the Galactic center, binary systems containing a black hole or a neutron star. On the other hand among the Extragalactic sources are classified, e.g. active galactic nuclei (AGN), gamma-ray bursts (GRB), starburst galaxies and galaxy clusters.

The detection of high energy neutrinos with the next generation neutrino telescope, Baikal GVD (Gigaton Volume Detector), will help in studying astrophysical neutrino fluxes and mapping the sky in the Southern Hemisphere including the region of the galactic center. The Baikal GVD is together with other experiments IceCube and KM3NeT one of the three current biggest large-scale next-generation neutrino telescopes in the world.

The goal of this contribution is to present the preliminary results of Monte Carlo simulations using the package ANIS (All Neutrino Interaction Simulation) based on the c++ code [1]. High energy neutrinos are simulated at the Earth's surface and then propagated through the Earth. Here, all standard model processes are taken into account, e.g. charge currents (CC), neutral currents (NC), and Glashow resonance (GR). Eventually, neutrinos interactions are simulated within a specified volume in the vicinity of the detector.

DETECTION PRINCIPLE

There are two main reasons why neutrinos serve as perfect cosmic probes:

i) They are not influenced by the cosmic electromagnetic fields unlike the charged particles. Therefore they point directly to the origin of their creation and can reveal the sources of great energy release in the Universe.

ii) Unlike the electromagnetic radiation (visible light, UV/IR radiation, X-rays, etc.) which can be scattered or absorbed they interact rarely so they can penetrate great distances from the deep Universe.

High-energy cosmic neutrinos of all flavors ($l = e, \mu, \tau$) interact in the target material of neutrino telescopes mostly with nucleons (N) through the charged (CC) and neutral currents (NC) producing the Cherenkov light:

$$\begin{aligned} CC &: \nu_l(\bar{\nu}_l) + N \rightarrow l^-(l^+) + hadrons \\ NC &: \nu_l(\bar{\nu}_l) + N \rightarrow \nu_l(\nu_L) + hadrons \end{aligned} \tag{1}$$

The interaction of neutrinos with target electrons makes virtually no contribution to the total number of recorded events, except for the resonant scattering of electron antineutrinos in the W-resonance region:

$$\bar{\nu}_e + e^- \rightarrow W^- \rightarrow anything \tag{2}$$

According to the flavor of neutrinos there are two different types of detection topologies in neutrino telescope: Cherenkov cone for muon (μ) tracks and spherical Cherenkov front for the cascades generated after electron (e) and tau (τ) interactions in the water target. As neutrinos have a very small interaction cross section, in order to be detected

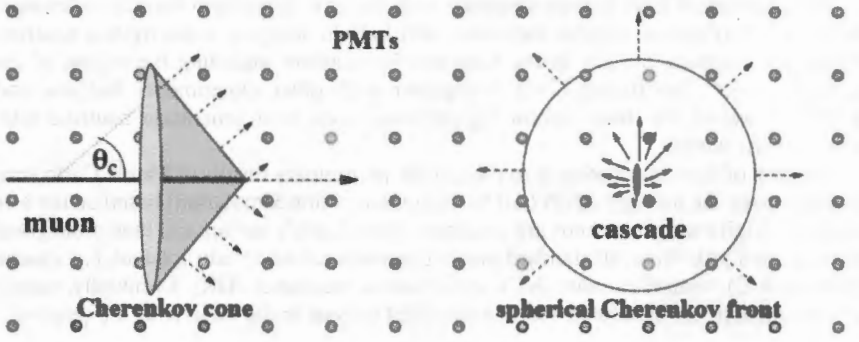

FIGURE 1. The two different types of detection topologies in underwater neutrino telescopes. The left panel displays the Cherenkov cone for muon (μ) track and the right panel the spherical Cherenkov front for the cascades generated after electron (e) or tau (τ) detection.

there is a need for a large detection volume.

THE BAIKAL GVD TELESCOPE

The Baikal detector is situated in the lake Baikal, Russia, at a depth of 1366 m and a distance of 3600 m from the shore. The detector will utilize Lake Baikal water instrumented at depth with light sensors that detect the Cherenkov radiation from secondary particles produced in interactions of high-energy neutrinos inside or near the instrumented water volume. The first Baikal neutrino experiment was initiated on the 1st of October 1980. The first stationary string of optical modules (GIRLANDA-84) was deployed in 1984 and shortly after was followed by the second string (GIRLANDA-86). The first large-scale deep underwater neutrino telescope, NT200, was gradually deployed from 1993 to 1998 and subsequently extended to NT200+ from 2003 to 2005.

The project Gigaton Volume Detector is the logical extension of more than 30 years of experience with the detection of high energy atmospheric and cosmic neutrinos in the lake Baikal. The first strings of the cluster "Dubna" were deployed in April 2011. In 2016 this cluster was upgraded to the baseline configuration which comprises 288 optical modules (OMs) arranged in eight strings. The second full-scale GVD-cluster was deployed and put in operation in 2017. In its final stage, the GVD detector will consists of 2 304 Optical Modules (OM) arranged to 8 clusters of strings submerged in the lake Baikal. Each cluster consists of eight 705 m long strings at depths of 600 to 1300 m below the surface. The clusters will be spaced over an area of ≈ 0.55 km^2 and the water volume instrumented by OM will be about 0.4 km^3 .

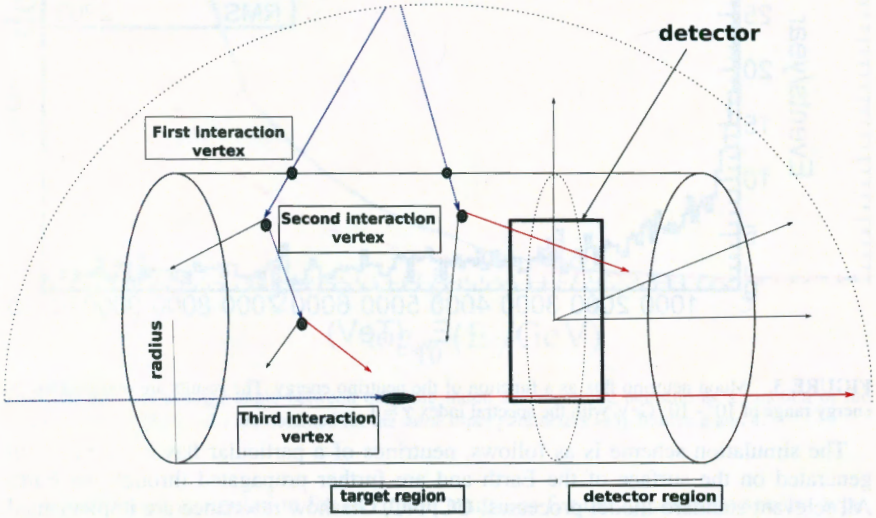

FIGURE 2. The neutrino event with more interaction vertices is illustrated in the vicinity of the detection volume.

The main detection element of the telescope is the optical module. It consists of 17" glass pressure-resistant sphere, electronics (amplifier, HV, controller), 2 calibration LED flashers, μ-metal cage, and photomultiplier R7081HQE fixed with elastic gel.

These OMs are used to detect light produced in the interactions of particles with the water. They are designed to convert the Cherenkov radiation of muons and showers into electric signals. The two main parameters are the amount of the detected light, and the time distribution of the signal (See reference [2]).

SIMULATIONS

The MC simulations of the neutrino events in the vicinity of the detector have been accomplished by means of the package ANIS, which is is a Monte Carlo neutrino event generator for high energy neutrino telescopes. The program is written in c++ and uses the vector package of the CLHEP library [3] as well as the HepMC Monte Carlo event record [4]. The input parameters for the evaluation procedure are: energy range, zenith angle, spectral index, type of the neutrino, geometry of the detector. The only type of spectra which is currently implemented is the power-law energy spectra: $\Phi_\nu(E) \propto E^{-\gamma}$. Here, γ stands for the spectral index. However, the code is flexible enough to allow an extension of the spectra type.

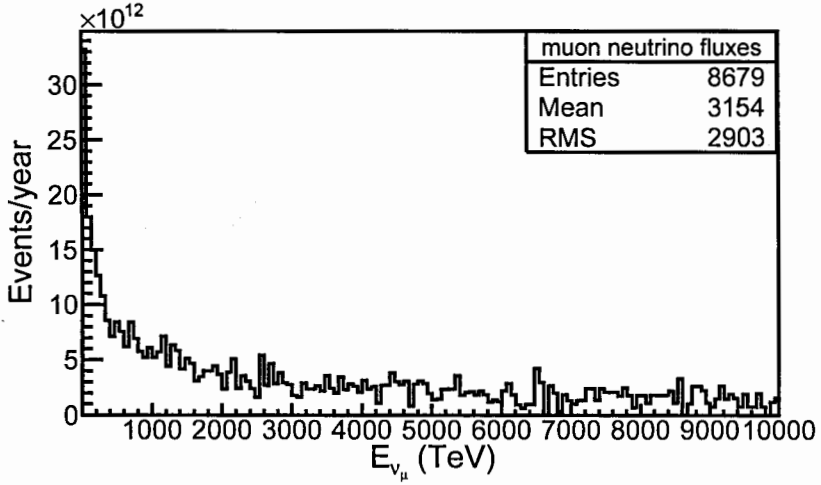

FIGURE 3. Muon neutrino flux as a function of the neutrino energy. The results are obtained for the energy range of 10^2 - 10^7 GeV, with the spectral index $\gamma = 1$.

The simulation scheme is as follows, neutrinos of a particular flavor are randomly generated on the surface of the Earth and are further propagated through the Earth. All relevant standard model processes: CC, NC, Glashow resonance are implemented. In the last step program simulates a neutrino interaction within a specified volume in the vicinity of the detector. The first interaction vertex is generated when the neutrino reaches the detection volume. Depending on the incoming neutrino energy, there could be two or more interaction vertices in a single event. In figure 2, an example of an event with more vertices is illustrated.

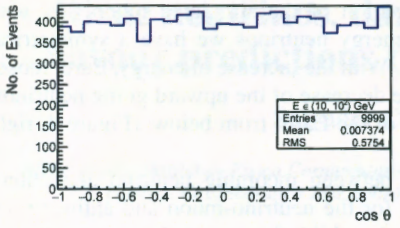

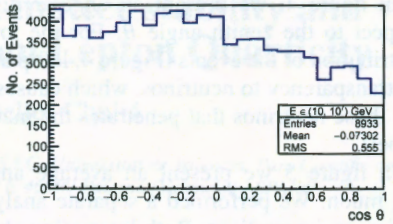

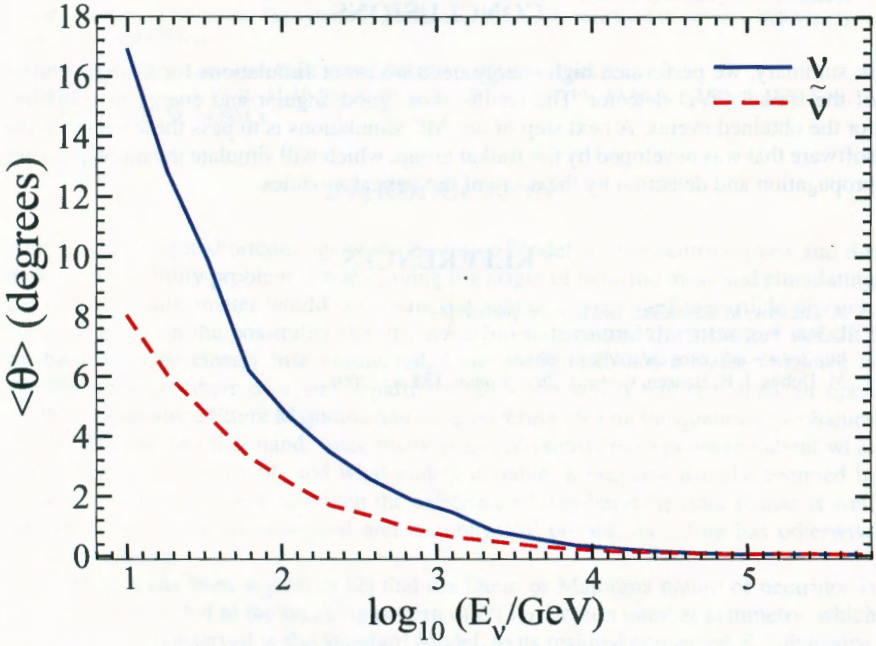

FIGURE 5. The average angle between outgoing muon and incoming neutrino as a function of the neutrino energy. The results are obtained for the same input parameters as in figures 3 and 4.

We performed a simulation for the muon neutrinos for the logarithmic spectra type, i.e. $\gamma = 1$. The distribution of the ν_μ flux as a function of the neutrino energy is shown in figure 3. The normalization is chosen such as we will have the total number of events per year in the detection volume of a single cluster of the GVD telescope.

We can see that, with the increase of energy, the number of the events reaching the detection volume decreases exponentially. This implies that a large number of generated events are needed to obtain events with high energies.

In figure 4, we present an angular distribution of the simulated muon flux with respect to the zenith angle θ. For the low energy neutrinos we have a symmetrical distribution of the events (Figure 4, left panel). With the increase of energy, Earth looses its transparency to neutrinos, which causes the decrease of the upward going neutrinos, i.e. those neutrinos that penetrates the matter of the Earth from below. (Figure 4, right panel).

In figure 5 we present an average angle between incoming neutrino and outgoing muon. We performed a separate analysis for the neutrino-muon and antineutrino-antimuon interactions. Both interacting channels exhibit the same behavior. For the increasing energy the average angle decreases asymptotically to 0.

CONCLUSIONS

In summary, we performed high energy neutrino event simulations for a single cluster of the Baikal GVD detector. The results show good angular and energy distributions for the obtained events. A next step of our MC simulations is to pass these events to the software that was developed by the Baikal group, which will simulate the muon particles propagation and detection by the array of the optical modules.

REFERENCES

1. A. Gazizov, M. Kowalski, *arXiv:astro-ph/0406439*
2. L. Fajt, PoS (ICRC2017) 1036
3. http://www.info.cern.ch/asd/hc++/clhep.
4. M. Dobbs, J. B. Hansen, *Comput. Phys. Comm.* **134**, *41 (2001)*

Dirac neutrinos, dark matter stability and flavour predictions from Lepton Quarticity

Salvador Centelles Chuliá

AHEP Group, Institut de Física Corpuscular – C.S.I.C./Universitat de València, Parc Científic de Paterna, C/ Catedrático José Beltrán, 2 E-46980 Paterna (Valencia) - SPAIN

Abstract. We propose to relate dark matter stability to the possible Dirac nature of neutrinos. The idea is illustrated in a simple scheme where small Dirac neutrino masses arise from a type-I seesaw mechanism as a result of a Z_4 discrete lepton number symmetry. The latter implies the existence of a viable WIMP dark matter candidate, whose stability arises from the same symmetry which ensures the Diracness of neutrinos. The symmetry groups Δ_{27} and A_4 are then used to extract a rich variety of flavour predictions.

Keywords: Dirac neutrinos, Dark Matter, Flavour predictions, Quarticity
PACS: 11.10.-z, 11.15.-q, 11.15.Ex, 11.30.-j, 11.30.Fs, 12.15.Ff, 12.60.-i, 12.90.+b, 13.15.+g, 14.60.Pq, 14.60.St, 14.80.Cp

INTRODUCTION

Amongst the major shortcomings of the Standard Model are the neutrino mass and the dark matter stability problem. Underpinning the origin of neutrino mass and elucidating the nature of dark matter would constitute a gigantic step forward in particle physics. Here we focus on the possibility that the **neutrino nature and dark matter stability problem may be closely interconnected**. Concerning neutrinos a major unknown is whether they are their own anti - particles, an issue which has remained an open challenge ever since Ettore Majorana had his pioneering idea on the quantum mechanics of spin [1]. On the other hand, since many years, physicists have pondered about what is the dark matter made of, and what makes it stable, a property usually assumed in an ad-hoc fashion. Indeed, although the existence of non-baryonic dark matter is well established by using cosmological and astrophysical probes, its nature has otherwise remained elusive.

Recently it has been argued in [2] that the Dirac or Majorana nature of neutrinos is intimately connected to the breaking pattern of $U(1)_L$ Lepton number symmetry, which is accidentally conserved in the Standard Model, to its residual conserved Z_n subgroups. Interestingly enough, neutrinos can only be Majorana for specific Z_n groups and even within these specific Z_n groups, only for special choices of the charges, while they will be Dirac in any other case. Here we focus on the $U(1)_L \to Z_4$ scenario, which we call **Quarticity**. We show that **a WIMP dark matter candidate can naturally emerge, stabilized by Quarticity, the same symmetry associated to the Diracness of neutrinos**. Moreover, the smallness of neutrino masses can be understood through the Dirac analogue of type-I seesaw. We also show that many different symmetry groups can be used to give the flavour structure of neutrino mixings and therefore **a rich**

variety of models arise, showing different features and predictions but all maintaining the principal result, **the connection between Dark Matter and the Dirac nature of neutrinos.**

THE MODEL

The general structure of the model is given in [3]. Concerning the particle content of the model, we need to introduce some new fields in addition to those in the Standard Model. In the fermionic sector we introduce **3 generations of right handed neutrinos**, $\nu_{i,R}$, to obtain neutrino masses, as well as **3 more generations of heavy neutral leptons** with the two chiralities, which we will call $N_{i,L}$ and $N_{i,R}$, in order to have a seesaw mechanism. We also have to introduce a new scalar, χ, which has a **non - zero vev**. In addition there are two other scalars carrying non-trivial Z_4 charges, a real scalar η, and a complex scalar ζ, which is the **DM candidate**. All of them are gauge singlets. The set of transformation rules under Z_4 for the fields in the model is:

TABLE 1. Charge assignments for leptons, quarks, scalars (Φ_i^u, Φ_i^d and χ_i) as well as "dark matter sector" (ζ and η). Here $\mathbf{z}$ is the fourth root of unity, i.e. $\mathbf{z}^4 = 1$.

Fields	Z_4	Fields	Z_4
Fermions			
$\bar{L}_{i,L}$	$\mathbf{z}^3$	$\nu_{i,R}$	$\mathbf{z}$
$l_{i,R}$	$\mathbf{z}$	$\bar{N}_{i,L}$	$\mathbf{z}^3$
$N_{i,R}$	$\mathbf{z}$		
Scalars (vev $\neq$0)			
Φ	1	χ	1
Scalars (vev=0)			
ζ	$\mathbf{z}$	η	$\mathbf{z}^2$

The only requirement for the flavour structure of the model is that **the flavour symmetry group G forbids the tree level neutrino mass**, this is, $\bar{L}\phi^c\nu_R$. Then **neutrino masses are generated via a type-I seesaw.**

Neutrino Diracness

The symmetry rules under Z_4 ensures that neutrinos are Dirac particles by forbidding all the possible Majorana terms at all orders. Note that the scalars which have a non-zero vev, Φ and χ, transform trivially under Z_4, thus implying that **the Quarticity symmetry Z_4 is not spontaneously broken**. Moreover

$$(\Phi^\dagger\Phi)^n\chi^m \sim 1 \tag{1}$$

This implies that if all the Majorana mass terms are forbidden at tree level, then they are forbidden at all orders. This is indeed the case, because **all neutral fermionic field**

transform as z under Z_4. Therefore, all the Majorana masses at tree level are forbidden. For example

$$\bar{\nu}_R^c \nu_R \sim z^2 \tag{2}$$

The higher order mass terms -via non-zero vevs of the scalars Φ and χ- also transform non-trivially under the Quarticity symmetry

$$\bar{\nu}_R^c \nu_R (\Phi^\dagger \Phi)^n \chi^m \sim z^2 \tag{3}$$

Therefore, these terms are forbidden and **neutrinos remain Dirac particles at all orders, while the symmetry Z_4 is not broken after spontaneous symmetry breaking.**

A stable Dark Matter candidate

To ensure that neutrinos remain Dirac particles, the Z_4 Quarticity symmetry should remain exact, so that no scalar carrying a Z_4 charge should acquire any vev. Thus **both ζ and η which carry Z_4 charge can potentially be stable as a result of the unbroken Quarticity symmetry**. However, owing to the Z_4 charge assignments, the η field has cubic couplings to both scalars and fermions. These couplings lead to the decay of η and thus, despite carrying a Z_4 charge, **η is not stable**. On the other hand, in the Lagrangian there is no term of the form $\zeta \rho_i \rho_j$, where ρ is a generic scalar, nor of the form $\zeta \psi_i \psi_j$, where ψ is a generic fermion. This implies that **ζ is an stable particle, thus it is a viable dark matter candidate.**

The detection could be direct, via **nuclear recoil**. The WIMP particle will also contribute to the **invisible decay of the Higgs**. Both features are shown in the following diagrams 1

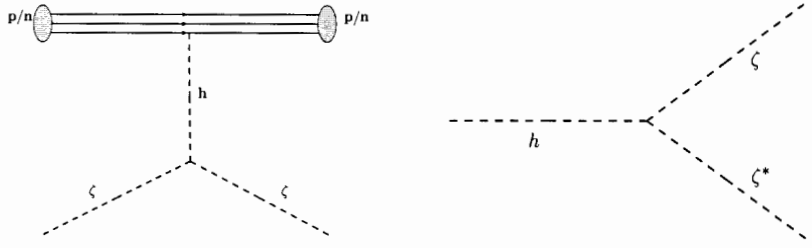

FIGURE 1. Left panel: Leading order Feynman diagram of the nuclear recoil of the dark matter candidate via a exchange of the Higgs boson. Right panel: Tree level Feynman diagram of the invisible decay of the Higgs boson to a pair of DM particles.

The constraints from LHC for invisible decay and the for direct searches coming from LUX experiment rules out part of the parameter space regarding the Higgs-dark matter quartic coupling $\lambda_{h\zeta}$ and mass of dark matter m_ζ, which can be seen in the figure 2.

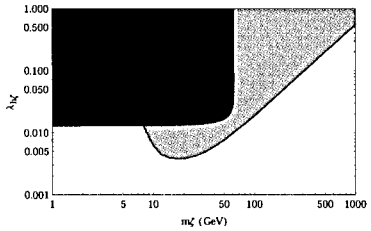

FIGURE 2. Parameter space excluded by LHC invisible decay data and LUX direct searches in the $\lambda_{h\zeta}$ vs m_ζ plane.

FLAVOUR PREDICTIONS

The model includes, apart from the Standard Model gauge group, a global symmetry $Z_4 \otimes G$, where Z_4 is the Quarticity symmetry already discussed while G is the flavour symmetry. It's role is to forbid the tree level coupling between left and right handed neutrinos and this can be trivially done using Z_2, as done in [3]. However, one can use non-Abelian discrete symmetries to extract very interesting flavour predictions

Δ_{27} as flavour symmetry

This model was discussed in [4]. **When we take $\Delta(27)$ as the flavour symmetry,** G, an interesting structure appears in the neutral fields mass matrix, which can then be diagonalized and the masses and mixing parameters can be extracted. The parameters in the model have enough freedom to **fit all the mixing angles and neutrino masses constraints.** The charged assignments are shown in Table 2.

TABLE 2. The $\Delta(27)$ and Z_4 charge assignments for leptons, the Higgs scalars (Φ_i, χ_i) and the dark matter sector scalars (ζ and η). Here $\mathbf{z}$ is the fourth root of unity, i.e. $\mathbf{z}^4 = 1$.

Fields	$\Delta(27)$	Z_4	Fields	$\Delta(27)$	Z_4
$\bar{L}_e$	$\mathbf{1}$	$\mathbf{z}^3$	$\nu_{e,R}$	$\mathbf{1}$	$\mathbf{z}$
$\bar{L}_\mu$	$\mathbf{1''}$	$\mathbf{z}^3$	$\nu_{\mu,R}$	$\mathbf{1'}$	$\mathbf{z}$
$\bar{L}_\tau$	$\mathbf{1'}$	$\mathbf{z}^3$	$\nu_{\tau,R}$	$\mathbf{1''}$	$\mathbf{z}$
$l_{i,R}$	$\mathbf{3}$	$\mathbf{z}$	$\bar{N}_{i,L}$	$\mathbf{3}$	$\mathbf{z}^3$
$N_{i,R}$	$\mathbf{3'}$	$\mathbf{z}$			
Φ_i	$\mathbf{3'}$	$\mathbf{1}$	χ_i	$\mathbf{3'}$	$\mathbf{1}$
ζ	$\mathbf{1}$	$\mathbf{z}$	η	$\mathbf{1}$	$\mathbf{z}^2$

The interesting scenario arises when we consider the following alignment for the vevs of the scalars

$$\langle \Phi_i \rangle = v\,(1,1,1) \tag{4}$$

$$\langle \chi_i \rangle = u\,(1, 1+\varepsilon, 1+\alpha) \tag{5}$$

Where $\varepsilon << 1$. In this limit, one can find a **correlation between the CP violation parameter, δ_{CP} , and the deviation from the alignment limit which is parametrized by ε** . This is shown in the figure 3.

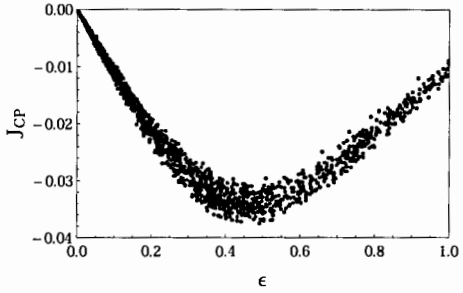

FIGURE 3. Leptonic CP violation phase δ_{CP} versus ε, the deviation from the reference alignment. We have taken $\alpha = 1.2$. See text.

A_4 as flavour symmetry

This realization of the Quarticity model was done in [5]. Taking A_4 **as the flavour symmetry** G gives very different results. On the one hand, the model gives some **strong predictions**

$$\begin{aligned} \theta_{23}^{\nu} &= 45^{\circ}, \qquad \delta^{\nu} = \pm 90^{\circ} \\ \theta_{12}^{\nu} &= \text{arbitrary} \qquad \theta_{13}^{\nu} = \text{arbitrary} \end{aligned} \tag{6}$$

While θ_{12}^{ν} and θ_{13}^{ν} are strongly correlated. However, **this correlation does not allow the fitting of the experimental constraints** for these two angles. The model can be **minimally extended** to include another set of Higgs doublet, which only couples to the up quarks and the neutrinos, while the other Higgs doublet only couples to the d-type quarks and the charged leptons. This way, **not only the mixing parameters can be fitted but also a series of interesting predictions arise.** The charged assignments are

TABLE 3. Charge assignments for leptons, quarks, scalars (Φ_i^u, Φ_i^d and χ_i) as well as "dark matter sector" (ζ and η). Here z is the fourth root of unity, i.e. $z^4 = 1$.

Fields	$SU(2)_L$	A_4	Z_4	Fields	$SU(2)_L$	A_4	Z_4
$\tilde{L}_i$	2	3	z^3	$\nu_{e,R}$	1	1	z
$\tilde{N}_{i,L}$	1	3	z^3	$\nu_{\mu,R}$	1	1′	z
$N_{i,R}$	1	3	z	$\nu_{\tau,R}$	1	1″	z
$l_{i,R}$	1	3	z	$d_{i,R}$	1	3	z
$\tilde{Q}_{i,L}$	2	3	z^3	$u_{i,R}$	1	3	z
Φ_1^u	2	1	1	χ_i	1	3	1
Φ_2^u	2	1′	1	η	1	1	z^2
Φ_3^u	2	1″	1	ζ	1	1	z
Φ_i^d	2	3	1				

A strong correlation between δ_{CP} and δ_{23} appears as shown in figure 4

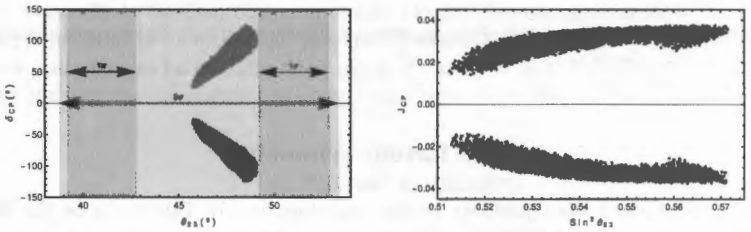

FIGURE 4. CP violation and θ_{23} predictions within the model. Left panel: δ_{CP} vs θ_{23}. The green regions are the 1σ (dark) and 3σ (light) regions for θ_{23} from current oscillation fit. Right panel: Same correlation, now showing J_{CP} vs $\sin^2\theta_{23}$ and zooming in the region allowed by the model, fully consistent in the 2σ experimental range.

Also, **only normal hierarchy of neutrinos is realized**. Moreover, an interesting **relation between the masses of the quarks and the charged leptons** is also present in the model.

$$\frac{m_b}{\sqrt{m_d m_s}} \approx \frac{m_\tau}{\sqrt{m_e m_\mu}} \tag{7}$$

In this case, the flavour symmetry predicts **(i)** a generalized **bottom-tau mass relation** involving all families, **(ii)** small neutrino masses are induced via a **type-I seesaw**, **(iii) CP must be significantly violated** in neutrino oscillations, **(iv)** the atmospheric angle θ_{23} **lies in the second octant** while showing a **strong correlation with** δ_{CP} and **(v)** only the **normal neutrino mass ordering is realized.** A more detailed phenomenological analysis of the oscillation predictions of the model has been recently done in [6].

CONCLUSIONS

We have shown **a very rich family of predictive models** which can accommodate many different setups while conserving the central features of the model, this is

- The Quarticity symmetry Z_4 ensures that neutrinos are Dirac particles and the stability of the DM candidate.
- Naturally small neutrino masses are generated via a type-I seesaw.

Then, the freedom to select the flavour symmetry G leads to a **whole variety of models with rich predictions**, not only in the neutrino sector but also in the quark and charged lepton sector.

ACKNOWLEDGMENTS

This article is based on the poster presentation done in the Pontercorvo school 2017 in Prague. The original works were done in collaboration with José W. F. Valle, Rahul Srivastava and Ernst Ma. Work supported by the Spanish grants FPA2017-85216-P and SEV-2014-0398 (MINECO), PROMETEOII/2014/084 (Generalitat Valenciana) and Severo Ochoa IFIC FPI.

REFERENCES

1. E. Majorana, Nuovo Cim. **14**, 171 (1937).
2. M. Hirsch, R. Srivastava and J. W. F. Valle, arXiv:1711.06181 [hep-ph].
3. S. Centelles Chuliá, E. Ma, R. Srivastava and J. W. F. Valle, Phys. Lett. B **767**, 209 (2017).
4. S. Centelles Chuliá, R. Srivastava and J. W. F. Valle, Phys. Lett. B **761**, 431 (2016).
5. S. Centelles Chuliá, R. Srivastava and J. W. F. Valle, Phys. Lett. B **773**, 26 (2017).
6. R. Srivastava, C. A. Ternes, M. Tórtola and J. W. F. Valle, arXiv:1711.10318 [hep-ph].

Waveform Reconstruction in JUNO

Yaping Cheng[1,2], Michaela Schever[1,3]

[1] *IKP-2 Forschungszentrum Juelich, Germany*
[2] *Institute of High Energy Physics, Beijing, China*
[3] *RWTH Aachen University, Germany*

Abstract. The Jiangmen Underground Neutrino Observatory (JUNO) is a 20 kt Liquid Scintillator detector located at Kaiping, Jiangmen in South China [1]. JUNO is designed to solve the neutrino mass hierarchy problem, one of the most important open issues in neutrino physics. An energy resolution of 3% at 1 MeV is required to distinguish between the mass hierarchies by spectral analysis. Since JUNO will employ a 1 GHz Flash-ADC digitizing readout scheme, extracting charge and time information from the recorded waveforms will be one of the key tasks in data analysis. In this proceedings, two basic waveform reconstruction methods are demonstrated.

Keywords: FADC, Waveform Fitting, Deconvolution
PACS: 84.30.Sk, 02.70.-c

INTRODUCTION

The JUNO experiment is a 20 kton multi-purpose underground liquid scintillator detector. The primary scientific goal is the determination of the neutrino mass hierarchy relying on an excellent energy resolution. The electron antineutrino from reactors is detected via the inverse β-decay(IBD) reaction. It interacts with proton in the Liquid Scintillator and releases a positron and a neutron. The positron and neutron provide a distinctive antineutrino signature by the prompt and delayed signal coincidence. The prompt signal is from positron and the delayed signal is from neutron captured on proton after a mean time of 200 μs.

Approximately 18,000 20-inch PMTs will be used in JUNO central detector to detect the photons, converting the photons passing through the photocathode to photoelectrons (p.e.). The output signal of the PMT will be sampled by the 1 GHz Flash-ADC (FADC) in JUNO readout electronics system. The DAQ will transmit the digitized waveform to the storage. Offline waveform reconstruction algorithms will reconstruct the charge and time of the hits on each PMT from the sampled waveforms. Then, higher level analysis such as energy and vertex reconstruction can be done by dedicated algorithms using the reconstructed charge and time of hits as input.

WAVEFORM RECONSTRUCTION METHODS

At present, there are three waveform reconstruction algorithms in the JUNO offline framework [2]. The charge integration method calculates the area of the pulse region, i.e., the sum of ADC values for points in the pulse region. This method is straightforward

and suffers from systematic errors due to the presence of overshoot in PMT waveforms. In this proceedings, we will focus on the template-fitting and the deconvolution method.

Template-fitting method

Waveform template-fitting is expected to be used for small samples such as events that pass the IBD selection criteria to obtain the hit time and charge from the sampled PMT waveforms.

The single p.e. (spe) response of each PMT is called the template, and its building process is as follows:

- Use ~2000 single p.e. waveforms and align them with respect to the point, where the waveform changes fastest, i.e. the maximal point of first derivative.
- Get the average profile as a template.

This template building method is effective based on Monte Carlo (MC) tests, shown in Figure 1. True spe response can be extracted using randomly distributed waveforms with noise and amplitude fluctuation, as seen in the right part of Figure 1.

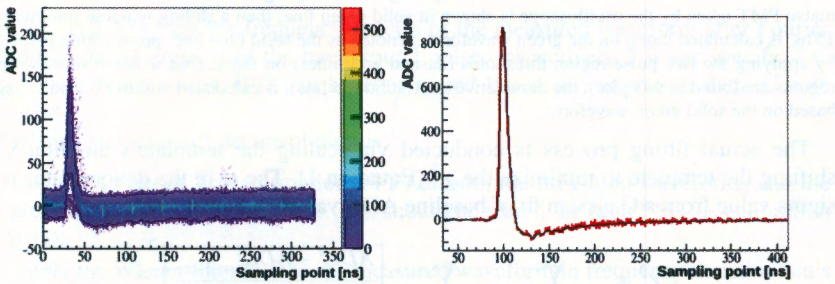

FIGURE 1. Sanity check of the construction of the spe template. Left plot: aligned MC waveforms. Right plot: comparison of derived template (black) and true spe model in MC (red).

The actual fitting based on the built spe template is performed in the pulse-fitting region. The pulse-fitting region is chosen according to two thresholds: the pulse-region start and end threshold. We select the pulse region to avoid doing waveform fitting in the region where only baseline fluctuations exist. A sum of ADC values within a fixed length time window is calculated at each sampling point. This is called the sliding window sum. Then the pulse-fitting region is determined based on the two thresholds, as illustrated in Figure 2. The length of the sliding window and the two thresholds should be tuned based on the real waveform shape, such as the width and the rising time of the waveform. Here, we show the tuned results for 20-inch Hamamatsu PMT R12860. The sliding window length, L, is chosen to be 15 ns. The pulse region start threshold is chosen to be $5 \times \sqrt{L} \times RMS$. Here the RMS is the value characterizing the waveform baseline fluctuation, in our case, it's 0.3 mV. The end threshold is chosen to be $RMS \div \sqrt{L}$. In Figure 2, there are two pulse regions. The start and end position for each pulse region is determined as the yellow and magenta circle, respectively. Inside each pulse region,

a cumulative sum of the ADC values of the sampled waveform is calculated to estimate roughly how many p.e. are in this pulse region, and this serves as the initial charge for the actual fitting. The initial hit time is estimated using the x-axis values of the n+1 equal diversion points for the cumulative sum, n is the integer part of estimated p.e. number.

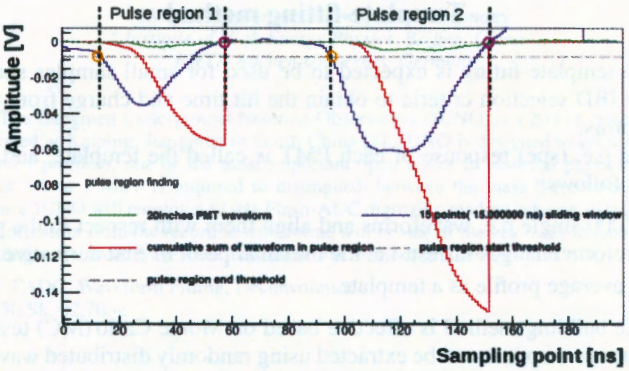

FIGURE 2. Illustration of the method defining the pulse-fitting region: the waveform of 20-inch Hamamatsu PMT taken by the oscilloscope is shown in solid green line; then a sliding window sum, with L = 15 ns, is calculated based on the green waveform, denoted as the solid blue line; pulse region is searched by applying the two pulse-region thresholds (dashed grey lines) on the sliding window sum (two pulse regions are found in this plot); the cumulative sum (solid red line), is calculated within each pulse region, based on the solid green waveform.

The actual fitting process is conducted via scaling the template's amplitude and shifting the template to minimize the χ^2 (Equation 1). The σ in the denominator is the sigma value from a Gaussian fit of baseline ADC values.

$$\chi^2 = \sum_{(pulse\ region)} \sum_{(i^{th}\ sample)} \left[\frac{ADC^i - ADC^i_{template}}{\sigma} \right]^2 . \quad (1)$$

In case of multiple p.e., multiple pulse regions can be found. The fitting is then performed in each pulse region separately. In one fit, the already fitted pulse region is substracted from the whole waveform. The fitting can become very time-consuming if the whole readout window is not split into several fitted regions.

Deconvolution method

The deconvolution method is based on the fact that the final observed waveform is the convolution of the hit distribution with the PMT spe response. Deconvolution is the reverse of convolution. Since we can get prior knowledge of the spe response, we can get the hit distribution by deconvolving the spe response from the sampled waveform. Due to the presence of noise in the measurements, a noise filter should be applied to select the signal and suppress the noise before carrying out the deconvolution. One possible choice is the Wiener filter, as shown in Figure 3.

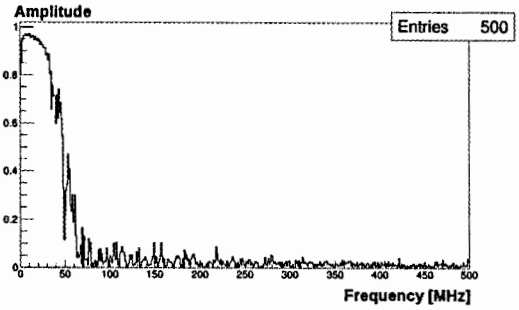

FIGURE 3. Example of the Wiener filter H(f).

The Wiener filter H(f) is deployed in the frequency domain and can be written as:

$$H(f) = \frac{|S(f)|^2}{|S(f)|^2 + |N(f)|^2}. \tag{2}$$

Here $S(f)$ and $N(f)$ are the frequency spectra of the measured waveform after Fourier transformation for signal and the background noise, respectively, f is the specific frequency. The Wiener filter H(f) can be constructed based on calibration data of both signal and noise.

The basic procedure of deconvolution is:

- Do a Fast Fourier Transformation (FFT) of both the measured waveforms and the previously derived spe response (this should be stored for each PMT as calibration data).
- Apply the Wiener filter H(f) to the measured waveform in frequency domain, that's basically a multiplication operation in the frequency domain.
- Deconvolve the spe response S(f) from the filtered measured waveform, that's basically a division operation in frequency domain.
- Obtain the time of a spe hit by examining the phase shift, obtain the charge by examining the amplitude in the frequency domain.

Usually, time and charge information is obtained in time domain. Here we find it can be done in frequency domain. For example, in case of single p.e., the FFT can be written as:

$$z = \sum_j a_j * e^{\phi_j * i}, \tag{3}$$

where j is the j^{th} harmonic component, which ranges from 0 to N-1 (N represents the number of total sampled points). The relative time shift with reference to PMT spe response is reflected in the phase shift between two consecutive frequency samples $\Delta\phi_k(\phi_k - \phi_{k-1}$, k from 1 to N). Therefore, we can do a Gaussian fit to the distribution of $\Delta\phi_k$ and use the mean value to represent the hit time. Similarly, the mean value of a Gaussian fit to a_j distribution can be used to represent the charge. The method to

derive hit time and charge from the frequency domain in multiple p.e. case is still under development.

PERFORMANCE

Two examples from template-fitting method are shown in Figure 4. The black dots are 20-inch Hamamatsu PMT R12860 waveforms taken by the oscilloscope. The red curve is the template-fitting result. From the right plot of Figure 4, we can see that template-fitting works well even in complex p.e. cases. However, it will become intolerantly slow since the number of fitting parameters to be minimized is twice the number of total p.e.

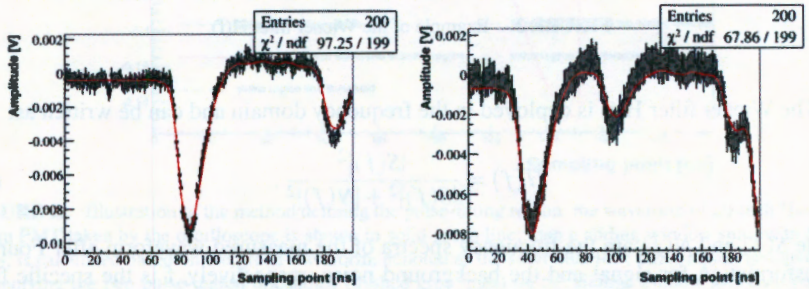

FIGURE 4. Two random examples of template-fitting results, R12860 waveforms are shown in black, template-fitting results are shown in red.

The deconvolution method is adopted as the default waveform reconstruction method due to the following reasons:

- It can handle the overshoot naturally. Overshoot is one of the sources of electronics nonlinearity, when using the charge integration method.
- It is very efficient, the time consumed in multiple p.e. cases and single p.e. cases is almost the same, $\sim$1 ms.
- It's robust & failure-free.
- The residual charge bias, close to 1%, is good.

The validation results of time and charge reconstruction performance from the deconvolution method is shown in Figure 5 and Figure 6. Figure 6 is the profile result of Figure 5. The charge in X axis of both figures means an increase in the amplitude relative to the spe amplitude, without any change in shape. We can achieve sub percent nonlinearity above 0.5 p.e.

CONCLUSIONS

In this paper, two methods of waveform reconstruction are described. Template-fitting is model-independent. The template can be built based on spe waveforms from calibration campaign. The performance of the template-fitting is checked using lab waveforms.

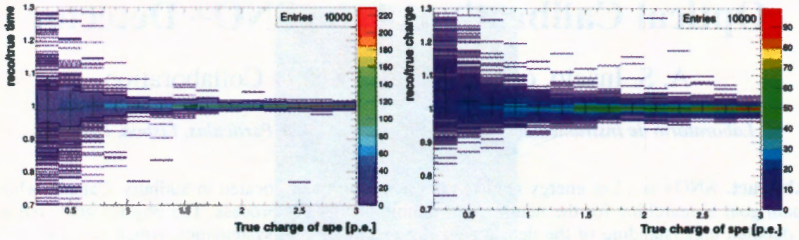

FIGURE 5. Demonstration of time and charge reconstruction performance from the deconvolution method.

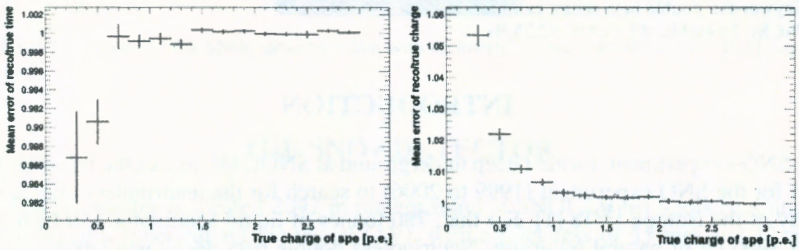

FIGURE 6. Average time and charge resolution from the deconvolution method.

It can deal with multiple pulse-region waveforms as well. The deconvolution method is robust and efficient, confirmed by testing on batch MC data. It takes ~1 ms per waveform, regardless of single p.e. or multiple p.e. It can also give good time and charge resolution. At present, the deconvolution method can achieve sub percent nonlinearity above 0.5 p.e. as shown in Figure 6. Other waveform reconstruction algorithms are also under development, for example, the neural network method.

ACKNOWLEDGMENTS

This work is supported in part by HGF and Deutsche Forschungsgemeinschaft DFG (Forschergruppe FOR 2319). It's also made possible by the 2016 Juelich-OCPC-Programme (China and Germany Postdoctoral Exchange Program).

REFERENCES

1. Adam, T., et al. *arXiv:1508.07166* (2015).
2. Yongbo Huang, et al. *arXiv:1707.03699* (2017).

Optical Calibration of the SNO+ Detector

A. S. Inácio, on behalf of the SNO+ Collaboration

Laboratório de Instrumentação e Física Experimental de Partículas, Lisboa, Portugal

Abstract. SNO+ is a low energy neutrino physics experiment located in Sudbury, Canada, whose main goal is searching for the neutrinoless double beta decay process. The physics goals require a detailed understanding of the detector energy resolution and systematics, which is achieved by a comprehensive calibration program. The Optical Calibration is performed using in-situ sources (fixed optical fibers and a deployable light diffusing sphere) that characterize and continuously monitor the optical properties of the detector, the main ones being the media attenuations and the response to light of the ~9400 photomultipliers.

Keywords: double beta decay, calibration
PACS: 29.40.Mc, 42.55.Mv, 42.25.Bs

INTRODUCTION

The SNO+ experiment, located deep underground at SNOLAB, reuses the infrastructure built for the SNO experiment (1999 to 2006) to search for the neutrinoless double beta decay of the isotope ^{130}Te [1]. For that, 780 tonnes of liquid scintillator will be loaded with 3900 kg of natural tellurium. Neutrinoless double beta decay is a lepton number violating process that, if observed, could prove the Majorana nature of neutrinos, i.e., that they are their own antiparticles, as well as allow the measurement of their effective mass. Other physics goals of the SNO+ experiment include the measurement of reactor, solar, supernova and geo-neutrinos.

The experiment is divided into three phases: Water phase, Liquid Scintillator phase and Te-loading phase. Physics data have been collected with the detector completely filled with water since May 2017. Liquid scintillator will be introduced in early 2018 and the tellurium will be loaded in early 2019. In all phases, detailed calibrations are required to understand the signals observed by the detector. That includes the Optical Calibration responsible for characterizing the effects modifying light propagation in the large volume of the detector and its collection by the ~9400 photomultipliers (PMTs). Such effects include the attenuation of light in each detector medium (water/scintillator/acrylic) and the angular dependence of the response of the PMTs. The Optical Calibration uses two in-situ sources: a system of fixed optical fibers and a deployable light diffusing sphere, called laserball (LB).

This paper starts with a description of the SNO+ detector, and then discusses the Optical Calibration hardware and analysis. Finally, it will present some of the first results obtained from the deployment of the laserball source.

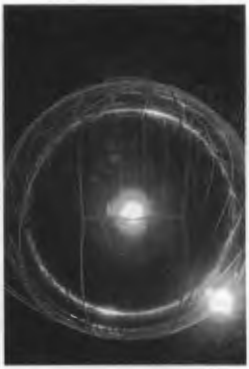

FIGURE 1. Picture of the SNO+ detector taken with an internal camera installed in the PMT support structure.

THE SNO+ DETECTOR

The SNO+ detector is located 2092 m underground at SNOLAB, in Sudbury, Canada. It consists of a spherical acrylic vessel (AV), with a thickness of 55 mm and 12 m in diameter, surrounded by a 17.8 m diameter geodesic steel structure that holds 9400 PMTs and other detector components, called the PMT Support Structure (PSUP) [1]. Almost all of the 9400 (20.3 cm in diameter) PMTs, with a coverage of ~50%, are the same as used in SNO, except for some that were damaged and had to be fixed or replaced. The PSUP is placed inside a barrel shape cavity 22 m wide and 34 m high. The volume between the AV and the PSUP, as well as the rest of the cavity, is filled with 7000 tonnes of ultra-pure water that provide a shield against the radioactivity from the instrumentation and surrounding rock. The detection medium inside the AV will change for the different data taking phases of the experiment: during the water phase the AV will be filled with 905 tonnes of ultra-pure water; during the pure scintillator phase it will be filled with 780 tonnes of LAB+PPO+bisMSB liquid scintillator, that will then be loaded with 0.5% Te-diol (1330 kg of ^{130}Te) for the Te-loading phase. The acrylic vessel is held in place by a net of support ropes and hold-down ropes. The hold-down ropes are an addition relative to SNO times, and their purpose is to cancel the buoyancy of the acrylic vessel when it is filled with the liquid scintillator (because the liquid scintillator has a smaller density than water, $\rho_{LAB} = 0.86$ g/cm^3). The acrylic vessel is connected to the deck level above the cavity through a cylindrical neck, from where deployable sources can be inserted to calibrate the detector. Other changes from SNO to SNO+ include upgraded electronics to accommodate the higher data rates, new calibration sources and a scintillator purification system. Figure 1 shows the interior of the PSUP, where it is possible to observe the PMTs, the AV and the system of ropes holding it in place.

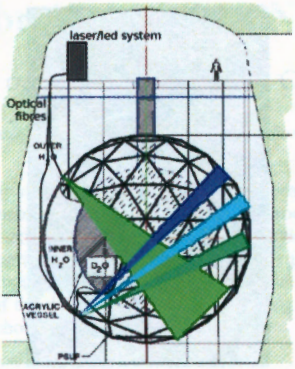

FIGURE 2. Cross sectional diagram of the SNO+ detector showing the ELLIE system.

OPTICAL CALIBRATION HARDWARE

The Optical Calibration is performed using an internally deployable source, called "laserball" [3], and a system of 120 optical fibers, called ELLIE (Embedded LED Light Injection Entity) [4], attached to the PSUP in fixed positions. These sources are used to characterize and continuously monitor the optical properties of the detector.

The fibers, illustrated in Figure 2, send pulses from fast LEDs or lasers into the detector, allowing frequent calibrations of the PMTs response, time and gain, as well as the measurement of the scattering lengths and the monitoring of the attenuation lengths of the media.

The laserball allows a full characterization of the detector response to light as it was designed to act as a point-like source of light with an isotropic emission throughout the detector volume. It consists of a quartz flask with 10.9 cm in diameter, filled with small air-filled glass beads suspended in silicone gel which are responsible for scattering the light that comes, through a fibre, from a nitrogen laser with dyes that is located in the deck above the AV. The laser emits pulsed light with a wavelength of 337 nm, and the dyes are used to change it to spectra centered on one of the following five wavelengths: 369 nm, 385 nm, 420 nm, 446 nm and 505 nm. This group of possible wavelengths allows to cover the whole PMT sensitivity region, as illustrated by Figure 3.

A laserball run is performed by collecting PMT data while the laserball is pulsing light at a fixed position, that can be central (in the center of the AV) or off-axis (away from the center of the AV). The optical calibration uses several laserball runs in $\sim$60 different positions inside and outside the AV for each of the six available wavelengths, as illustrated by Figure 4.

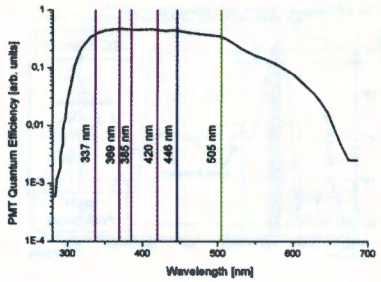

FIGURE 3. PMT Quantum efficiency as a function of wavelength. Each vertical line is one of the wavelengths of the light emitted by the laserball, and they cover the whole region of maximal PMT sensitivity.

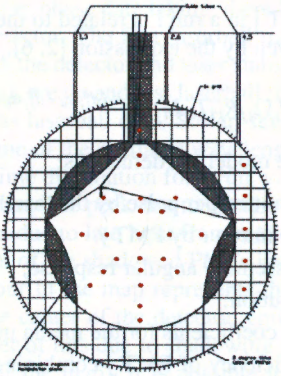

FIGURE 4. Cross sectional diagram of the SNO+ detector illustrating the laserball positions during a scan. Includes positions inside the AV along the vertical, horizontal and diagonal axis of the detector, and positions outside the AV.

OPTICAL CALIBRATION ANALYSIS

The Optical Calibration Analysis uses the laserball data to characterize the detector optical properties as a function of wavelength, position and direction. The main input for the analysis are the PMT occupancies, which are defined as the amount of direct light detected by each of the PMTs. The direct light is identified by imposing a narrow time window on the data to identify the prompt light in each PMT, as illustrated in Figure 5, thus ignoring signals due to pre- and late-pulsing of the PMTs or reflections from the detector elements.

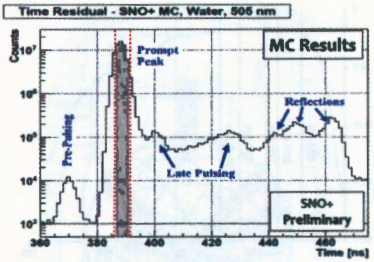

FIGURE 5. Time residual distribution of a MC simulation with the laserball in water, at the center of the AV, emitting light at 505 nm. Shown are the peaks due to direct light (prompt peak), pre- and late-pulsing, and reflections from the detector components. The two dashed red lines define the time window that is imposed on the data to identify the prompt light in each PMT.

The occupancy O_{ij} of a PMT j in a run i is related to the different optical parameters through the Optical Model, given by the expression [2, 6]:

$$O_{ij} = N_i \Omega_{ij} R_{ij} T_{ij} L_{ij} \varepsilon_j e^{-(d_{ij}^a \alpha_a + d_{ij}^b \alpha_b + d_{ij}^c \alpha_c)} \quad (1)$$

The different parameters of the model are defined as:

- N_i - number of photons emitted per pulse by the laserball in run i;
- Ω_{ij} - solid angle from LB in run i by PMT j.
- R_{ij} - PMT and reflector assembly angular response;
- L_{ij} - laserball light distribution;
- T_{ij} - Fresnel transmission coefficients for the media interfaces;
- ε_j - absolute quantum efficiency of PMT j combining the overall PMT efficiency and electronics threshold effects (including the quantum efficiency (QE), which refers to the wavelength dependent probability of registering a hit);
- $d_{ij}^{a,b,c}$ - light path lengths through the media;
- $\alpha_{a,b,c}$ - attenuation coefficients for the optical media;

The reason for including a parameter that describes the laserball light distribution in the model is because the laserball itself is not totally isotropic. Not accounting for it would result in a wrong characterization of the other parameters of the model.

The analysis does not use PMTs that are shadowed by some of the detector elements, such as the ropes that hold the acrylic vessel in place, because the shadowing imposes a stronger dependency on the source position. It calculates numerically, by knowing the source and PMT positions, the solid angle, the Fresnel transmission coefficients and the distances travelled by the light in the different media. The remaining optical parameters are obtained by performing a multi-parameter fit that compares the measured occupancy with the one predicted by the model.

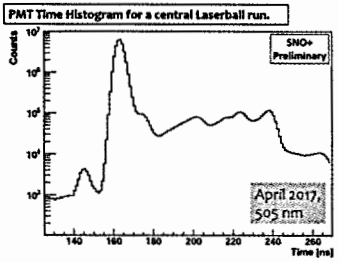

FIGURE 6. PMT time histogram for a central laserball run at 505 nm.

LASERBALL DEPLOYMENT AND FIRST RESULTS

Since the beginning of the water phase data taking, there have been several deployments of the laserball inside the detector. The first laserball data has been very important to perform several checks: check the detector and laser stability, tune the laser and laserball settings (such as the intensity), create and test laserball data quality tools as well as test the software tools that process laserball data. So far, several runs in different positions along the vertical axis for some of the available wavelengths were already obtained.

Figure 6 shows the PMT time distribution for a run with the laserball at the center of the AV, emitting light at 505 nm. The peak due to the direct light is clearly visible, and it is followed by smaller bumps due to late light from reflections. Looking at PMT maps, like Figure 7, gives an insight of the shadowed PMTs inside the detector due to several detector elements. Each colour in the map represents the number of hits detected, for a run with the laserball in the center of the detector, emitting at 337 nm. The PMTs at the top have a smaller number of hits due to shadowing by the hold-down ropes. Also, around the equator (center of the map), it is possible to identify a circular pattern of PMTs with lower hits. This is due to the belly plates, a region in the equator of the AV where the ropes attach.

Figure 8 shows distributions of occupancies for a central laserball run at 420 nm. The distribution in black corresponds to all the online PMTs during the run, and the distribution in red corresponds to the online and non-shadowed PMTs. As can be observed, excluding the shadowed PMTs affects mostly the low occupancy tail of the distribution.

The laserball data obtained so far is not enough to characterize with a good precision the optical effects in the detector. While data was acquired, the Optical Calibration analysis tools were tested and validated with data from the SNO experiment and simulated data. Through the tests with simulated data, the analysis tools showed a good capability in reproducing the optical parameters used as input for the simulations, as shown by Figure 9.

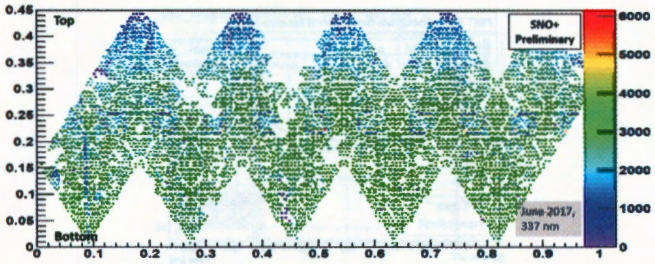

FIGURE 7. Icosahedron projection of the SNO+ detector. Shows the number of hits in each PMT, for a run at 337 nm with the laserball in the center of the detector. The PMTs with a lower number of hits are shadowed due to detector elements. Blank spaces are due to offline PMTs.

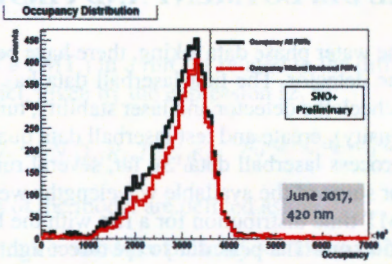

FIGURE 8. Occupancy distribution for a central laserball run, at 420 nm, before (black) and after (red) excluding the shadowed PMTs.

CONCLUSIONS

The detection of light signals in the SNO+ experiment is strongly affected by the optical effects that change the propagation and collection of light in the detector, such as the

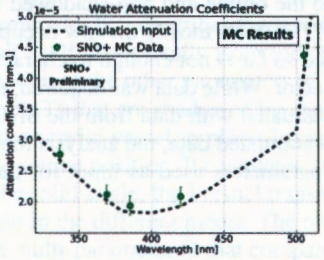

FIGURE 9. Water attenuation coefficients extracted by the Optical Calibration Analysis from simulated data (green dots), compared with the simulation input (black dashed line). The coefficients obtained show a good agreement with the input.

media attenuation and the PMT angular responses. The achievement of the experiment physics goals requires very precise energy reconstruction methods that depend on a detailed characterization of the detector response to light. To characterize it, a detailed optical calibration has to be performed, using the available light sources, such as the laserball and the fixed optical fibres. The laserball has been deployed inside the SNO+ detector several times since May 2017, and the first data was crucial to check the status of the detector and of the calibration hardware. Data has been collected along the vertical axis for several wavelengths. In the meantime, the Optical Calibration analysis tools have been tested and validated with Monte Carlo data, and are ready to extract the optical parameters once the full set of laserball data is ready (expected at the beginning of 2018).

ACKNOWLEDGMENTS

This work is supported by ASRIP, CIFAR, CFI, DF, DOE, ERC, FCT, FedNor, NSERC, NSF, Ontario MRI, Queens University, STFC, UC Berkeley and benefitted from services provided by EGI, GridPP and Compute Canada. The presenter is supported by FCT (Fundação para a Ciência e a Tecnologia, Portugal) grant number PTDC/FIS-NUC/0640/2014. We thank SNOLAB and Vale for valuable support.

REFERENCES

1. S. Andringa *et al.* (SNO+ Collaboration), Adv.High Energy Phys. **2016**, 6194250, (2016).
2. B.A. Moffat, *The Optical Calibration of the Sudbury Neutrino Observatory*. PhD Thesis, Queen's University, (2001).
3. B.A. Moffat *et al.*, Nucl.Instrum.Meth. **A 554**, 255-265, (2005).
4. R. Alves *et al.*, Journal of Instrumentation (JINST) **10**, P03002, (2015).
5. O. Simard, *Measurement of the Survival Probability and Determination of the Three-Flavour Neutrino Oscillation Parameters at the Sudbury Neutrino Observatory*. PhD thesis, Ottawa-Carleton Institute for Physics, Carleton University, Ottawa, Ontario, Canada, (2009).
6. R. Stainforth, *Characterising the Optical Response of the SNO+ Detector*. PhD Thesis, Department of High Energy Particle Physics of the Faculty of Sciences and Engineering of the University of Liverpool, (2016).

The reactor antineutrino signal maps of Slovakia and the Czech Republic

Peter Kerényi, Dušan Štefánik

Department of Nuclear Physics and Biophysics, Comenius University, Mlynská dolina, SK-84248 Bratislava, Slovakia

Abstract. Nuclear reactors are intense sources of electron antineutrinos. Recently many experiments concentrating on the measurements of the basic properties of reactor antineutrinos were built or are under construction. Therefore, theoretical calculation of the reactor antineutrino signal and its energy spectrum are subjects of great importance. The signal depends on the reactor-detector distance, reactor type, reactor power, and load factor. This paper summarizes the theoretical background of the signal calculation. The detailed reactor antineutrino signal maps of Slovakia and the Czech Republic are presented. The antineutrino signal coming from different sources is visualized.

Keywords: nuclear reactors, antineutrino, antineutrino detectors, antineutrino signal map
PACS: 14.60.Pq, 28.41.-i, 29.85.-c

INTRODUCTION: PROPERTIES OF THE REACTOR ANTINEUTRINO SIGNAL

Nuclear reactors are the strongest antineutrino sources created by humanity. In a reactor approximately 200 MeV of energy and six antineutrinos are produced per fission. Antineutrinos are emitted due to the β^- instability of the neutron-rich fission fragments, resulting a flux of around $6 \cdot 10^{20}\ \bar{\nu}_e/s$ emitted from a 3 GW reactor [1]. Calculation of the reactor antineutrino signal at a given location requires many ingredients. It demands knowledge about the production of antineutrinos at reactor cores, their propagation to the detector, and their detection via inverse β decay.

Production of antineutrinos at reactor cores

Approximately 99.9% of the power of nuclear reactors comes from the thermal-neutron-induced fission of uranium and plutonium isotopes ^{235}U, ^{238}U, ^{239}Pu, ^{241}Pu and from the decays of their fission fragments. These fragments are very neutron-rich compared to the line of stability of nuclei making them β^- active. In β^- decay a neutron is converted into a proton, electron and an electron antineutrino. The total emitted antineutrino spectrum of a nuclear reactor is given as [2]

$$S(E_{\bar{\nu}}) = P_{th}\, LF \sum_{k=1}^{4} \frac{p_k}{Q_k} \lambda_k(E_{\bar{\nu}}), \tag{1}$$

where P_{th} is the total reactor thermal power, LF is the load factor, p_k is power fraction of the k-th actinide in the reactor fuel , Q_k is the energy released per fission of the k-th actinide in the reactor fuel , $\lambda_k(E_{\bar{\nu}})$ is the antineutrino spectrum of the k-th actinide in the reactor fuel. Power fractions p_k and energies released from the fission Q_k of reactor fuel isotopes are shown in Table 1. Data of the reactor thermal power P_{th} and monthly average load factor LF for all commercial nuclear reactors in the world can be obtained from the Istituto Nazionale di Fisica Nucleare (INFN) database [3].

Different nuclear reactor cores use reactor fuels of different composition. Natural uranium contains next to the isotope ^{238}U roughly 0.72% of isotope ^{235}U. While it is usable in some reactors (PHWR), in others (PWR, BWR, LWGR, GCR) natural uranium needs to be enriched to contain a larger percentage of ^{235}U in order to produce a self-sustaining chain reaction. Thus, the power fractions of the actinides p_k differ for each reactor type because of the different starting fuel composition. During the power cycle of a nuclear reactor the composition of the fuel changes, as plutonium isotopes are bred and ^{235}U is consumed, thus the power fractions evolve with time. With the evolution of fuel composition, the antineutrino signal as a function of burnup changes as well. Approximately a 10% decrease of antineutrino count rate can be observed during a fuel cycle of about 550 days [1].

TABLE 1. Energy released per fission Q_k for isotopes of uranium and plutonium in reactor fuels according to *Ma et al.* [4] and their power fractions p_k for different reactor types and reactors using MOX according to *Baldoncini et al.* [2]

Fissile isotope k	$Q_k(MeV)$	p_k for PWR, BWR, LWGR, GCR	p_k for PHWR	p_k for MOX
^{235}U	202.36±0.26	0.560	0.543	0.000
^{238}U	205.99±0.52	0.080	0.024	0.081
^{239}Pu	211.12±0.34	0.300	0.411	0.708
^{241}Pu	214.26±0.33	0.060	0.022	0.212

Regarding reactors using MOX (mixed oxide fuel), approximately 30% of their power output comes from MOX fuel itself, while the remaining 70% of power is produced by standard fuel, with power fractions depending on the reactor type.

The antineutrino emission spectrum of the k-th actinide $\lambda_k(E_{\bar{\nu}})$ can be determined in two complementary ways: the analytical 'ab initio' summation and the experimental beta electron spectrum conversion methods. In our calculations we adopted the analytical 'ab initio' approach for evaluating the antineutrino spectra of each four contributing isotope from *Mueller et al.* [5].

Propagation of antineutrinos

There are three generations of active antineutrinos, associated with each lepton, specifically the electron antineutrino $\bar{\nu}_e$, muon antineutrino $\bar{\nu}_\mu$, and tau antineutrino $\bar{\nu}_\tau$. Arguably, the most important discovery in neutrino physics is the discovery of the oscillation between these interacting flavors. One of the most significant consequences of neutrino oscillation is the small, unequal rest mass of the neutrinos. The Nobel Prize in Physics 2015 was awarded for the experimental discovery of neutrino oscillation.

The concept behind neutrino oscillation is that there are antineutrinos of definite lepton flavor ($\bar{\nu}_e, \bar{\nu}_\mu, \bar{\nu}_\tau$) and antineutrinos of definite mass ($\bar{\nu}_1, \bar{\nu}_2, \bar{\nu}_3$). Each antineutrino flavor eigenstate is a different superposition of antineutrino mass eigenstates. The lepton and mass eigenstates mix via the three mixing angles ($\theta_{12}, \theta_{13}, \theta_{23}$) according to the Pontecorvo-Maki-Nakagawa-Sakata (PMNS) matrix.

When calculating the antineutrino flux in a certain distance from the reactor core, one has to take into account that antineutrinos from nuclear reactors are emitted in every direction and propagate in a straight line. The further the detector is located from the source, the smaller percentage of the emitted antineutrinos reach it. The reactor-detector distance d is the shortest distance between the two points through the planet, not the distance "as the crow flies", as antineutrinos propagate through matter. The relation between initial reactor antineutrino flux and the flux in the distance d can be expressed as

$$\Omega_d = \frac{\Omega_{init}}{4\pi d^2}. \tag{2}$$

The survival probability of a given flavor is governed by the mass-mixing oscillation parameters ($\delta m^2, \theta_{12}, \theta_{13}$), which we have taken from *Capozzi et al.* [6] and are shown in Table 2. For the purpose of calculating the reactor antineutrino signal, the survival probability for electron antineutrinos can be expressed as [7]

$$P_{ee} = \cos^4(\theta_{13})\left(1 - \sin^2(2\theta_{12})\sin^2\left(\frac{\delta m^2 d}{4E_{\bar{\nu}}}\right)\right) + \sin^4(\theta_{13}). \tag{3}$$

TABLE 2. Values for oscillation parameters from *Capozzi et al.* [6]

Oscillation parameter	Central value	1σ range
δm^2 [eV^2]	$7.54 \cdot 10^{-5}$	$2.6 \cdot 10^{-6}$
$\sin^2(2\theta_{12})$	$3.08 \cdot 10^{-1}$	$1.7 \cdot 10^{-3}$
$\sin^2(2\theta_{12})$	$2.34 \cdot 10^{-2}$	$2.0 \cdot 10^{-3}$

Detection of antineutrinos

Antineutrino detection is based on inverse β decay (IBD) on free protons $\bar{\nu}_e + p \rightarrow e^+ + n$ due to the relatively large reaction cross section of the order 10^{-42}cm^2. The IBD cross section can be parametrized according to [8] as

$$\sigma_{IBD}(E_{\bar{\nu}}) = 10^{-43} p_e \, E_e \, E_{\bar{\nu}}^{-0.07056+0.02018\ln(E_{\bar{\nu}})-0.001953\ln^3(E_{\bar{\nu}})} \left[\text{cm}^2\right], \tag{4}$$

where $E_e = E_{\bar{\nu}} - \Delta$ is the positron energy and $p_e = (E_e^2 - m_e^2)^{1/2}$ is the positron momentum. The mass of electrons, respectively positrons is $m_e = 0.511$ MeV, Δ stands for the mass difference of neutrons and protons, $\Delta = m_n - m_p \approx 1.293$ MeV. All energies in the Eq. (4) are expressed in MeV.

Inverse β decay causes two light flashes in the detector. The first, prompt flash, is caused by the immediate annihilation of the positron with a nearby electron producing

two 511 keV γ-rays. The second, delayed flash, is caused by the capture of the neutron on an element or a free proton. Capture on a free proton is more typical, producing a γ-ray of 2.22 MeV.

CALCULATION OF THE REACTOR ANTINEUTRINO SIGNAL

Collecting equations (1), (2), (3), and (4) we can express the relation for the total antineutrino signal form nuclear reactors at a given detector location using the following formula [2]

$$N_{tot} = \varepsilon N_p \tau \sum_{i=1}^{N_{reactor}} \frac{P_{th}^i}{4\pi d_i^2} \langle LF_i \rangle \int dE_{\bar{\nu}} \sum_{k=1}^{4} \frac{p_k}{Q_k} \lambda_k(E_{\bar{\nu}}) P_{ee}(E_{\bar{\nu}}, d_i) \sigma_{IBD}(E_{\bar{\nu}}), \qquad (5)$$

where ε is the detector efficiency, N_p is the number of free target protons in the detector, τ is the exposure time, $\langle LF_i \rangle$ is the average load factor of the i-th reactor over τ, d_i is the distance of the i-th reactor from the detector, $N_{reactor}$ is the number of all nuclear reactors on Earth.

Setting the detector efficiency $\varepsilon = 1$, the number of free target protons $N_p = 10^{32}$ (which approximately equals to the number of free protons in a 1 kton liquid scintillation detector) and the exposure time τ to a year ($\tau = 3.15 \cdot 10^7$ s), the calculated reactor antineutrino signal is in terrestrial neutrino units (TNU).

Since the detection is based on inverse β decay, only those antineutrinos are detected, which have higher energies than the IBD threshold, approximately 1.806 MeV [1]. Thus, for numerical evaluation, the integral boundaries can be set from the IBD threshold to 10 MeV, as reactor antineutrinos of higher energies are of negligible amount.

Reactor antineutrino signal maps

We have created the reactor antineutrino signal maps of Slovakia and the Czech Republic by placing ten thousand virtual 1 kton detectors (100x100 rectangular grid) separately over the area of Slovakia and the Czech Republic and calculating the total worldwide antineutrino signal in each point according to Eq. (5) using a computation software. Converting the raw calculated data of ten thousand triplets of latitude, longitude and signal for each country into a contour plot resulted our maps. The calculated signal is for the year 2015. In 2015 there were 448 registered commercial nuclear reactors in the world. We have taken the location, type, thermal power, and monthly load factors of each nuclear reactor from the INFN database [3].

In order to optimize our taxing calculations, we have decided to calculate the reactor antineutrino signal from reactors very far from Slovakia and the Czech Republic on a smaller 6x6 grid. This calculation included 266 nuclear reactors from Argentina, Armenia, Brazil, Canada, China, Taiwan, India, Iran, Japan, Pakistan, South Korea, Mexico, South Africa, the United States of America, and the Russian Bilibino Nuclear Power Plant. The mean signal for Slovakia was 2.321 TNU, for the Czech Republic 2.305 TNU. Given the scope of later results and possible uncertainties, these mean values

can be used as constant throughout the corresponding countries without sacrificing accuracy, meanwhile greatly reducing the time needed for calculations.

In the case of reactors located closer to our studied countries, we separately calculated the reactor antineutrino signal from reactors in the studied countries, their neighbouring countries, and the remaining countries in Europe. In Europe there are commercial nuclear reactors located in Belgium, Bulgaria, Czech Republic, Finland, France, Germany, Hungary, Netherlands, Romania, Russia, Serbia, Slovakia, Spain, Sweden, Switzerland, Ukraine, and the United Kingdom. Combination of output data allowed the creation of custom maps with selected sources.

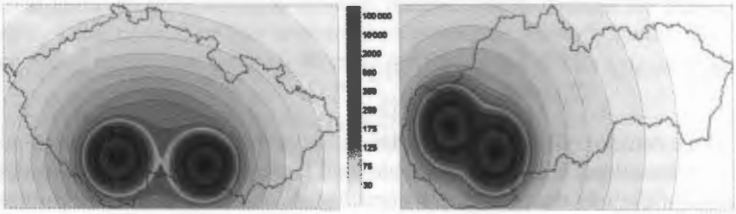

FIGURE 1. Reactor antineutrino signal maps of Slovakia and the Czech Republic, with reactor antineutrino signal coming only from reactors located in the corresponding countries. Signal is expressed in TNU.

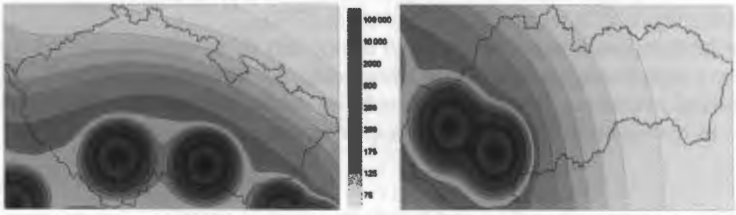

FIGURE 2. Reactor antineutrino signal maps of Slovakia and the Czech Republic, with reactor antineutrino signal coming from reactors in the corresponding countries and their neighbouring countries. The neighbouring countries of the Czech Republic with commercial nuclear reactors are Germany and Slovakia. The neighbouring countries of Slovakia with commercial nuclear reactors are the Czech Republic, Hungary, and Ukraine. Signal is expressed in TNU.

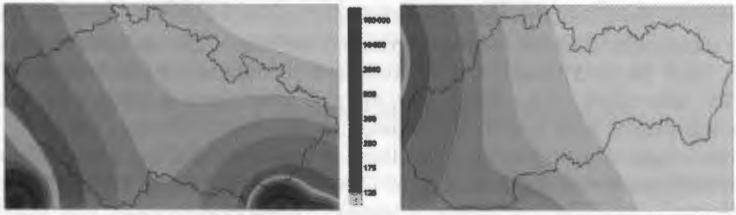

FIGURE 3. Reactor antineutrino signal maps of Slovakia and the Czech Republic, with reactor antineutrino signal coming from all commercial reactors in the world except for the reactors located in the corresponding countries. Signal is expressed in TNU.

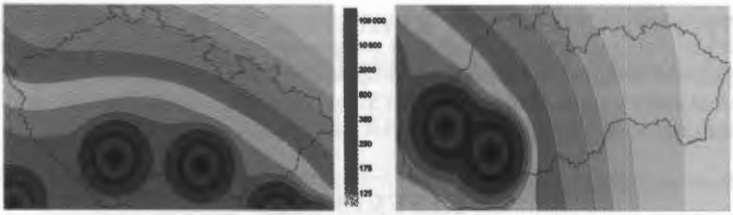

FIGURE 4. Reactor antineutrino signal maps of Slovakia and the Czech Republic, with reactor antineutrino signal coming from all commercial reactors in the world. Signal is expressed in TNU.

Figure 1 demonstrates how quickly the reactor antineutrino signal reduces with increasing reactor-detector distance. In the case of Slovakia both Jaslovské Bohunice and Mochovce Nuclear Power Plants are located in the western part of the country. In the eastern part of Slovakia their contribution to the reactor antineutrino signal is below 20 TNU. In the case of the Czech Republic the Dukovany and Temelin Nuclear Power Plants are located in the southern part of the country, therefore the antineutrino signal originating from them is weaker in the northern parts of the country. This effect is primarily due to Eq. (2), the initially strong antineutrino flux decreases with the square of the reactor-detector distance.

From Figure 2 we can learn, that while the neighbouring countries do significantly contribute into the reactor antineutrino signal, the locations of the nuclear power plants in the studied countries can be still clearly distinguished. The same can be said about Figure 4 representing the worldwide reactor antineutrino signal.

Comparing Figures 1 and 3 we can state, that in the case of Slovakia, antineutrino signal coming from reactors in Slovakia dominates in the west, while the worldwide signal dominates in the eastern regions of the country. In the case of the Czech Republic, Czech signal dominates in the middle and southern parts of the country, while the worldwide signal is stronger everywhere else. This is due to the closeness of German and Slovak reactors to the Czech border.

If we had to choose the location of a future geo-neutrino experiment in Slovakia or the Czech Republic, these maps would help us determine the best possible location. Since the energy spectrum of antineutrinos from nuclear reactors overlaps with the energy spectrum of geo-neutrinos, reactor antineutrinos constitute a severe source of background for the detection of geo-neutrinos [2]. According to Figure 4, the smallest worldwide reactor antineutrino signal is expected in the easternmost parts of Slovakia, therefore that would the best place for a potential geo-neutrino experiment in these two countries.

CONCLUSIONS

In this paper we described a method of calculation antineutrino signal from arbitrary nuclear reactors at arbitrary detector sites, real or virtual. We calculated and visualized the reactor antineutrino signal over Slovakia and the Czech Republic coming from all

commercial nuclear power reactors in the world for the year 2015. We compared the antineutrino signal arising from different sources and presented results in the series of the maps. According to our results, we proposed that the most suitable location for an experiment studying geo-neutrinos within Slovakia and the Czech Republic would be in the eastern regions of Slovakia.

REFERENCES

1. A.C. Hayes and P. Vogel, *Ann. Rev. Nucl. Part. Sc.* Vol. **66**, 219 (2016).
2. M. Baldoncini, I. Callegari, G. Fiorentini, F. Mantovani, B. Ricci, V. Strati, and G. Xhixha, *Phys. Rev. D* **91**, 065002 (2015).
3. `http://www.fe.infn.it/antineutrino/`
4. X.B. Ma, W.L. Zhong, L.Z. Wang, Y.X. Chen, and J. Cao, *Phys. Rev. C* **88**, 014605 (2013).
5. T.A. Mueller, D. Lhuillier, M. Fallot, A. Letourneau, S. Cormon, M. Fechner, L. Giot, T. Lasserre, J. Martino, G. Mention, A. Porta, and F. Yermia, *Phys. Rev C* **83**, 054615 (2011).
6. F. Capozzi, G.L. Fogli, E. Lisi, A. Morrone, D. Montanino, and A. Palazzo, *Phys. Rev. D* **89**, 093018 (2014).
7. G. Fiorentini, G.L. Fogli, E. Lisi, F. Mantovani, and A.M. Rotunno, *Phys. Rev. D* **86**, 033004 (2012).
8. A. Strumia and F. Vissani, *Phys. Letters B* **564**, 42 (2003).

Single Pion Production in Neutrino-Nucleon Scattering Studied with FORM Package

Beata E. Kowal and Krzysztof M. Graczyk

Institute of Theoretical Physics, University of Wrocław, pl. M. Borna 9, 50-204, Wrocław, Poland

Abstract. Two models for the single pion production induced by interactions of the neutrinos with the nucleons are studied. The nonresonant background contribution is a subject of analysis. It is shown that the normal component of the polarization of the charged lepton is sensitive on the nonresonant background contribution. It is also demonstrated that the FORM language can be utilized to evaluate all necessary transition matrix elements and the single pion production cross sections.

Keywords: single pion production, neutrino-nucleon interaction, lepton polarizations, nucleon polarizations, non-resonant background, FORM
PACS: 13.15.+g, 13.60.Le

MOTIVATION

Let us consider the single pion production (SPP) in the neutrino-nucleon scattering. It is the processes of a type

$$\nu_\mu(k) + N(p) \to \mu^-(k') + N'(p') + \pi(k_\pi), \tag{1}$$

where N and N' are initial and final nucleons, while k, k', p, p' and k_π denote the neutrino, outgoing lepton, initial nucleon, outgoing nucleon and pion momenta respectively.

A good understanding of the the SPP processes is important for such fundamental studies as the problem of the neutrino oscillations and the CP-violation in lepton sector [1]. These fundamental properties of neutrinos are studied experimentally in the long and short baseline experiments like T2K [2]. The measurement of the oscillation parameters and CP-violation phase is based on the detection of the quasielastic neutrino-nucleus (QE) scattering but the SPP-like events contribute to the background for theses measurements.

There are two theoretical scenarios for the pion-production mechanism in process (1): i) a resonant, where the nucleon is exited to resonant state and decays to the pion-nucleon πN system; ii) a nonresonant, where the resonance states do not occur but pions occur. The main theoretical difficulty is to describe the latter dynamics properly. There are many theoretical models describing the SPP (see Refs. in [3]), however, typically they are different in the treatment of the resonance and the nonresonance contributions. All models are fine tuned to reproduce the bubble chamber data [4, 5]. However, the data are not enough accurate and statistically consistent [6, 7] to constrain the parameters of the models well. Hence the predictions of the SPP cross sections are quite model dependent. Therefore there is a need of performing more deeper experimental and theoretical studies of the physics, which is behind the process (1).

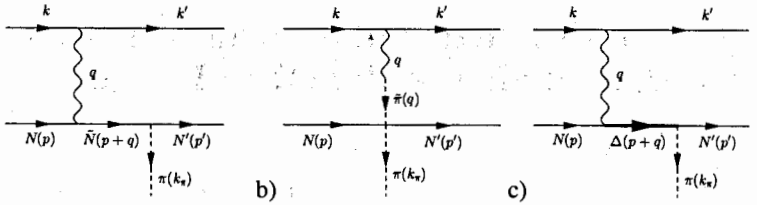

FIGURE 1. The SPP diagrams: (a) nucleon pole, (b) pion pole and (c) delta pole.

Our goal is to propose the physical observables which contain the signal which may help to constrain the theoretical models for the nonresonant background contribution. In this short report we shortly review some of the results presented in our prior work [3], where we show that the significant information about the nonresonant background contribution is hidden in the components of the polarization vector and a degree of polarization of the final nucleon and the charged lepton.

SPP MODELS

The differential cross-section for the process (1) reads

$$d\sigma = \frac{1}{4ME_k}\frac{d^3\mathbf{k'}}{2E_{k'}(2\pi)^3}\frac{d^3\mathbf{p'}}{2E_{p'}(2\pi)^3}\frac{d^3\mathbf{k}_\pi}{2E_{k_\pi}(2\pi)^3}(2\pi)^4\delta^{(4)}(p'+k'+k_\pi-k-p)|\mathscr{M}|^2 \quad (2)$$

where $k = (E_k, \mathbf{k})$ etc., and M denote the averaged nucleon mass. Notice that the spin notation is systematically omitted here, $\mathscr{M}$ – is the transition matrix element.

In the one-boson exchange approximation the scattering matrix is given by a contraction of a leptonic and a hadronic currents:

$$\mathscr{M} = -\frac{G_F}{\sqrt{2}}\cos\theta_C\bar{u}(k')\gamma_\mu(1-\gamma_5)u(k)J^\mu, \quad (3)$$

where G_F is the Fermi constant, while θ_C is the Cabibbo angle. The total hadronic current J^μ is a sum of contribution described by various Feynman diagrams.

$$J^\mu = \sum_{a\in S} C_a J_a^\mu, \quad (4)$$

where C_a is the Clebsch-Gordan coefficient. Then the square of the $\mathscr{M}$ matrix reads

$$|\mathscr{M}|^2 = \sum_{a,b\in S} \mathscr{M}_a\mathscr{M}_b^*. \quad (5)$$

We concentrate our attention on the SPP processes in which the neutrino energy is of the order of 1 GeV. In this describing the resonance part by the nucleon to the $\Delta(1232)$ resonance state transition is a good approximation.

In this paper we report the results obtained within two models: Hernàndez-Nieves-Valverde (HNV) [8] and Fogli-Nardulli (FN) [9]. In the first approach the resonance contribution is described by two diagrams, while nonresonant part includes five diagrams. The FN model includes one resonance diagram and three nonresonance diagrams. In both models the $\Delta(1232)$ state is described by the Rarita-Schwinger 3/2-spin field but with different choice of the phenomenological form factors. In both models the background terms are obtained assuming the chiral symmetry of strong interactions. However, there are some differences between models which are described in Ref. [3]. An example of three Feynman diagrams (one resonance and two nonresonance) contributing to the SPP cross section is given in Fig. 1.

There are some similarities between the HNV and FN models, however, the predictions of both approaches are different. It is illustrated in Fig. 2, where we present plots of the double differential cross sections and its partition to various interference $\mathscr{M}_a\mathscr{M}_b^*$ terms. Notice significant differences between predictions of two models given by nucleon pole (NP) and pion in flight (PF) diagrams.

FORM AND SPP AMPLITUDES

FORM is a system for symbolic manipulation [10]. It has been developed by Jos Vermaseren in Nikhef - the Dutch institute for subatomic physics. The FORM reads script files containing definitions of the mathematical expressions and the instructions. This language was design to use in the quantum field theory. It is vary fast and excellent tool for performing complicated algebraic manipulation, in particular in non-commutative algebra. It contains a number of functions which allows to optimized the output in order to use in numerical calculations done in the Fortran, C++ codes etc. More information about the package can be find in [11].

The FORM includes the definition of the Clifford algebra with Dirac-gamma matrices as well as the trace function. We use these functionalities to calculate the transition matrix amplitudes and their interferences.

We have implemented currents from both models in the FORM language. Below we present an example of the implementation of two HNV currents which have the form:

$$
\begin{aligned}
J^{\mu}_{NP} &\sim \bar{u}(p')\not{k}_{\pi}\gamma_5 \frac{\not{p}+\not{q}+M}{(p+q)^2-M^2+i\varepsilon}\left(V^{\mu}_N(q)-A^{\mu}_N(q)\right)u(p) \\
J^{\mu}_{PP} &\sim F_{\rho}\frac{q^{\mu}}{q^2-m_{\pi}^2}2M\bar{u}(p')\not{q}u(p). \qquad (6)
\end{aligned}
$$

(for explanation of the notation see [3]). The implementation of theses currents in the FORM language reads

```
Global   Ja = Jnp(mu);
Global   Jb = Jpp(mu);

id Jnp(mu?)= -g_(2,kpi)*g5_(2)*(g_(2,p) + g_(2,q) + M)*
( 2*( F1*g_(2,mu) - (g_(2,mu)*g_(2,q)
-g_(2,q)*g_(2,mu))/2*(F2/2/M) ) -
```

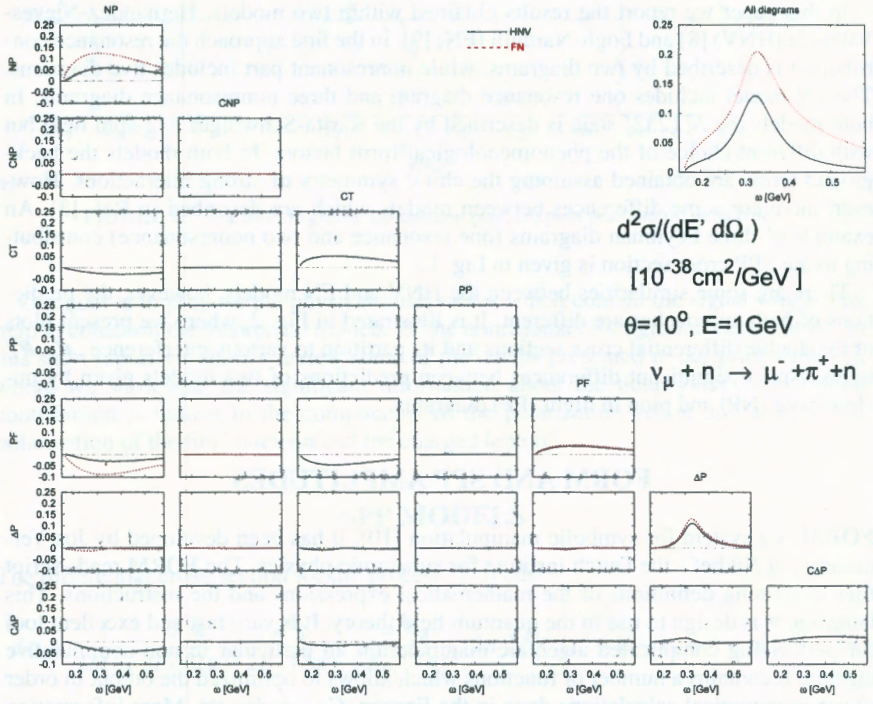

FIGURE 2. Double differential cross section and its partition into interference contributions $\mathcal{M}_a\mathcal{M}_b^*$, where in the HNV model (solid black line) a = NP, CNP, CT, PP, PF, ΔP and $C\Delta P$, while in the FN (dashed red line) model a = NP, CNP, PF and ΔP. Notation of diagrams is given in [3]. Notice that θ is the scattering angle, while ω is the energy transfer, while E' denotes the energy of the outgoing muon. The contributions on diagonal are given by $|\mathcal{M}_a|^2$, below diagonal contributions from $2\Re\mathcal{M}_a\mathcal{M}_b^*$ are given.

```
( Ga*g_(2,mu) + Gp*q(mu)*g_(2,q) )*g5_(2) )*[1/(W2-M^2)];

id Jpp(mu?)= -Frho*g_(2,q)*q(mu)*[1/(q^2-mpi2)];
```

Computed currents can be stored in .sav file and then used in further calculations in another FORM script. In the next part of calculation we obtained a contraction of hadronic and leptonic tensor. The next code is a part of script in FORM which computes a leptonic tensor, namely

```
Global TensorL = 1/8*(g_(1,kp) + m)*g_(1,mu)*
(1 - E*g5_(1))*g_(1,k)*g_(1,nu)*(1 - E*g5_(1));
trace4, 1;
```

Instructions like the physical identities that allow reducing the number of variables or substitution were written in form of a procedure in separated file and were called if

necessary. Example of a part of such procedure is given below:

```
#procedure Kinematics()
id pp = p + q - kpi;
id kp = k - q;
id p.kpi = (mpi2 + W2  - M^2)/2  - KpiQ;
id p.q = (W2  - M^2 - t)/2;
id p.k = (s - M^2)/2;
id k.q = (t - m^2)/2;
id kpi.kpi = mpi2;
id q.q = t;
id p.p = M^2;
id k.k = 0;
 #endprocedure
```

Obtained amplitudes were optimized (we used Format O3) and printed in C form. A simple bash script took output of FORM and changed it into a file with C++ function, which returned one amplitude. Files with amplitudes were included to C++ project, which was developed to generate all kinds of differential cross-sections.

POLARIZATION TRANSFER OBSERVABLES

We utilized the FORM package to calculate all necessary transition amplitudes in order to calculate the spin averaged cross sections and also polarization transfer observables. We obtained that the polarization transfer observables contain valuable information about the nonresonance contribution [3]. In particular let us underline that the normal component of the polarization of the outgoing charged lepton is determined by the interference between resonance and nonresonance contributions. It is illustrated in Fig. 3. Hence the measurement of the polarizations of the final fermions in process (1) should give an access to the non-trivial knowledge about resonance and nonresonance dynamics. In particular it should allow to fix the relative sign between both contributions.

ACKNOWLEDGMENTS

We used FORM symbolic language [10] to perform symbolic calculations. The calculations have been carried out in Wroclaw Centre for Networking and Supercomputing (`http://www.wcss.wroc.pl`), grant No. 268.

REFERENCES

1. U. Mosel, *Ann. Rev. Nucl. Part. Sc.* **66**, 171–195 (2016).
2. K. Abe, et al., *Nucl. Instrum. Meth. A* **659**, 106–135 (2011).
3. K. M. Graczyk, and B. E. Kowal (2017).
4. G. M. Radecky, V. E. Barnes, D. D. Carmony, A. F. Garfinkel, M. Derrick, E. Fernandez, L. Hyman, and G. Levman *et al.*, *Phys. Rev. D* **26**, 3297 (1982), [Erratum-ibid. D **26** (1982) 3297].

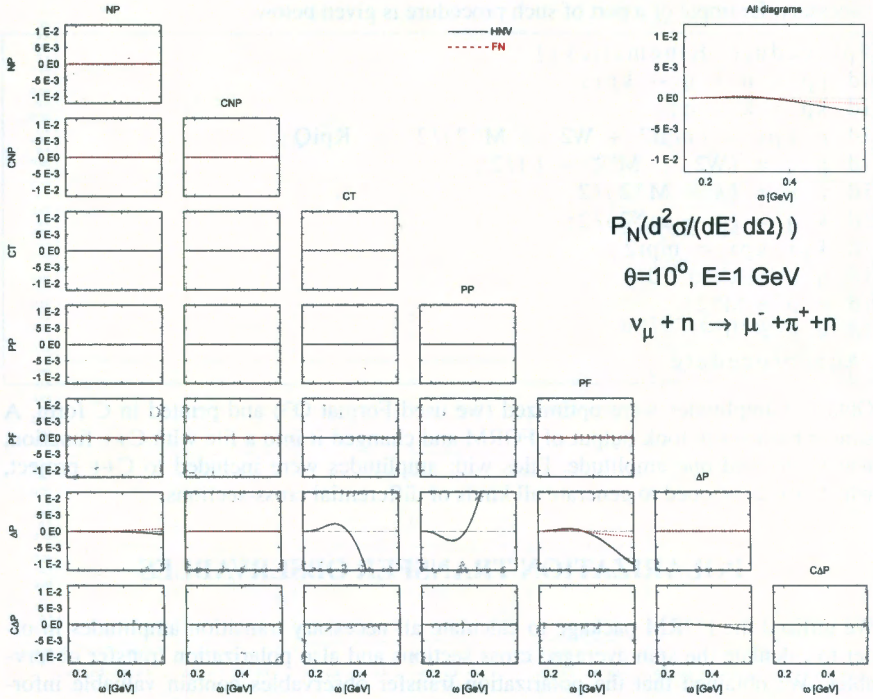

FIGURE 3. Normal component, P_N, of the μ^- lepton polarization depending on the energy transfer ω and the scattering angle θ as well the partition of P_N into various interference contributions $\mathcal{M}_a\mathcal{M}_b^*$, where in the HNV model (solid black line) a = NP, CNP, CT, PP, PF, ΔP and $C\Delta P$, while in the FN (dashed red line) model a = NP, CNP, PF and ΔP. Diagrams labels are explained in [3]. E' denotes the energy of the outgoing muon. The contributions on diagonal are given by $|\mathcal{M}_a|^2$, below diagonal contributions from $2\Re\mathcal{M}_a\mathcal{M}_b^*$ are given.

5. T. Kitagaki, H. Yuta, S. Tanaka, A. Yamaguchi, K. Abe, et al., *Phys. Rev. D* **34**, 2554–2565 (1986).
6. K. M. Graczyk, D. Kielczewska, P. Przewlocki, and J. T. Sobczyk, *Phys. Rev. D* **80**, 093001 (2009).
7. K. M. Graczyk, J. Zmuda, and J. T. Sobczyk, *Phys. Rev. D* **90**, 093001 (2014).
8. E. Hernández, J. Nieves, and M. Valverde, *Phys. Rev. D* **76**, 033005 (2007).
9. G. Fogli, and G. Nardulli, *Nucl. Phys. B* **160**, 116 – 150 (1979).
10. J. A. M. Vermaseren (2000), `math-ph/0010025`.
11. A. Heck (2000), `https://www.nikhef.nl/~form/maindir/documentation/tutorial/book.pdf`.
12. K. M. Graczyk, D. Kiełczewska, P. Przewłocki, and J. T. Sobczyk, *Phys. Rev. D* **80**, 093001 (2009).
13. K. M. Graczyk, J. Żmuda, and J. T. Sobczyk, *Phys. Rev. D* **90**, 093001 (2014).

Study of FWHM Vertex Reconstruction Precision in SuperNEMO Demonstrator as a Function of Angle Between Electrons from $0\nu\beta\beta$

Miroslav Macko[1,2,3]
on behalf of the SuperNEMO collaboration

[1] *Institute of Experimental and Applied Physics, CTU in Prague, CZ-12800 Prague, Czech Republic*
[2] *FMFI, Comenius University, Mlynská dolina F1, SK-842 48 Bratislava, Slovakia*
[3] *Université de Bordeaux, CNRS/IN2P3, CENBG, F-33175 Gradignan, France*

Abstract. SuperNEMO experiment, which is designed to study $0\nu\beta\beta$, will take advantage of topological event reconstruction. It is a unique feature in the field. In order to establish proper cuts for data analysis the limitations on the reconstruction precision should be investigated. Proposed study offers analysis of precision of vertex reconstruction in SuperNEMO demonstrator based on simulations. The precision is studied as a function of angle between outgoing electrons. The paper also includes an analysis of used fitting methods.

Keywords: SuperNEMO, double-beta decay, vertex precision
PACS: 23.40.-s, 23.40.Bw, 14.60.Pq

SUPERNEMO EXPERIMENT

SuperNEMO is a unique $0\nu\beta\beta$ experiment [1]. Its demonstrator module is currently being in its latest phase of construction in LSM (Laboratoire Souterrain Modane) - the deepest European underground laboratory. While all of the other experiments in the field aim to study double-beta decay based on the analysis of energy spectrum, the uniqueness of SuperNEMO lies in the topological reconstruction of double-beta events on top of calorimetric measurement of energy carried by two electrons. Summary of double beta results and current or future experiments can be found in [2].

Other advantage of this experiment is its modularity and flexibility of choice of studied isotope. The whole project (after it will be finalized in the full planned scale) will consist of 20 modules. Each module can be separated into three main parts - source foil made of studied isotope (^{82}Se), tracker consisting of more than 2000 Geiger cells for reconstruction of event topology and finally, scintillating calorimeter walls giving information about energies of emitted electrons [3]. Simplified geometry can be seen in Figure 1. Modularity of the project allows scalability of the mass of used isotope by simple addition of extra modules. Even though, SuperNEMO is designed at the moment to study ^{82}Se, in principle, it can study any double-beta isotope which can be efficiently turned into form of thin foils (for example ^{150}Nd).

DESCRIPTION OF STUDIED PROBLEM

In double-beta decay, two electrons are emitted from the same nucleus of negligible size (point). If the experimental uncertainties are taken into account, it is inevitable to obtain two misplaced vertices on the foil (V_1 and V_2 in Figure 2 - right) after software track reconstruction. They are both representing more or less precisely the point of origin. It is important to evaluate the typical size of this misplacement in order to distinguish real double-beta decay electrons from random coincidences. The goal of this paper is an evaluation of the vertex reconstruction precision as a function of the angle between two electrons. This paper is using similar methods to [4] and [5].

The sketch of the problem can be seen in Figure 2. In the left part of the figure one can see an example of double-beta decay event as seen in the simulation. The discrete Geiger hits are reconstructed by software into continuous tracks. The right side of the Figure 2 represents the same situation after zooming. Foil vertices (V_1 and V_2) obtained after reconstruction are misplaced in respect to each other by vector $\vec{\Delta} = V_1 - V_2 = (\Delta_x, \Delta_y, \Delta_z)$. As the thickness of the foil is negligible (so it is Δ_x) I was interested only in the y and z components of $\vec{\Delta}$ (named Δ_y and Δ_z).

Another issue which I have to account for, is a definition of the angle between two electrons. Electrons undergo several scattering events before they leave the source foil which is changing their direction. Example can be seen in Figure 3. In the figure, I define two angles Φ_{decay} and Φ_{escape}. Φ_{escape} (in contrary to Φ_{decay}) is measurable experimentally.

RELATION BETWEEN Φ_{decay} AND Φ_{escape}

Let us evaluate a relation between Φ_{decay} and Φ_{escape}. As a first step, a sample of 3×10^7 events of $0\nu\beta\beta$ (from ^{82}Se) was generated, originating in the source foil. For simulation, Falaise 2.0.0 software package was used. It is software package based on Geant4 [6], specifically developed for needs of SuperNEMO collaboration. Subsequently, filters, introducing conditions from following list, were employed: exactly two calorimeter hits, exactly two associated calorimeter hits, exactly two vertices on source foil, exactly two

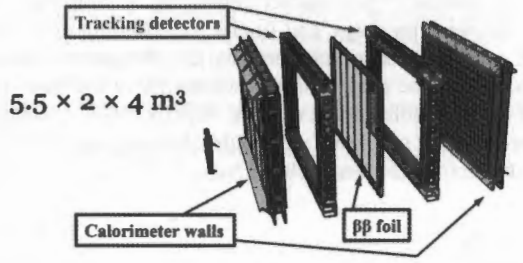

FIGURE 1. Overview of geometry of one SuperNEMO module.

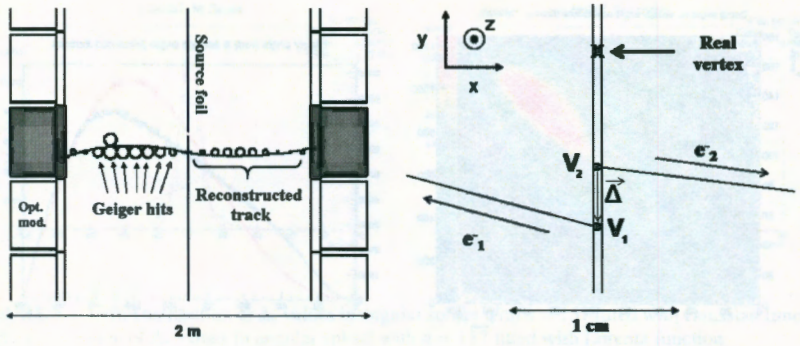

FIGURE 2. Left: Example output of $0\nu\beta\beta$ decay event from simulation performed by Falaise. Discrete circles represent Geiger hits obtained from tracker and the continuous curve represent track reconstructed by software. Right: Zoomed view onto the event depicted on the left side of the picture. One can clearly observe shift of the two vertices by vector $\vec{\Delta}$ due to experimental imprecisions.

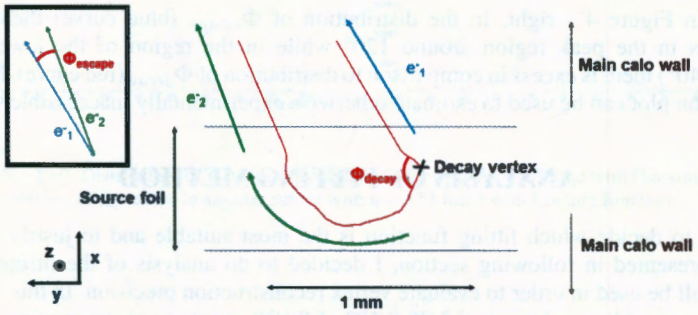

FIGURE 3. Close-up view onto the situation inside of the source foil right after the double-beta decay event occurs. Even though the thickness of the foil is relatively small, one can observe that it is thick enough for electrons to undergo several scatterings. Due to this fact, for the needs of this study, I defined two different angles: angle at the moment when decay happened (Φ_{decay}) and angle between electron momenta in the moment when they are leaving the source foil (Φ_{escape}).

reconstructed particles and exactly two negatively charged particles. They ensure that reconstructed event (as seen by detector) meets basic requirements of double-beta decay. The filters are explained in more detail in [4] and [5]. After filtration, only roughly 7.75×10^6 $0\nu\beta\beta$ events remained. For each of these events, the Φ_{decay} and Φ_{escape} were calculated and were scored into 2D histogram in Figure 4 - left.

One can observe that the majority of events are falling rather close to the $\Phi_{escape} = \Phi_{decay}$ line, however, the correlation plot is not symmetric in respect to aforementioned line, favouring smaller Φ_{escape}. It can be seen clearly in the angle spectra of the same

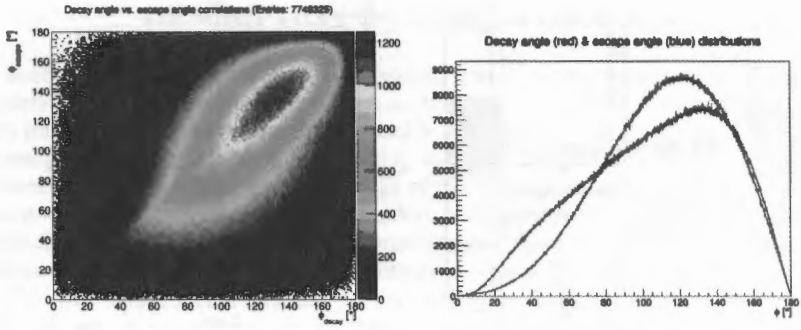

FIGURE 4. Left: Plot of correlation between Φ_{escape} and Φ_{decay} defined in Figure 3. Every bin of 1° by 1° size symbolize number of events with given values of Φ_{escape} and Φ_{decay}. The studied dataset was composed of roughly 7.75×10^6 $0\nu\beta\beta$ events of ^{82}Se. Right: Angular spectrum comparison for Φ_{decay} (red) and Φ_{escape} (blue). It is including the same dataset as the image on the left.

dataset in Figure 4 - right. In the distribution of Φ_{escape} (blue curve) there is lack of events in the peak region around 120° while in the region of the lower angles (around 40°) there is excess in comparison to distribution of Φ_{decay} (red curve). Proposed correlation plot can be used to estimate otherwise experimentally inaccessible Φ_{decay}.

ANALYSIS OF FITTING METHOD

In order to decide which fitting function is the most suitable and to justify obtained results presented in following section, I decided to do analysis of the fitting method which will be used in order to evaluate vertex reconstruction precision. In this section, I used the same filtered dataset of 7.75×10^6 of $0\nu\beta\beta$ events as in the previous section. For each event $\Delta_y = V_{1y} - V_{2y}$ and $\Delta_z = V_{1z} - V_{2z}$ was calculated. Then the dataset is divided into what I call "angular subsets". Each angular subset is consisting of events which fulfil the condition: $n° < \Phi_{escape} < (n+1)°$ where $n = 0, 1, 2, ..., 179$. For each angular subset histograms of Δ_y and Δ_z were plotted. Example of such distributions can be found in Figures 5 and 6 (case of $n = 157$). In order to obtain what I call "FWHM vertex reconstruction precision" the FWHM is extracted from all such histograms in all angular subsets.

However, the choice of the fitting function was not trivial. In the mentioned Figures 5 and 6 one can also notice that in the case of Δ_y Lorentz function in the form:

$$f_L(x) = \frac{A}{x^2 + \gamma^2} \tag{1}$$

fits the distribution more precisely than standard Gaussian distribution (without normalization) in form:

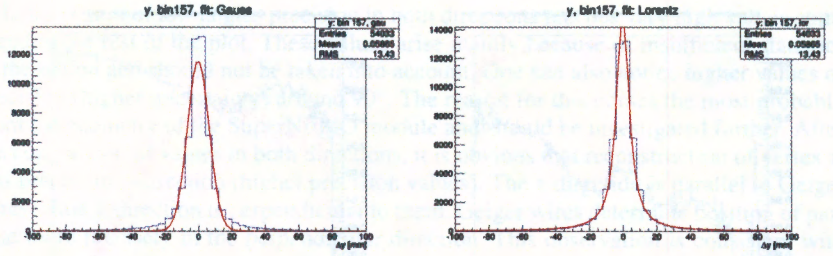

FIGURE 5. Left: Distribution of Δ_y values in angular subset with $n = 157$ fitted with Gaussian function. Right: Distribution of Δ_y values in angular subset with $n = 157$ fitted with Lorentz function.

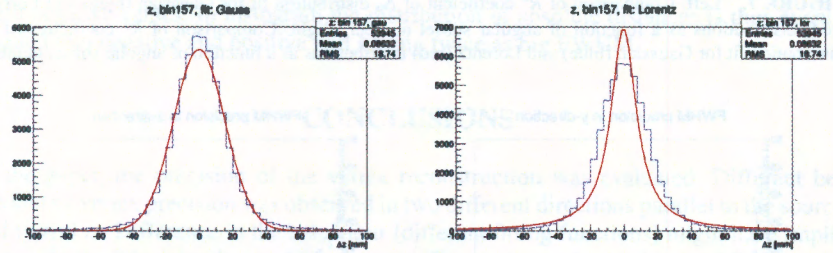

FIGURE 6. Left: Distribution of Δ_z values in angular subset with $n = 157$ fitted with Gaussian function. Right: Distribution of Δ_z values in angular subset with $n = 157$ fitted with Lorentz function.

$$f_G(x) = Ae^{-\frac{(x-\mu)^2}{2\sigma^2}}. \tag{2}$$

Moreover, in case of the distribution of Δ_z it works the opposite and the distribution can be fitted by Gaussian function.

To investigate further, whether this is just a coincidence in case of $n = 157$, or, whether it works the same way for all events regardless of Φ_{escape}, I created similar Δ_y and Δ_z histograms for all possible angles (with step of 1°) and fitted each one with both Lorentz and Gauss distributions. I calculated R^2 coefficient for each fit. The results are shown in Figure 7.

The results support my observation from case when $n = 157$. This is the reason why in the following analysis Lorentz function is used to fit Δ_y distributions while Δ_z distributions are fitted with standard Gaussian.

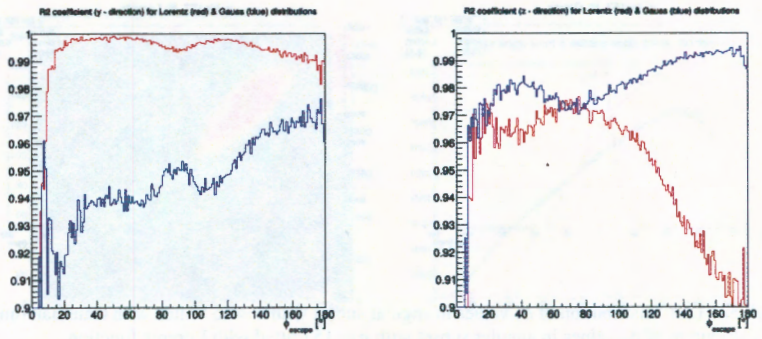

FIGURE 7. Left: Comparison of R^2 coefficient of Δ_y distribution fit for Gaussian (blue) and Lorentz (red) distributions as a function of angular subset number. Right: Comparison of R^2 coefficient of Δ_z distribution fit for Gaussian (blue) and Lorentz (red) distributions as a function of angular subset number.

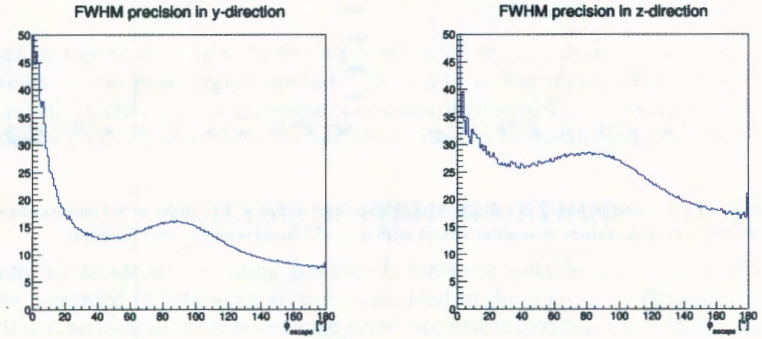

FIGURE 8. Left: FWHM precision in y-direction as a function of Φ_{escape}. Right: FWHM precision in z-direction as a function of Φ_{escape}.

RESULTS

Presented work is a continuation of the study from [4]. All the angular subsets' histograms of Δ_y and Δ_z values were fitted in fashion discussed in previous section. The fit provides FWHM value which I named (for the needs of the article) as "FWHM vertex reconstruction precision". The higher the value is, the further away from each other both reconstructed vertices are, thus, the more imprecisely reconstruction performs. For lower values, naturally, it works the opposite. In the Figure 8 one can see how the precision of the vertex reconstruction performs depending on Φ_{escape} in both directions parallel to source foil (y and z).

In the region of low angles precision in both directions reaches very high values compared to the rest of the plot. These values arise mainly because of insufficient statistics in the region and should not be taken into account. One can also notice higher values of precision (higher uncertainty) around 90°. The reason for this comes the most probably from the geometry of the SuperNEMO module and should be investigated further. After the comparison of values in both directions, it is obvious that reconstruction of vertex is less precise in z-direction (higher precision values). The z-direction is parallel to Geiger wires while y-direction is perpendicular to them. Geiger wires determine position of particle more precisely in the perpendicular direction. This observation is consistent with my obtained results.

It is important to note at this point, that values of FWHM precision presented in the plots should be divided by factor of two in order to obtain proper absolute uncertainties on vertex determination. It is due to the definition of variables Δ_y and Δ_z. They are not representing an absolute value (distance) but a difference of two vertices which might yield negative values. In histogram the distribution of absolute distances is thus evenly divided into negative and positive part having twice as big FWHM.

CONCLUSIONS

In the paper, the precision of the vertex reconstruction was evaluated. Different behaviour of vertex precision was observed in two different directions parallel to the source foil (y and z). Difference in the behaviour (different fitting functions) might have implication for the fiducial volume of the detector. The study can be used to establish cuts on angle after the SuperNEMO will start collecting data.

ACKNOWLEDGMENTS

This work was supported by the Ministry of Education, Youth and Sports of the Czech Republic under the Contract Number 02.1.01/0.0/0.0/16 013/0001733 and by Comenius University in Bratislava grant for youth No. UK/213/2017.

REFERENCES

1. R. Arnold, C. Augier, et al., *Eur. Phys. J.* **C 70**, 927–943 (2010).
2. A. S. Barabash, "Brief review of double beta decay experiments," in *Proceedings, 2nd International Conference on Particle Physics and Astrophysics (ICPPA 2016): Moscow, Russia, October 10-14, 2016*; arXiv:1702.06340.
3. A. S. Barabash, et al., *Nucl. Instrum. Meth.* **A 868**, 98–108 (2017).
4. M. Macko, *AIP Conference Proceedings* **1894**, 020014 (2017).
5. M. Macko (2017), dissertation thesis project.
6. S. Agostinelli, J. Allison, et al., *Nucl. Instrum. Meth.* **A 506**, 250 – 303 (2003).

Optimisation of metallic magnetic calorimeter arrays with embedded Holmium-163 for the ECHo experiment

Federica Mantegazzini for the ECHo Collaboration

Kirchhoff Institute for Physics, Heidelberg University, Heidelberg, Germany

Abstract. Presently, the only model independent approach which can be used to determine the absolute scale of neutrino masses consists in the precision measurement of the kinematics of atomic weak decays, in particular of the ^{3}H β-decay and the ^{163}Ho electron capture (EC). The Electron Capture in ^{163}Ho experiment (ECHo) is designed to reach sub-eV sensitivity on the electron neutrino mass by means of the analysis of the calorimetrically measured EC spectrum of ^{163}Ho. Arrays of metallic magnetic calorimeters (MMC) with enclosed ^{163}Ho and featuring high energy resolution and fast response time have been developed for the ECHo experiment. The current phase of the ECHo experiment, ECHo-1k, characterised by a source of 1 kBq enclosed in about 100 single pixels, has been conceived to reach a sensitivity on the electron neutrino mass at the level of 10 eV and to set the detector design, the read-out scheme and cryogenic set-up, in order to be suitable for the following ECHo phases, with the goal to achieve sub-eV sensitivity.

Keywords: electron neutrino mass, metallic magnetic calorimeters, ECHo
PACS: 14.60.Pq; 29.40.Wk

INTRODUCTION

The electron neutrino mass can be investigated by studying electron capture processes. In these decays an electron from an inner atomic shell is captured by the nucleus and one electron neutrino is emitted, leading to an excited daughter atom. The excitation energy is released through the emission of x-rays and/or electrons which can then be measured.

The current limit on the electron neutrino mass is $m(\nu_e) < 225$ eV/c^2 95% C.L. and it was achieved by analysing the Internal Bremsstrahlung in Electron Capture (IBEC) spectrum of ^{163}Ho [1]. The goal of the ECHo experiment is to improve this limit and to reach a sensitivity below 1 eV on the electron neutrino mass. The strategy to achieve this goal is based on the analysis of the calorimetrically measured EC spectrum of ^{163}Ho, as proposed by De Rujula and Lusignoli [2]. To perform such a measurement, the ^{163}Ho source should be enclosed in suitable detectors, so that all the energy emitted in the decay - besides the neutrino energy - is measured. The resulting energy spectrum is characterised by several resonances, centered at about the binding energy of the captured electrons with respect to the potential of the daughter nucleus. A non-zero neutrino mass affects the corresponding energy spectrum in the end-point region (figure 1). Since the fraction of events in the end-point region of the spectrum increases if the Q-value of the process is small, the isotope ^{163}Ho is currently the best choice, having an extremely low Q-value: $Q_{EC} = 2.833 \pm 0.030_{stat} \pm 0.015_{sys}$ - as recently determined by the ECHo collaboration [3].

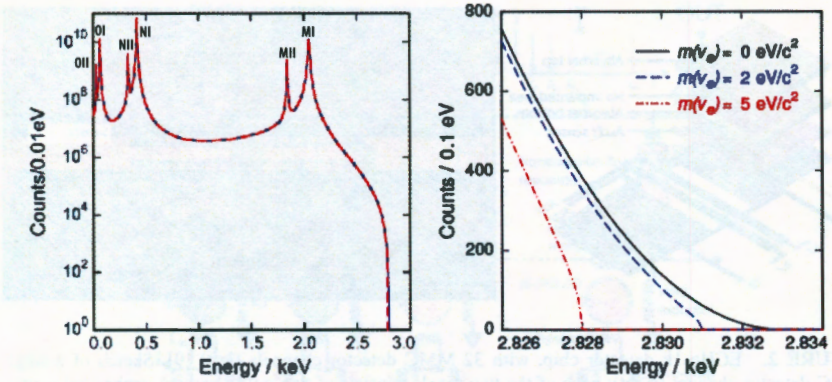

FIGURE 1. Electron capture spectrum of ^{163}Ho. The zoom on the endpoint region shows the effect of a non-zero electron neutrino mass [4].

DETECTORS AND READ-OUT

In order to perform a fully calorimetric measurement of the EC spectrum with the required energy resolution, metallic magnetic calorimeters (MMC) with ^{163}Ho embedded source have been developed [5] [6].

MMCs are near equilibrium detectors operating at very low temperatures, below 100 mK. They consist of an absorber, optimised for the particles to be detected, which is well thermally connected to the temperature sensor, a paramagnetic Au:Er sample sitting in an external magnetic field generated by a persistent current flowing in a superconducting meander-shaped coil which also works as pick-up coil. The sensor is then weakly coupled to the thermal bath. For the ECHo experiment, ^{163}Ho atoms are enclosed in the absorber, as indicated in Figure 2 (left). When a particle interacts in the absorber releasing an energy E, the temperature T of the detector increases and the magnetisation M of the sensor decreases. The change of magnetisation ΔM leads to a change of magnetic flux $\Delta\Phi$ in the superconducting pick-up coil:

$$\Delta\Phi \propto \frac{\Delta M}{\Delta T}\Delta T \simeq \frac{\Delta M}{\Delta T}\frac{E}{C} \tag{1}$$

where C is the total heat capacity of the detector.

The pick-up coil is connected to a Superconducting Quantum Interference Device (SQUID) that can precisely read-out the change in magnetic flux and translate it into a voltage signal. MMCs are characterised by an excellent energy resolution $\Delta E_{\mathrm{FWHM}} \approx 1.6$ eV, a fast rise-time $\tau_r \approx 90$ ns and a very good linearity [7]. For that reasons they have been chosen as detector technology by the ECHo collaboration.

For the first phase of the ECHo experiment, ECHo-1k, a 64-pixel detector array has been designed, fabricated and tested.. The detector geometry has been optimised for the ^{163}Ho implantation and for that a new microfabrication process has been developed.

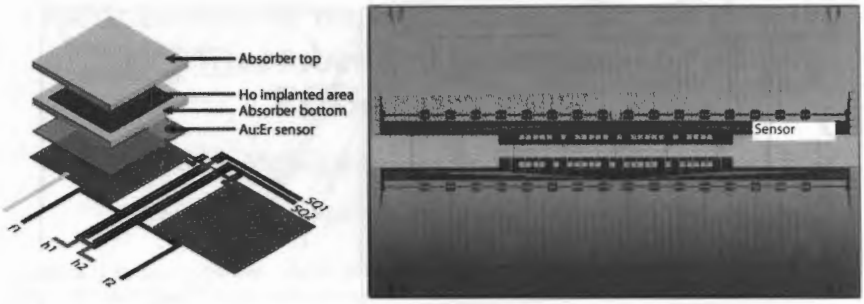

FIGURE 2. ECHo-1k detector chip, with 32 MMC detector channels (left) [9]. Sketch of a single MMC detector channel (right): each of the two pixels consists of two gold aborbers, embedded source, paramagnetic sensor and meander-shaped pick-up coil [6].

A picture of the ECHo-1k chip is shown in Figure 2 (right). It consists of 64 MMC pixels, corresponding to 32 detector channels. The absorber of each pixel is made of two gold layers having dimension 180 μm x 180 μm x 5 μm, a paramagnetic Ag:Er sensor (180 μm x 180 μm x 1.3 μm) and a superconducting meander-shaped pick-up coil. The implantation area defined on the first absorber layer is 150 μm x 150 μm, so that the ^{163}Ho source is completely surrounded by the absorber material and the resulting detection quantum efficiency for the energy released in the ^{163}Ho decay is close to 100%.

In order to measure a high statistics EC spectrum, the read-out of a large number of detectors (in the order of 10^4 [4]) is required and therefore the ECHo collaboration is currently developing a new multiplexing technique based on the microwave SQUID multiplexing concept [8]. The corresponding scheme is shown in Figure 3: each detector is coupled to a rf-SQUID which works as non-linear inductor. The rf-SQUIDs are then also coupled to coplanar waveguide resonators, each of them with a characteristic resonance frequency. When an event occurs in the detector, the magnetic flux in the rf-SQUID changes and therefore the resonance frequency of the resonant circuit is shifted. It is then possible to read-out hundreds or thousands of detectors simultaneously by injecting a microwave frequency comb through a common transmission line and monitoring the amplitude and phase of the transmitted signal.

The ECHo-1k detector design performance fulfils the requirements for the first phase of ECHo: the expected energy resolution is 5 eV FWHM at an operational temperature of 30 mK and the rise-time is about 300 ns with multiplexed read-out.

The detector chip with implanted ^{163}Ho source is currently being tested in a dedicated dilution refrigerator at an operating temperature of 10 mK.

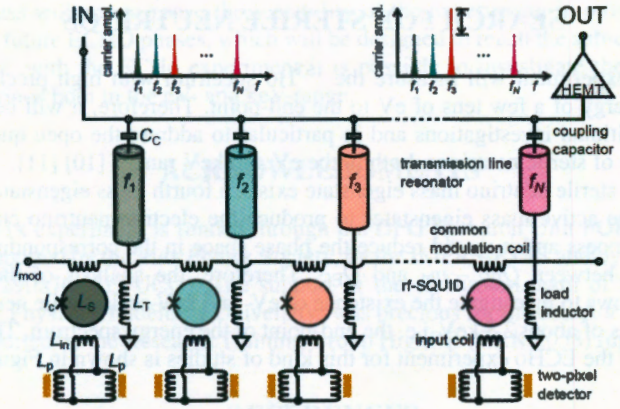

FIGURE 3. Microwave multiplexing scheme for MMC detectors read-out. A signal in a single detector leads to a resonance frequency shift of the associate resonator. [4]

SENSITIVITY ON THE ELECTRON NEUTRINO MASS

The final goal of the ECHo collaboration is to reach a sensitivity below 1 eV on the electron neutrino mass. The sensitivity of the ECHo experiment is influenced mainly by three factors:

- The total number of events acquired during the measurement
- The energy resolution of the detectors ΔE_{FWHM}: it defines the resolving power of the measurement of the ^{163}Ho spectrum
- The intrinsic background source represented by the unresolved pile-up fraction, which is proportional to the detector activity A and the time resolution of the detector, i.e. the rise-time τ_{rise}: $f_{pu} = A \cdot \tau_{rise}$

The ECHo experiment is planned to proceed through different phases characterised by increased ^{163}Ho activity implanted in the detectors. During the current phase, ECHo-1k - distinguished by a total activity of about 1 kBq - the collaboration aims to reach a sensitivity of 10 eV and to prove the scalability of the experiment. In order to reach a sub-eV sensitivity a total activity of at least 1 MBq is required and it will be accomplished in an experiment called ECHo-1M. In table 1 the main requirements for these two experiments are summarised.

TABLE 1. Experimental requirements for the ECHo phases [4].

Phase	Sensitivity on $m(\nu_e)$	Statistics	Activity	Detector resolution
ECHo-1k	≤ 10 eV	$\geq 10^{10}$	1 kBq	≤ 5 eV
ECHo-1M	≤ 1 eV	$\geq 10^{14}$	1 MBq	≤ 3 eV

SEARCH FOR STERILE NEUTRINOS

The ECHo experiment will measure the ^{163}Ho spectrum with high precision from a threshold energy of a few tens of eV to the end-point. Therefore, it will be possible to perform additional investigations and in particular to address the open question about the existence of sterile neutrinos, both in the eV and keV ranges [10] [11].

If a fourth sterile neutrino mass eigenstate exists, a fourth mass eigenstate would mix with the three active mass eigenstates to produce the electron neutrino emitted in the ^{163}Ho EC process and it would reduce the phase space in the corresponding spectrum for energies between $Q_{EC} - m_4$ and Q_{EC}. Therefore, the analysis of the ^{163}Ho EC spectrum allows to investigate the existence of eV- and keV-scale sterile neutrinos up to masses values of about 2.8 keV, i.e. the end-point of the energy spectrum. The estimated sensitivity of the ECHo experiment for this kind of studies is shown in Figure 4.

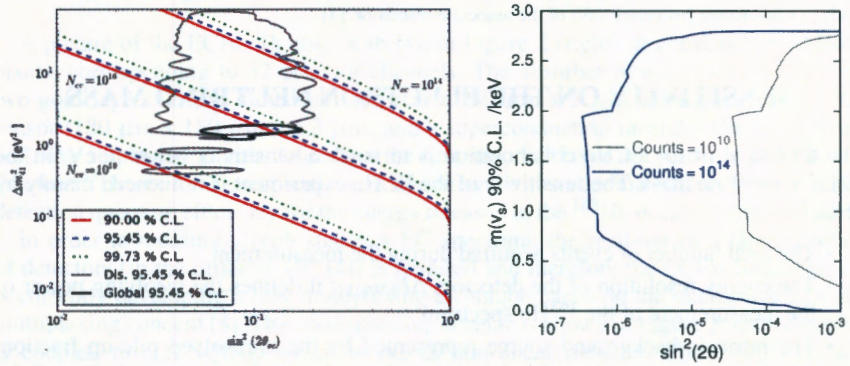

FIGURE 4. Estimated sensitivity curves for the investigation of sterile neutrinos. In the left plot the sensitivity on eV-range sterile neutrinos at 90% C.L., 95.45% C.L. and 99.73% C.L. are shown [10]. In the right plot the estimated sensitivity on keV-scale sterile neutrinos at 90% C.L. for two different statistics is shown [11].

CONCLUSIONS

The determination of the absolute scale of neutrinos masses is one of the most pressing open questions in the framework of elementary particles physics. The ECHo experiment is designed to reach sub-eV sensitivity on the electron neutrino mass exploiting the electron capture process in ^{163}Ho. The detector technology used by ECHo is based on MMCs with implanted ^{163}Ho source and operated at millikelvin temperature. The detector optimisation as well as the read-out scheme and the cryogenic measurement set-up have been finalised for the current phase, ECHo-1k, characterised by an activity of 1 kBq. The goals of this phase are to reach a sensitivity below 10 eV on the electron

neutrino mass will and to prove the scalability of the experiment, in order to pave the way for the future ECHO phases, which will be designed to reach the sub-eV sensitivity. Furthermore, with the ECHo experiment it is possible to investigate the existence of sterile neutrinos both in the eV- and keV-range.

ACKNOWLEDGMENTS

The ECHo-1k experiment is funded through the DFG Research Unit FOR 2202 ECHo and it is supported by the Max Planck Society, by the IMPRS-PTFS and by the EU (ERC Grant No. 290870-MEFUCO). The support of the cleanroom team of the Kirchhoff Institute for Physics (Heidelberg University) was precious for the detector development. F.M is supported by the Research Training Group HighRR (GRK 2058) funded by DFG.

REFERENCES

1. P. T. Springer et al., *Phys. Rev. A* **35**, 679 (1987).
2. A. De Rujula and M. Lusignoli *Phys. Lett. B* **118**, 429 (1982).
3. S. Eliseev et al., *Phys. Rev. Lett.* **115**, 062501 (2015).
4. L. Gastaldo et al., *EPJ ST* **226**, 8 (2017).
5. A. Fleischmann et al., *AIP Conference Proceedings* 1185, 571 (2009).
6. L. Gastaldo et al., *NIM A* **711**, 150-159 (2013).
7. K.D. Irwin and G.C. Hilton, *Topics in Applied Physics* **99**, 63 (2005).
8. J. A. B. Mates et al., *Applied Physics Letters* **92**, 2, 023514 (2008).
9. S. Kempf at al., *AIP Advances* **7**, 015007 (2017).
10. L. Gastaldo, C. Giunti, E. M. Zavanin *JHEP* **6**, 61 (2016).
11. R. Adhikari et al., *JCAP* **01**, 025 (2017).

Pulse Shape Simulations for the GERDA Experiment

Michael Miloradovic

Physik Institut der Universität Zürich, Zürich, Switzerland

Abstract. The search for the neutrinoless double beta decay ($0\nu\beta\beta$) of ^{76}Ge with the Germanium Detector Array (GERDA) experiment has yielded the most stringent lower limit on the $0\nu\beta\beta$ half-life of ^{76}Ge with $T_{1/2}^{0\nu\beta\beta} > 8.0 \cdot 10^{25}$ yr at a 90% C.L. in the latest results [1, 2]. Due to the achieved background-free scenario, the experiment's sensitivity grows linearly with exposure and is expected to surpass 10^{26} yr within 2018. This success has motivated the formation of the LEGEND (Large Enriched Germanium Experiment for Neutrinoless $\beta\beta$ Decay) collaboration to design the next generation array with the goal of reaching one ton of germanium detectors [3]. The development pulse shape simulations for germanium detectors and connecting the energy deposition MC simulations to this signal shape modeling run through the same analysis chain will allow the creation of a background model after Pulse Shape Discrimination (PSD) and benefit the understanding of the background, current and upcoming analysis of GERDA data, and future efforts of the LEGEND collaboration [3].

Keywords: neutrinoless double beta decay, germanium
PACS: 23.10.-s; 21.60.-n; 23.40.Bw; 23.40.Hc

INTRODUCTION

Some of the most important questions in modern particle physics and cosmology could be answered through the investigation of the neutrino nature. From the absolute neutrino mass scale and hierarchy to a possible explanation of the matter antimatter asymmetry in the universe [4, 5].

Wolfgang Pauli predicted the existence of the neutrino in 1930 as a completely new, undetected elementary particle to maintain the conservation of energy and momentum in the beta decay [6]. In 1937, Ettore Majorana suggested that the neutrino could be its own anti-particle. The resulting equation introduces a Majorana mass for the neutrino [7]. The ν and $\bar{\nu}$ could be the two chirality states of a single particle. A resulting extension of the Standard Model by heavy sterile neutrinos would induce CP violating decays of sterile neutrinos, spontaneously generating leptons. The increased number of leptons in comparison to anti-leptons results in a lepton asymmetry in the early universe. A conversion of leptogenesis into baryogensis could thus lead to the observed baryon asymmetry and the universe as we know it [5].

The prime avenue to directly probe this fundamental characteristic and simultaneously obtain information on the absolute neutrino masses is the neutrinoless double beta decay. The discovery of this postulated decay channel would prove that total lepton number is not conserved in nature and that neutrinos have a Majorana mass component. In consequence, exploring the Majorana nature of the neutrinos could help reconcile major

cosmological issues of modern physics.

THE GERDA EXPERIMENT

The Germanium Detector Array (GERDA) experiment at the Laboratori Nazionali del Gran Sasso (LNGS) searches for the neutrinoless double beta decay ($0\nu\beta\beta$) of ^{76}Ge. It employs high-purity germanium diodes isotopically enriched in ^{76}Ge to $>86\%$, acting simultaneously as the detector and source material [8]. The germanium detectors are operated directly submerged in liquid argon (LAr), shown in Fig. 1. The detectors on the inner core string are not enriched and thus called natural Ge detectors. Surrounding the LAr is a water tank Cherenkov veto.

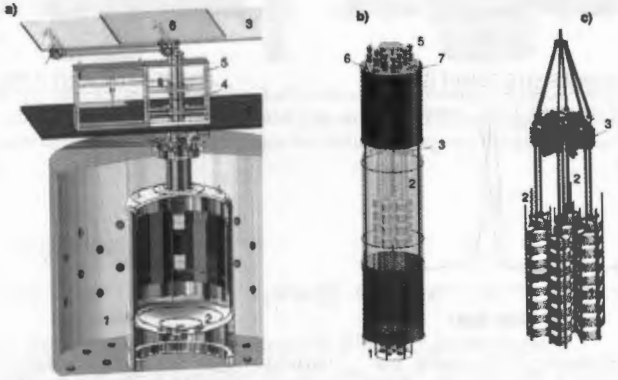

FIGURE 1. Schematic view of the GERDA experiment. **Left** – Overview: (1) water tank muon veto with 10 m diameter , (2) LAr cryostat with 4 m diameter (2), (3-5) clean room, lock, glove box, and (6) plastic muon veto system. **Centre** – Phase II LAr veto system: (1, 5) PMTs (2) fiber curtain, (3) SiPMs, (4) copper cylinders (6-7) calibration source slots. **Right** – Germanium detector array: (1) germanium detectors arranged in 7 strings, (2) bias and readout cables, (3) amplifiers.

Phase II of GERDA has been taking data since December 2015 in stable conditions with 40 germanium detectors (38 kg). In the last unblinding of the data, no hint for a $0\nu\beta\beta$ decay signal of ^{76}Ge has been found, resulting in the combined lower limit of $T_{1/2}^{0\nu\beta\beta} > 8.0 \cdot 10^{25}$ yr at a 90% C.L. [1, 2]. The background index (BI) at $Q_{\beta\beta}$ for the BEGe detectors on the order of 10^{-4}cts/(keV·kg·yr) is the world's best background level in comparison to competing experiments (taking resolution into account) and was published in the journal Nature [2]. In this practically background free scenario, the sensitivity grows linearly with time as opposed to the square root. The experiment's sensitivity is expected to surpass 10^{26} yr within 2018. Due to these great results, a new global collaboration has been formed in January 2017 named LEGEND (Large Enriched Germanium Experiment for Neutrinoless $\beta\beta$ Decay), which will be based on the successful techniques used in GERDA to pave the way for a ton-scale germanium experiment [3].

PULSE SHAPES OF GERMANIUM DETECTORS

Incident charged particles and photons ionise the germanium crystals, producing charge carriers in the conduction band proportional to their energy. Under an applied reverse bias voltage on the semiconductor, the electrons and holes drift towards the electrodes. The resulting induced current on the read-out electrode is then measured. Figure 2 depicts a schematic that shows the differences between a signal induced by a signal as a Single Site Event (SSE) or background such as γ-rays as a Multiple Site Event (MSE). The deposited energy is reconstructed from the pulse shapes [9]. Due to the distinct differences in induced signal, the event topologies can be discerned through Pulse Shape Discrimination (PSD).

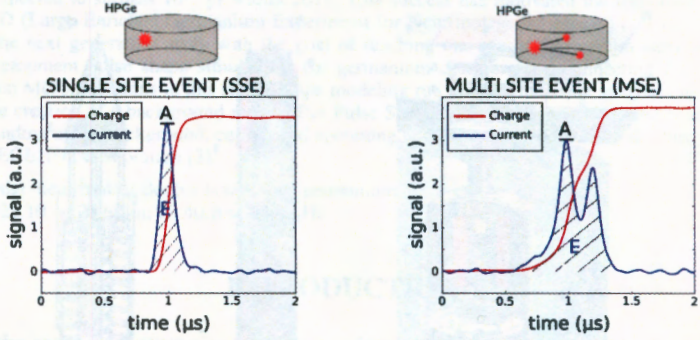

FIGURE 2. Schematic of Ge signals: **Left** – Signal-like Single Site Event (SSE) depositing energy in the detector only in a single location. **Right** – Background-like Multi Site Event (MSE) that deposits energy in multiple locations, e.g. a γ-ray.

PULSE SHAPE SIMULATIONS

The goal is to develop pulse shape simulations that model the germanium signal shape. This will be done by integrating the Monte Carlo simulations with GEANT4 into the entire GERDA data production and processing chain. Pulse shape simulation will also provide an estimate of the $0\nu\beta\beta$ signal efficiency to compare it to the ^{208}Tl Double Escape Peak (DEP) one.

Simulations of the electric fields and potentials with the ADL3 Simulation Toolkit [10] adapted to GERDA [11] have been performed for the BEGe detectors. A BEGe type germanium detector consists of a groove that separates the positively biased inner p+ readout electrode from the outer grounded n+ electrode. The path of charge carriers depends on the applied high voltage and thus the electric potential inside the detector. The simulated electric potential is shown in Figure 3 on the left for the example of the specific geometry of detector GD35A.

The induced charge on the readout p+ electrode is determined with the Shockley Ramo Theorem by simulating the weighting potential $\psi(\vec{x})$ wherein the readout elec-

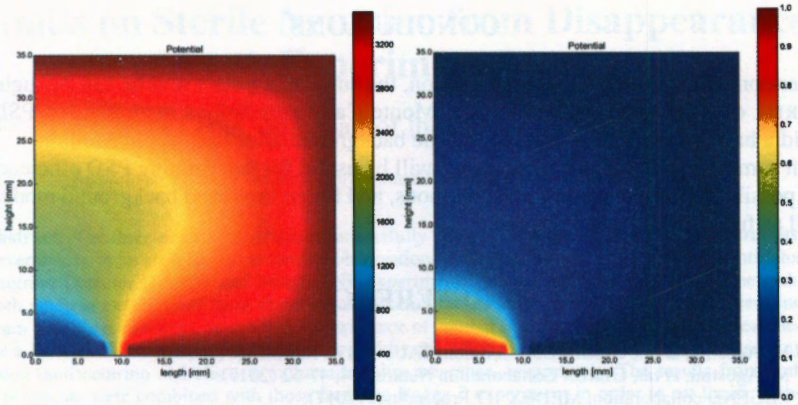

FIGURE 3. BEGe detector field simulation: Left is the electric potential of BEGe GD35A determining the calculated path of charge carriers. The potential is in terms of applied voltage in Volts. On the right, the weighting potential of BEGe GD35A determines the induced charge on the electrode with the Shockley Ramo Theorem.

trode is set to unit potential:

$$I = -q\nabla\psi(\vec{x}) \cdot \vec{v}_{drift}\,. \tag{1}$$

The simulated weighting potential is shown in Figure 3 on the right.

After applying electronics response to the simulated germanium pulses, they can be compared to real GERDA Phase II data. This will be used in the future to verify the germanium detector signal model. Stacked real data pulses of the DEP and the FEP, as shown in Figure 4, reveal a characteristic shape of germanium signal at the DEP (and for α-events). In this way, a comparison of real characteristic average pulses shapes to simulation can be done.

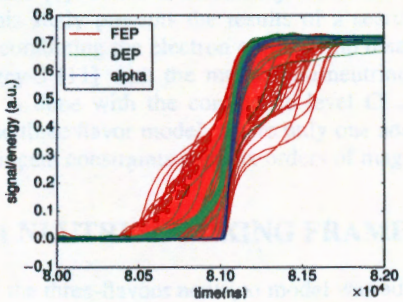

FIGURE 4. The ^{208}Tl Full Energy Peak (FEP) in red exhibits a wide range of different pulse shapes falling into Single Site Event (SSE) and Multi Site Event (MSE) categories. The Double Escape Peak (DEP) however as a very localised interaction and can thus only ever be a SSE and is thus characterised by a unique shape identified as a typical SSE shape which the simulations can be compared to.

CONCLUSIONS

After comparison to data and optimisation, the simulated pulses will be run through the GERDA data production chain to gain Monte Carlo simulations incorporating PSD to build a background model that models the background after PSD application.

In summary, pulse shape simulations will be useful for determining PSD efficiencies, the possibility to develop new PSD methods, and for an improved background model, as well as future detector development.

REFERENCES

1. M. Agostini, *et al.*, GERDA Collaboration, TAUP 2017 Proceedings (2017).
2. M. Agostini, *et al.*, GERDA Collaboration, Nature **544**, 47-52 (2017).
3. LEGEND collaboration, MEDEX '17 Proceedings (2017).
4. M. Fukugita, T. Yanagida, Phys. Lett. B **174**, 45 (1986).
5. S. Davidson, *et al.*, Phys. Rep. **466**, 105-177 (2008).
6. W. Pauli, "Brief an die Gruppe der Radioaktiven...", Zürich (1930).
7. E. Majorana, Il Nuovo Cimento **14**, 4 (1937).
8. K.-H. Ackermann, et al., GERDA Collaboration, Eur.Phys.J. C **73**, 2330 (2013).
9. M. Agostini, *et al.*, GERDA Collaboration, Eur. Phys. J. C **75**, 39 (2015).
10. B. Bruyneel *et al.*, P. Eur. Phys. J. A **52**, 70 (2016).
11. M. Salathe, PhD Thesis (2015).

Limits on Sterile Neutrino from Disappearance Experiments

Luis Mora Lepin, on behalf of the Daya Bay Collaboration

Instituto de Física, Pontificia Universidad Católica de Chile, Santiago, Chile

Abstract. The three-neutrino model can successfully explain the majority of experimental results. Nevertheless, there are a few experimental observations including those from the Liquid Scintillator Neutrino Detector (LSND) and MiniBooNE experiments that do not fit within that framework. Both of these experiments have observed an electron antineutrino excess in a muon antineutrino beam over short baselines, suggesting the existence of another neutrino state. Independent searches for a light sterile neutrino have been performed by the MINOS and Daya Bay experiments using muon (anti)neutrino and electron antineutrino disappearance, respectively. The results from both experiments were combined with those from the Bugey-3 experiment in order to set limits in the $\sin^2(2\theta_{\mu e})$ - Δm^2_{41} parameter space using a minimally extended four-neutrino model. The parameter space allowed by LSND and MiniBooNE was excluded for $\Delta m^2_{41} < 0.8$ eV^2 at 95% CL$_s$.

Keywords: light sterile neutrino, Daya Bay, MINOS, Bugey-3
PACS: 14.60.St; 14.60.Pq

INTRODUCTION

There are a few neutrino experiments whose results are not well explained by the three-flavour model, and serve as a motivation for the introduction of additional neutrino states. Some of these observations are the Reactor anomaly [1], the Gallium anomaly [2], and particular accelerator experiments results [3,4]. This letter addresses the LSND [3] and MiniBooNE [4] observations.

These additional neutrino states beyond the known active ones are referred to as sterile, because they do not interact via any of the Standard model forces according to precise electroweak measurements [5]. There is essentially no restriction in their number or in their mass range. This study presents the results of a search for light (< 0.1 eV) sterile neutrino mixing combining the electron antineutrino disappearance results from Daya Bay [9] and Bugey-3 [11] with the muon (anti)neutrino results from MINOS [10]. The combination is done with the confidence level CL$_s$ method [7,8] using a minimal extension of the three flavor model, where only one additional sterile neutrino is included, yielding stringent constraints over six orders of magnitude in Δm^2_{41} [6].

THE 3+1 NEUTRINO MIXING FRAMEWORK

A minimal extension of the three-flavour neutrino model was adopted in the search of a light sterile neutrino. This framework includes just one sterile flavor and the corresponding mass eigenstate. The muon to electron neutrino oscillation probability for LSND and

MiniBooNE is a function of the propagation length L, the energy E, and the elements of the 4x4 unitary mixing matrix U such that:

$$P_{\nu_\mu \to \nu_e} = \mid \sum_i U_{li} U^*_{l'i} e^{-i(m_i^2/2E)L} \mid^2 \tag{1}$$

The equation can be simplified for the region where $\Delta m^2_{41} \ll \mid \Delta m^2_{32} \mid$ and for short baselines ($\Delta m^2_{32} L/4E \approx 0$) to:

$$P_{\nu_\mu \to \nu_e} \approx 4 \mid U_{e4} \mid^2 \mid U_{\mu 4} \mid^2 \sin^2(\frac{\Delta m^2_{41} L}{4E}) \approx P_{\bar{\nu}_\mu \to \bar{\nu}_e} \tag{2}$$

Such oscillations with amplitude $4 \mid U_{e4} \mid^2 \mid U_{\mu 4} \mid^2$ could serve as an explanation for the electron antineutrino excess observed by these experiments. To examine their observations, it is necessary to have access to both terms in the amplitude. The first can be constrained from the electron antineutrino disappearance measurement performed in Daya Bay [9] and Bugey-3 [11]. The second term can be constrained from the muon (anti)neutrino disappearance measurements done in MINOS [10]. The survival probability for both experiments is:

$$P^{DYB}_{\bar{\nu}_e \to \bar{\nu}_e} = 1 - 4 \sum_{k>j} \mid U_{ek} \mid^2 \mid U_{ej} \mid^2 \sin^2(\frac{\Delta m^2_{kj} L}{4E}) \tag{3}$$

$$P^{MINOS}_{\bar{\nu}_\mu \to \bar{\nu}_\mu} = 1 - 4 \sum_{k>j} \mid U_{\mu k} \mid^2 \mid U_{\mu j} \mid^2 \sin^2(\frac{\Delta m^2_{kj} L}{4E}) \tag{4}$$

The unitary matrix U for the 3+1 model can be parametrized by $U = R_{34} R_{24} R_{14} R_{23} R_{13} R_{12}$ where R_{ij} is the rotational matrix for the mixing angle θ_{ij}, yielding:

$$\begin{aligned} \mid U_{e4} \mid^2 &= \sin^2\theta_{14} \\ \mid U_{\mu 4} \mid^2 &= \sin^2\theta_{24}\cos^2\theta_{14} \\ 4 \mid U_{e4} \mid^2 \mid U_{\mu 4} \mid^2 &= \sin^2 2\theta_{14}\sin^2\theta_{24} \equiv \sin^2 2\theta_{\mu e} \end{aligned} \tag{5}$$

THE CL_s METHOD

The CL_s method [7,8] is a two-hypothesis statistical test which compares the three-flavour (null) hypothesis (here referred to as 3ν) to the alternative four-flavour hypothesis (referred to as 4ν). The method is based on the construction of $\Delta\chi^2 = \chi^2_{4\nu} - \chi^2_{3\nu}$,

where $\chi^2_{4\nu}$ is the χ^2 value resulting from the fit assuming a four-flavour hypothesis, and $\chi^2_{3\nu}$ is the χ^2 value from the fit considering the three-flavour hypothesis. The $\Delta\chi^2$ observed with data, $\Delta\chi^2_{obs}$, is compared to the $\Delta\chi^2$ expected in the case that the three-flavour hypothesis is true, or the four-flavour hypothesis is true. The CL_s is defined through:

$$\begin{aligned} CL_{H_0} &= P(\Delta\chi^2 \geq \Delta\chi^2_{obs} \mid 3\nu) \\ CL_{H_1} &= P(\Delta\chi^2 \geq \Delta\chi^2_{obs} \mid 4\nu) \\ CL_s &= \frac{CL_{H_1}}{CL_{H_0}} \end{aligned} \tag{6}$$

CL_{H_0} measures agreement with the three-flavour hypothesis, and CL_{H_1} with the four-flavour hypothesis. The previous expressions are calculated for points throughout the $(\sin^2 2\theta_{14}, \Delta m^2_{41})$ parameter space for Daya Bay and Bugey-3, and $(\sin^2\theta_{24}, \Delta m^2_{41})$ for MINOS.

THE DAYA BAY EXPERIMENT

Daya Bay is a reactor antineutrino experiment which detects them trough inverse β decay $\bar{\nu}_e + p \rightarrow e^+ + n$ (IBD). Antineutrinos are produced by six reactor cores and measured in eight functionally identical liquid-scintillator detectors (ADs) [12]. The detectors are located in three underground experimental halls (EHs). The flux-averaged baselines for EH1, EH2 and EH3 are approximately 520, 570 and 1590 m, respectively. This allows Daya Bay to explore over three orders of magnitude of Δm^2_{41}. The layout of the experiment is shown in Fig.1. Near halls (EH1 and EH2) house two ADs each, while the far hall houses 4 ADs. More details about the IBD event selection, background estimates, and assessment of systematic uncertainties can be found in [12,14].

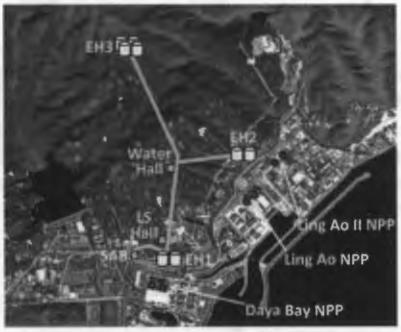

FIGURE 1. Layout of the Daya Bay experiment: The red dots near the ocean represent the reactor cores, and the white cylinders represent the antineutrino detectors located in the three different halls (EHs).

Daya Bay's latest search for sterile neutrino mixing used a dataset comprised of 621 days of data [13]. The analysis was performed with two independent and complemen-

tary methods: A Feldman-Cousins approach [15], and the confidence limit CL_s [7,8] approach explained before. The resulting exclusion contours are shown in Fig.2. where it can be seen that the two approaches give consistent results.

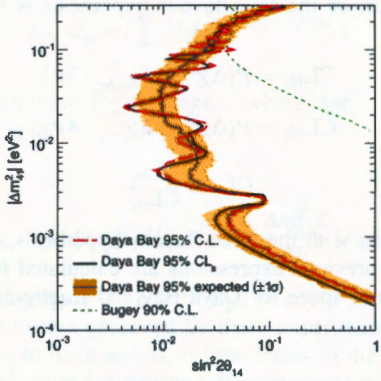

FIGURE 2. Exclusion contours in the $\sin^2(2\theta_{14})$ and Δm^2_{41} parameter space assuming the normal hierarchy. The red dashed line is the 95% exclusion contour using the Feldman-Cousins method [15] and the solid black line represents the exclusion contour using CL_s [7,8]. The reproduction of Bugey-3 results [6] at 90% confidence level are included as the green dashed-line.

THE BUGEY-3 EXPERIMENT

The Bugey-3 experiment was performed in the early 1990s. The experiment detected electron antineutrinos produced in two reactors with two ^{6}Li-doped liquid scintillator detectors at three different baselines (15, 40 and 95 m). Because Bugey-3 had shorter baselines compared to Daya Bay, the experiment was sensitive to a region with larger Δm^2_{41} values.

The original Bugey-3 analysis used the raster scan method detailed in Ref. [11]. To get the combination with the Daya Bay results, two changes were made to the original results: The IBD cross section was updated [16], and the Huber [17] and Mueller [18] model for the antineutrino flux was utilized. This ensures consistency with the prediction used by the Daya Bay experiment. The reproduced Bugey-3 contours are shown in Fig.3 alongside the results from Daya Bay.

THE MINOS EXPERIMENT

The MINOS experiment [19] was located at Fermilab in The United States. It used two functionally equivalent detectors separated by 734 km. These detectors sampled the NuMI neutrino beam [20], which yields neutrinos with an energy spectrum that peaks at about 3 GeV. The 1 kton Near Detector was located at Fermilab, and the 5.4 kton Far Detector is located at the Soudan Underground Laboratory [19]. Further details of the

NuMI beam and the detectors can be found in Ref. [20].

The experiment used the reconstructed energy spectrum of charged-current and neutral-current neutrino interactions to search for sterile neutrino mixing. With these two channels the MINOS experiment was able explore different ranges of Δm^2_{41} by searching for distortions or deviations from three-flavour oscillations. The Feldman-Cousins [15] and the CL_s [7,8] methods were used to obtain exclusion limits in the $(\sin^2\theta_{24}, \Delta m^2_{41})$ parameter space. These contours are shown in Fig.4.

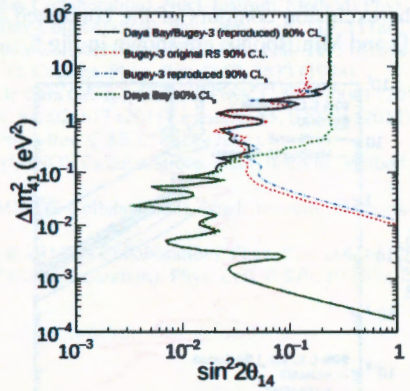

FIGURE 3. Excluded regions for the original Bugey-3 results obtained based on the raster scan method [11]. The reproduced Bugey-3 results are also shown, together with the Daya Bay results and their combination [6]. In all cases the region to the right is excluded at the 90% confidence.

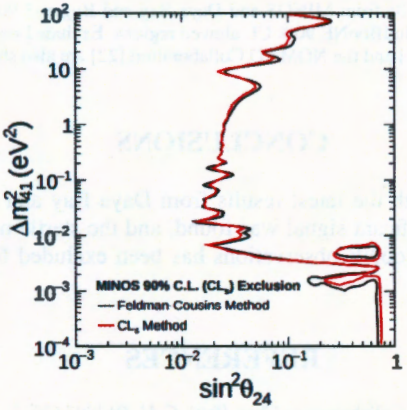

FIGURE 4. Comparison of the MINOS 90% CL contour using the Feldman-Cousins method and the CL_s method [6]. The region to the right is excluded at the 90% CL and 90% CL_s for the two methods respectively.

COMBINED ANALYSIS

The combined analysis was performed using the CL_s method. In the combined analysis $\Delta\chi^2$ as well as $\Delta\chi^2_{3\nu}$ and $\Delta\chi^2_{4\nu}$ were obtained for points in $(\sin^2 2\theta_{14}, \Delta m^2_{41})$ parameter space for Daya Bay and Bugey-3, and points in $(\sin^2\theta_{24}, \Delta m^2_{41})$ for MINOS. Combined pairs of points from MINOS and the Daya Bay and Bugey-3 results at fixed values of Δm^2_{41} allowed to obtain constrains on electron neutrino or antineutrino appearance due to oscillations into sterile neutrinos. Further details of the combination procedure can be found in Ref. [6]. The exclusion contours of the combined analysis as well as the allowed regions of LSND and MiniBooNE are shown in Fig.5.

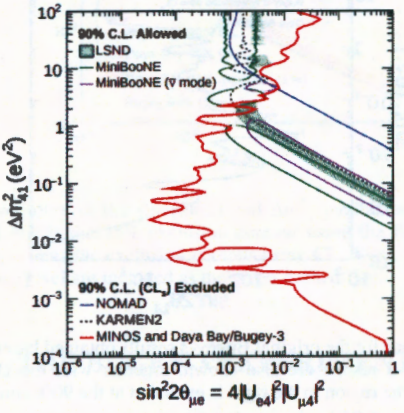

FIGURE 5. Combined results from MINOS and Daya Bay and Bugey-3 90% CL_s limit on $\sin^2 2\theta_{\mu e}$ compared to the LSND and MiniBooNE 90% CL alowed regions. Excluded regions at 90% CL from the KARMEN2 Collaboration [21] and the NOMAD Collaboration [22] are also shown.

CONCLUSIONS

A combined analysis with the latest results from Daya Bay and MINOS experiments was performed. No significant signal was found, and the sterile neutrino interpretation of the LSND and MiniBooNE observations has been excluded for $\Delta m^2_{41} < 0.8\text{eV}^2$ at 95% CL_s.

REFERENCES

1. F. P. An *et al.* (Daya Bay Collaboration) Chin. Phys. C **41**, 013002 (2017).
2. C. Guinti and M. Laveder. Phys, Rev. C **83**, 065504 (2011).
3. A. Aguilar *et al.* (LSND Collaboration) , Phys, Rev. D **64**, 112007 (2001).
4. A. Aguilar-Arevalo *et al.* (MiniBooNE Collaboration), Phys, Rev. Lett. **110**, 161801 (2013).

5. S.Schael *et al.* (ALEPH Collaboration, DELPHI Collaboration, L3 Collaboration, OPAL Collaboration, SLD Collaboration, LEP Electroweak Working Group, SLD Electroweak Group, SLD Heavy Flavour Group), Phys, Rep. **427**, 257 (2006).
6. P. Adamson (Fermilab) *et al.* (Daya Bay and MINOS Collaborations), Phys. Rev. Lett. **117**, 151801 (2016).
7. A. L. Read, J. Phys, G **28**, 2693 (2002).
8. T. Junk, Nucl. Instrum. Method Phys. Res. Sect. A **434**, 435 (1999).
9. F. P. An *et al.* (Daya Bay Collaboration), Phys. Rev. Lett. **117**, 151802 (2016).
10. P. Adamson *et al.* (MINOS Collaboration), Phys. Rev. Lett **117**, 151803 (2016).
11. B. Achkar *et al.* (Bugey-3 Collaboration), Nucl. Phys. B **434**, 503 (1995).
12. F. P. An *et al.* (Daya Bay Collaboration), Nucl. Instrum. Methods Phys. Res. Sect. A **811**, 133 (2016).
13. F. P. An *et al.* (Daya Bay Collaboration), Phys. Rev. Lett. **115**, 111802 (2015).
14. F. P. An *et al.* (Daya Bay Collaboration), Phys. Rev. Lett. **117**, 151802 (2016).
15. G. J. Feldman and R. D. Cousins, Phys. Rev. D **57**, 3873 (1998).
16. K. Olive *et al.* (Particle Data Group), Chinese Phys. C **38**, 090001 (2014).
17. P. Huber, Phys. Rev. C **84**, 024617 (2011), erratum: **85**, 029901 (2012).
18. T. A. Mueller *et al.*, Phys. Rev. C **83**, 054615 (2011).
19. D. G. Michael *et al.* (MINOS Collaboration), Nucl. Instrum. Methods Phys. Res. Sect. A **596**, 190 (2008).
20. P. Adamson *et al.* (MINOS Collaboration), Nucl. Instrum. Methods Phys. Res. Sect. A **806**, 279 (2016).
21. B. Armbruster *et al.* (KARMEN Collaboration), Phys. Rev. D **65**, 112001 (2002).
22. P. Astier *et al.* (NOMAD Collaboration), Phys. Lett. B **570**, 19 (2003).

Reactor antineutrinos in SNO+

Ştefan-Alexandru Nae[1,2] for the SNO+ collaboration

[1] *Laboratório de Instrumentação e Física Experimental de Partículas (LIP), Lisbon, Portugal*
[2] *Faculdade de Ciências (FCUL), Universidade de Lisboa, Lisbon, Portugal*

Abstract. The SNO+ liquid scintillator detector capability for a neutrino oscillations study using antineutrinos from nuclear reactors is outlined. The flux is dominated by three Canadian close-by nuclear power plants located ~250 km, Bruce, and ~350 km, Pickering and Darlington, away from the experimental site at SNOLAB. The expected energy spectrum for inverse beta decay events is generated with Monte Carlo techniques and the impact of the two sigma discrepancy between solar and reactor measurements of Δm^2_{21} on its shape is discussed. SNO+ will reach a sensitivity to Δm^2_{21} of 0.2×10^{-5} eV^2 after 7 years of data taking.

Keywords: neutrino oscillations, rector neutrinos, inverse beta decay, scintillation detector
PACS: 14.60.Pq, 13.15.+g, 29.40.Mc

INTRODUCTION

SNO+, a large-scale liquid scintillator (LS) experiment located 2 km underground at SNOLAB in Canada, targets a vast neutrino physics research programme [1]. The main goal of the collaboration is to search for the neutrino-less double beta decay ($0\nu\beta\beta$) of ^{130}Te, which, if detected, will support theories describing neutrinos as Majorana particles and will provide a definite constraint on the sum of the mass states contributions to the electron flavour neutrino state. The Δm^2_{21} neutrino oscillation parameter can be extracted from detection of antineutrinos originating at nuclear reactors. A separation between reactor antineutrinos and geo-neutrino signals will be attempted using both a Monte Carlo simulation of the expected event rates and directional information. Measurements of pep, CNO, and ^{8}B solar neutrinos are also possible. Detector operations are optimized to maximize its uptime for supernova events. Exotic physics like invisible nucleon decay are also part of its extensive physics program.

With an overburden of ~6000 meter water equivalent, the detector consists of a 12 meter diameter spherical acrylic vessel (AV) which will house different detection media across the lifespan of the experiment. Starting with 1000 tonnes of ultra pure water in the 9 months first phase, it will then use 780 tonnes of organic liquid scintillator (LAB + PPO) for the 6 months second phase, to finally use 780 tonnes of LS loaded with 3 tonnes of natural tellurium (1.3 tonnes of ^{130}Te) in the 5 year long third phase. Outside the AV, attached to a geodesic support structure, ~9300 photo-multiplier tubes (PMTs) with concentrators are pointed at the detection medium providing a coverage of ~55%. 1700 tonnes of water stand between the PMTs and the AV while outside the PMT support structure another 5300 tonnes of water provide extra shielding.

REACTOR ANTINEUTRINOS

Originating in the burning of nuclear fuel in the core of nuclear reactors ~60% of the reactor antineutrinos reaching the SNO+ detector are from three nuclear power plants in Canada, Bruce, Darlington, and Pickering, summing up to 18 cores from a total of ~450 cores worldwide. 99.9% of the energy produced in a reactor core is from the induced nuclear fission of ^{235}U, ^{239}Pu, and ^{241}Pu with thermal neutrons, and of ^{238}U with fast neutrons [2]. These reactions give ~6 electron type antineutrinos from the beta decays of the fission products. A 3000 MW reactor releases 1.9×10^{22} MeV per second as a result of these reactions with 5.5×10^{20} antineutrinos emitted isotropically every second. 250 km away from this reactor, the same distance as between the SNO+ detector and the nuclear power plant closest to it, Bruce, the flux will be of 7.2×10^4 antineutrinos per centimetre squared per second. The flux from the 8 Bruce cores contributes ~40% to the expected flux. The next closest reactors, Darlington and Pickering, are at a distance of ~350 km, are both in almost the same direction from the detector, and contribute ~20% to the flux. Almost all of the remaining contributions to the antineutrino flux, ~40% at SNO+ are from 32 nuclear power plants (32R), with a total of 50 cores, located no further than 1000 km away from the detector, in Canada and USA.

NEUTRINO OSCILLATIONS

Propagating away from a nuclear reactor the initial neutrino pure flavour state $|\nu_e\rangle = \sum_j U_{ej} |\nu_j\rangle$, $j = \overline{1,3}$, will undergo changes of the component mixed mass states phases as a function of the distance travelled and the carried energy leading to deformations of the energy spectrum when detecting neutrinos of the initial flavour as shown in Figure 1. The probability to detect a reactor antineutrinos in the same flavour state as they were produce, the survival probability, is given by

$$P_{\bar{\nu}_e \to \bar{\nu}_e}(L, E_{\bar{\nu}_e}) = cos^4\theta_{13}\left[1 - sin^2(2\theta_{12})\, sin^2\left(1.27\frac{\Delta m^2_{21} \cdot L}{E_{\bar{\nu}_e}}\right)\right] + sin^4\theta_{13} \qquad (1)$$

where L is the travelled distance in [km], $E_{\bar{\nu}_e}$ is the antineutrino energy in [MeV] at the production point, while θ_{12}, θ_{13} are measured parameters of the Pontecorvo-Maki-Nakagawa-Sakata (PMNS) mixing matrix, and Δm^2_{21} is the squared mass difference of the 2 and 1 neutrino mass states, a quantity emerging in the calculation of oscillation probabilities. The neutrino oscillation model was proposed and developed in 1957 and 1962 and confirmed with measurements of atmospheric neutrinos by the Super-Kamiokande collaboration in 1998 [6] and of solar neutrinos by the Sudbury Neutrino Observatory collaboration in 2001 and 2002 [7].

The stacked contributions to the energy spectrum shown in Figure 1, using the 2016 global fit oscillation parameters from PDG [3], confirm the main weighted contributions come from the closest reactors followed by the next closest 32 reactor complexes which contribute with local extrema, minima and maxima, to the energy spectrum thus amplifying its features. For the same groups of reactors, summing up to the total number of commercial reactors worldwide, the oscillation probability is computed replacing the

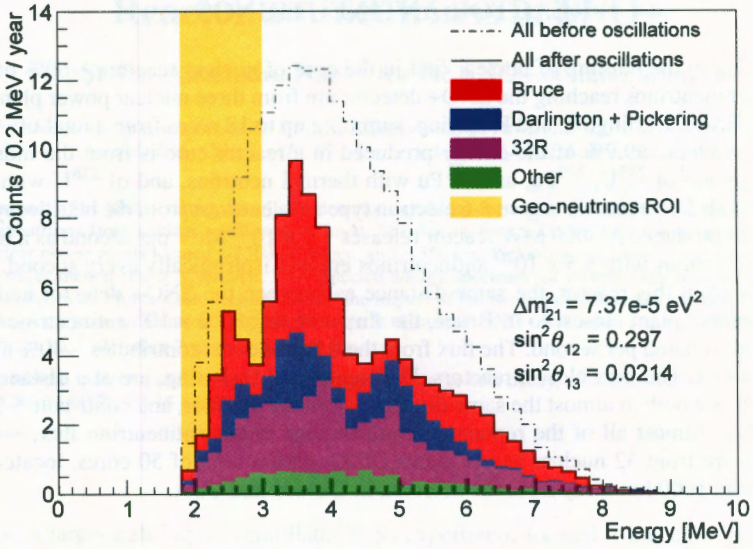

FIGURE 1. Monte Carlo simulation of the contributions from all reactors in the world to the expected reactor antineutrino energy spectrum at SNO+ using a 3 flavour oscillation formula with the PDG 2016 neutrino oscillation parameters values. Stacked contributions of the main components to the spectrum are highlighted.

Δm^2_{21} value with the most recent Super-Kamiokande result [4] and the result is shown in Figure 2. While the PDG fit value for Δm^2_{21} reflects the KamLAND measurement [8], due to its smaller uncertainty, thus weighting more the contribution to its value from a *reactor* measurement, the Super-Kamiokande result is from a *solar* measurement [4]. With the 2 σ tension between the two measurements, additional independent information will help clarify the apparent disagreement.

The energy spectra from Figures 1 and 2 are modelled starting from fractions of fissile isotopes in the nuclear fuel, varying with nuclear reactor type (pressurized heavy water reactors - PHWR, boiling water reactors - BWR, etc.), weighting parametrizations for each isotopes antineutrino energy spectrum which then are scaled by reactor thermal powers provided by International Atomic Energy Agency (IAEA) through the Power Reactor Information System (PRIS) [9]. Changes in the relative fraction of fissile nuclei during fuel burn-up will have a negligible impact on the time evolution of the energy spectrum. The constant refuelling of the CANDU [10] type Canadian reactors translates into a time independent flux expectation. Any maintenance work that impacts energy production can be monitored and accounted for using the hourly energy outputs provided by the Independent Electricity System Operator (IESO) [11] in Canada, for Canadian reactors, an with the PRIS service for all commercial reactors in the world. Seasonal

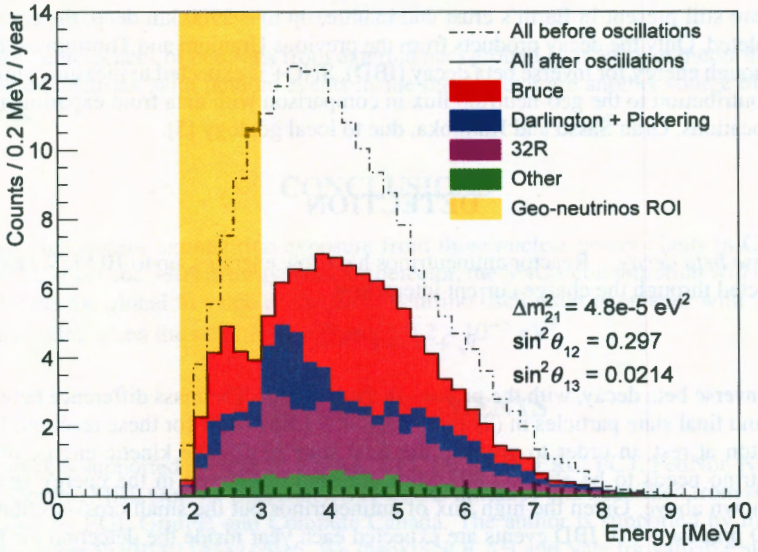

FIGURE 2. Same as Figure 1 but with the value for Δm^2_{21} from [4].

variations in the energy production due to temperature dependent energy conversion efficiency and consumer demand constitute less than 1% effect on the expected number of events. Cooling pools for spent nuclear fuel, located close to the reactor, were not accounted for in the simulation but the effect is expected to be below 1%.

Δm^2_{21} sensitivity. After 7 years of data taking, SNO+ will reach a sensitivity to Δm^2_{21} of 0.2×10^{-5} eV^2 considering 300 PMT-hits per MeV in scintillator (a quantity reflecting the light collection given the PMT coverage and scintillator optical properties), a 5.5 m fiducial volume (the radius of the volume at the centre of the AV optimized by the expected signal to noise ratio for the specific antineutrino analysis), and events above 3 MeV. Below this energy cut geo-neutrino events will also be detected, as shown in Figures 1 and 2. Successful separation of events between the two antineutrino sources based on the different expected energy spectra and rates in that region will improve the sensitivity to Δm^2_{21} and provide a geo-neutrino measurement, the first at SNOLAB and third worldwide. A successful attempt in separating for the first time the geo-neutrinos and reactor contributions based on directional information will further improve the result.

Geo-neutrinos. From inside the Earth, the decays of the naturally occurring radioactive elements ^{238}U, ^{232}Th, and ^{40}K constitute the main sources of geo-neutrinos. These

nuclei are still present in Earth's crust and mantle, up to ~2900 km deep, the core being depleted. Only the decay products from the previous Uranium and Thorium isotopes have enough energy for inverse beta decay (IBD). SNO+ is expected to measure a higher crust contribution to the geo-neutrino flux in comparison with data from experiments at other locations, Gran Sasso and Kamioka, due to local geology [5].

DETECTION

Inverse beta decay. Reactor antineutrinos have low energies, up to 10 MeV, and can be detected through the charge current interaction

$$\bar{\nu}_e + p \rightarrow e^+ + n, \tag{2}$$

called inverse beta decay, with the protons in the medium. The mass difference between initial and final state particles in (2) gives a $Q_0 = -1.802$ MeV for these reaction. With the proton at rest, in order to produce the final state in (2), the kinetic energy of the antineutrino needs to be above 1.802 MeV, threshold observed in the energy spectra plots shown above. Given the high flux of antineutrinos but the small cross-section for the IBD process ~110 IBD events are expected each year inside the detection medium irrespective of the experimental phase due to the similar number of Hydrogen atoms present in the different media. Due to an increased light yield in the scintillator phases, in comparison with the water phase, resulting in lower detector energy thresholds, the fraction of events detected from the expected IBD interactions will be higher in these phases allowing the Δm^2_{21} measurement.

Delayed coincidence

Signals. The final state particles in the IBD process give a definite signature inside the detector, the associated events are separated by ~ 200 μs and ~ 30 cm. The first one, the prompt event, comes a few nanoseconds after the interaction from the positron ionizing energy loss and ends in an electron-positron annihilation. The second one, the delayed event, is produced hundreds of microseconds after the interaction from the neutron capture, usually after thermalization, on Hydrogen nuclei, when the resulting Deuterium de-excites to ground state through the emission of a 2.2 MeV gamma ray. The reconstructed energy of the interacting antineutrino is directly given by the energy of the prompt event shifted with a constant,

$$E_{\bar{\nu}_e} = E_{prompt} + (M_n - M_p) - m_e = E_{prompt} + 0.8 \text{ MeV}. \tag{3}$$

Backgrounds. Alpha particles from the decay of ^{210}Po, from leaching inside the detection medium from the AV, will give a similar prompt-delayed coincidence in reaction with ^{13}C inside the detector (4). This is the main background and it will be mitigated by recirculation of the detection medium and through pulse shape discrimination using the sensitivity to the difference between the energy losses of alphas and positrons.

$$\alpha + {}^{13}C \rightarrow {}^{16}O + n \quad (4)$$

Fake coincidences of neutrons from external background sources, like muon-induced spallation neutrons, with random events inside the detector are another source of backgrounds.

CONCLUSIONS

With a high reactor antineutrino exposure from three nuclear power plants in Canada, located 250 km and 350 km away from the detector, the SNO+ collaboration will be able to improve the global fit value of the Δm^2_{21} neutrino oscillation parameter with 7 years of data taking when the sensitivity will reach 0.2×10^{-5} eV^2.

ACKNOWLEDGMENTS

This work is supported by ASRIP, CIFAR, CFI, DF, DOE, ERC, FCT, FedNor, NSERC, NSF, Ontario MRI, Queens University, STFC, UC Berkeley and benefitted from services provided by EGI, GridPP, and Compute Canada. The author is supported by the FCT grant number PD/BD/114381/2016. We thank SNOLAB and Vale for valuable support.

REFERENCES

1. S. Andringa et al. (SNO+ collaboration), *Adv. High Energy Phys.* **2016**, 6194250 (2016).
2. A. C. Hayes, and P. Vogel, *Ann. Rev. Nucl. Part. Sci.* **66**, 219-244 (2016).
3. C. Patrignani et al. (Particle Data Group), *Chin. Phys. C*, **40**, 100001 (2016).
4. K. Abe et al. (Super-Kamiokande collaboration), *Phys. Rev. D* **94**, 052010 (2016).
5. M. Baldoncini et al., *J. Phys. Conf. Ser.* **718**, 062003 (2016).
6. T. Kajita, E. Kearns, and M. Shiozawa, *Nucl. Phys. B* **908**, 14-29, (2016).
7. A. Bellerive et al., *Nucl. Phys. B* **908**, 30-51, (2016).
8. M.P. Decowski, *Nucl. Phys. B* **908**, 52 - 61, (2016).
9. Power Reactor Information System (PRIS), *iaea.org*, (2016).
10. Canadian nuclear association (CNA), *cna.ca*, (2017).
11. Independent Electricity System Operator (IESO), *ieso.ca*, (2016).

Measurement of the neutrino mixing angle θ_{13} with the Double Chooz experiment

Diana Navas Nicolás on behalf of the Double Chooz collaboration

Centro de Investigaciones Energéticas, Medioambientales y Tecnológicas CIEMAT,28040, Madrid, Spain

Abstract. The Double Chooz experiment aims for a precise and accurate determination of the neutrino mixing angle θ_{13} through the disappearance of the electron antineutrinos $\bar{\nu}_e$ coming from the two PWR reactors of the Chooz nuclear plant. These antineutrinos interact with the liquid scintillator of the Double Chooz detectors and can be detected through the inverse beta decay reaction (IBD). A novel analysis that allows to increase statistics by almost a factor 3 has been developed, improving the measurement of θ_{13}.

Keywords: neutrino mixing angle, reactor experiments, inverse beta decay IBD
PACS: 14.60.Lm; 14.60.St; 14.60.Pq

INTRODUCTION

The main goal of the Double Chooz experiment is to provide a precise and robust measurement of the θ_{13} neutrino mixing angle. This angle, the smallest of the three known mixing angles, can be determined from the disappearance of the $\bar{\nu}_e$ (eq. 1):

$$P_{\bar{\nu}_e \to \bar{\nu}_e} = 1 - sin^2(2\theta_{13}) sin^2 \frac{1.27 \Delta m^2_{13} L[m]}{E_{\bar{\nu}_e}[MeV]} \quad (1)$$

The antineutrinos emitted by the nuclear reactors interact with the protons present in the detector liquid scintillator through the inverse β decay: $\bar{\nu}_e + p \to e^+ + n$, producing the spatial and temporal coincidence of two signals that allows an efficient suppression of the backgrounds. The positron will lose its kinetic energy and will be annihilated fastly, being observed as the prompt signal. Measuring the e^+ energy, the neutrino energy can be obtained. The energy threshold of this reaction is 1.8 MeV. The delayed signal corresponds to the neutron capture either by a Gadolinium (Gd) nucleus after 30 μs emitting gammas of 8 MeV or by a Hydrogen (H) nucleus after 200 μs, emitting gammas of 2.2 MeV, providing two independent samples.

THE DOUBLE CHOOZ DETECTORS

Nuclear reactors are a very intense and pure source of electron antineutrinos suitable to study the properties of these evasive particles. A new generation of nuclear reactor experiments, Double Chooz (DC) [1], Daya Bay [2] and Reno [3] have been able to determine θ_{13}. The key of these experiments falls on the comparison of the observed $\bar{\nu}_e$ between a near and a far detector, providing an accurate measurement of the mixing

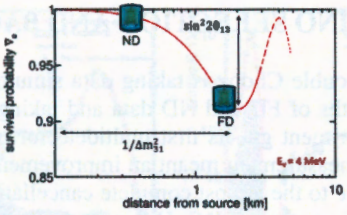

FIGURE 1. Survival probability for 4 MeV $\bar{\nu}_e$.

angle without needing to use predictions of the reactor flux. The DC near detector (ND), operational since December 2014, is located around 400 meters far from the reactors and measures the $\bar{\nu}_e$ rate before the oscillation takes place. On its side, the far detector (FD), around 1050 meters away from reactors and operating since April 2011, is placed closed to the oscillation maximum and is able to detect the $\bar{\nu}_e$ disappearance (figure 1).

The design of the two DC detectors is almost identical (figure 2). The neutrinos are detected by their collision with the protons present in the ν-target (NT), which is filled with liquid scintillator doped with Gd. The incident neutrino energy is extracted from the positron deposited energy in the target. The NT is surrounded by another cylinder full of liquid scintillator without any Gd, called γ-catcher (GC), that collects the γs that can escape from the NT. In the inner face of the next volume, known as buffer (BF), 390 photomultipliers (PMT) that detect the scintillation light are fixed. The BF contains also non-scintillating mineral oil that isolates the other two scintillating volumes from the PMTs radioactivity. These three regions, optically separated from the rest of the detector, constitute what it is known as the inner detector volume (ID). The most external layer, called inner veto (IV), is filled up with liquid scintillator and is equipped with 72 PMTs that allow to detect the muons (μ) that pass through or near the detector. Moreover a shield made of steel (FD) or water (ND) covers the full detector volume. Finally, the outer veto (OV), made by scintillating strips, hides the upper part of the detector and tags the muon traces.

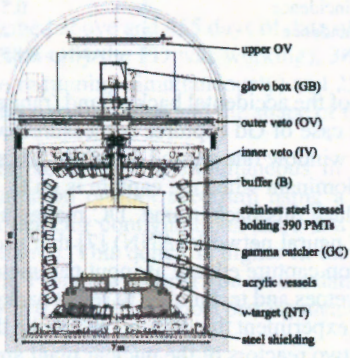

FIGURE 2. Schematic view of the DC detector.

ANTINEUTRINO SELECTION AND BACKGROUNDS

Since December 2014, Double Chooz is taking data simultaneously with the two detectors. Analysing 9 months of FD and ND data and taking into account the neutrino captures on Gd, the experiment got its first multidetector measurement: $sin^2(2\theta_{13}) = 0.111 \pm 0.018$ [4]. This measurement meant an improvement from previous results [5] obtained with only FD due to the almost complete cancellation of the error uncertainty thanks to the isoflux configuration of DC. However the statistical uncertainty was still limiting the sensitivity of this data sample.

To solve this, DC has developed a new analysis (called Gd+H) in which either Gd or H neutron captures are considered in the whole detector volume (NT+GC), increasing this way the statistics by almost a factor of 3 (the neutrino rate in the near (far) detector is increasing to about 900 (140) events/day). The signal to background ratio in both detectors is still well above 10 with the new selection.

The procedure to select the signals is the following. First of all, a preselection is made to identify the $\bar{\nu}_e$. The preselection requires that the trigger must be totally efficient (E_{vis}>0.4 MeV), eliminates the tagged muons and the subsequent events using the IV and OV information and rejects also light noise (LN) signals produced by the light emission of the PMTs basis [6].

From the preselected sample, the $\bar{\nu}_e$ are identified as pairs of signals closed in time and space. The energy range of the prompt signal e^+ takes into account the energy spectrum of the incident neutrino, which is expected to finish at 8.5 MeV but this window is opened up to 20 MeV to constraint background events of cosmogenic isotopes, fast neutrons and stopping muons. The energy range of the second signal is chosen considering the possible energies of the neutron capture on Gd or H. The variables used are listed in the table 1:

TABLE 1. Antineutrino selection cuts used in Gd+H analysis.

Variable	Values for Gd+H
Multiplicity (without extra signals on this period)	[-800,900] μs taking fast signal as reference
Prompt signal energy	$0.5 < E_{vis} < 20$ MeV
Delayed signal energy	$1.3 < E_{vis} < 10$ MeV
Temporal coincidence	$0.5 < \Delta T < 800$ μs
Spatial coincidence	$\Delta R < 1200$ cm
ANN	ANN > 0.85 (FD), ANN > 0.86 (ND)

The small contribution of the accidental background (random coincidences of two uncorrelated triggers) in the case of Gd captures is measured with high precision moving the temporal coincidence window one second from the fast signal. However the contribution of these events is dominant when the capture is on H, where the average delayed signal is 2.2 MeV. To reduce this background, DC makes use of a multivariable analysis based on an artificial neural network (ANN) [7] that uses the spatial and temporal coincidence and the neutron capture energy as input parameters (fig. 3).

Besides all these cuts, vetoes and techniques to reject backgrounds, there is one of the unique features in the DC experiment that falls back into the the possibility of measuring the background when the two reactors of the nuclear plant are off. So far there were two of these reactor off periods during the time in which only the FD was taking data [8]. This

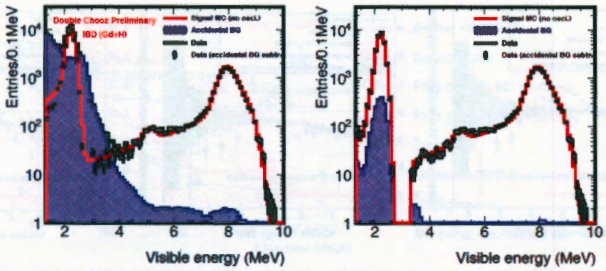

FIGURE 3. Energy of the neutron capture on H and Gd before (left) and after (right) the ANN selection is applied. Accidentals are present in purple, black line shows the data sample and red line shows MC distribution which is in perfect agreement with data once the accidental subtraction is done (black dots).

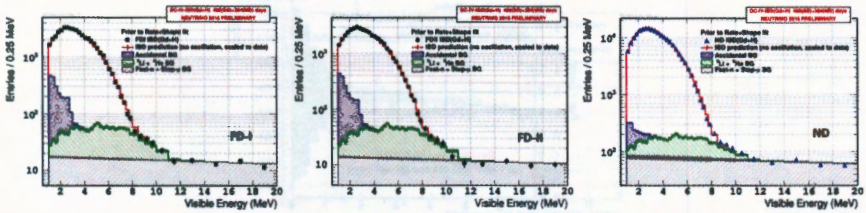

FIGURE 4. Observed IBD visible energy spectrum (black points) superimposed to the $\bar{\nu}_e$ non-oscillation prediction (red line) with the backgrounds added: fast neutrons and stopping muons (grey), ^{9}Li and ^{8}He (green) and accidental coincidences (purple) for FD-I, FD-II and ND.

measurement is used to constrain the total background rate in the oscillation analyses.

OSCILLATION RESULTS

Using Gd+H analysis described above and 455 days of data of FD-I (nomenclature used to refer to the period in which only the FD was working), 363 days of FD-II (phase in which FD as well as ND were running simultaneously) and 258 days of ND, DC is able to obtain the neutrino and backgrounds rate and the shape of the energy spectrum as can be seen in figure 4.

The θ_{13} parameter is extracted from a simultaneous fit of the data taken by the detectors and the non oscillation prompt spectrum using a MC simulation. One can see in figure 5 that for all detector configurations there is a deficit at low energy that is induced by the θ_{13} oscillation. This deficit is higher in the far detector as it is closer to the oscillation maximum. From the comparison of the data to the MC, DC obtains a value of $sin^2(2\theta_{13}) = 0.119 \pm 0.016$ [9], the most precise measurement of the experiment to date.

In figure 5, it can be also observed that there is a distortion between the prediction

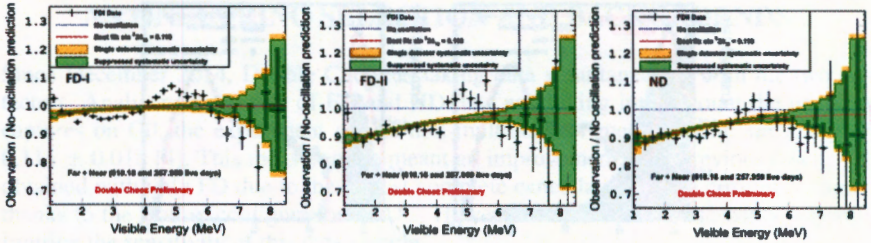

FIGURE 5. Ratio of the prompt spectrum to the expected non oscillation prompt spectrum as a function of the visible energy for each detector (ND, FD-I and FD-II). Red line shows the best fit value. Systematic uncertainties are also plotted.

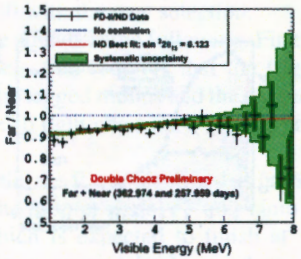

FIGURE 6. Ratio of the observed energy spectrum from FD-II to ND data. The red line shows the best-fit value. Systematics uncertainties are also plotted.

and the data that can not be explain by θ_{13} around 5 MeV. This spectral distortion is observed by all reactor antineutrino experiments [10] and it is under study. In order to cross check the previous θ_{13} result, another fit is performed comparing directly the data of FD-II to the data of ND. Figure 6 shows the ratio of FD-II to ND being the best fit value: $sin^2(2\theta_{13}) = 0.123 \pm 0.023$, in good agreement with the data to MC fit within uncertainties.

PROSPECTS AND CONCLUSIONS

The most precise Double Chooz results of θ_{13} using two detectors with a novel analysis (Gd+H) is presented. The data to prediction fit results in $sin^2(2\theta_{13}) = 0.119 \pm 0.016$.

Systematic uncertainty evolution of Double Chooz is shown in Figure 7. The reactor flux was the dominant uncertainty before ND data was included, while it is strongly suppressed in the recent results. Current largest systematic uncertainty is now the detection uncertainty, which comes from the proton number uncertainty in GC. This uncertainty will be suppressed by the direct measurement at the detector dismantling. Figure 8 shows the evolution of the sensitivity as a function of data taking time in case the measurement of the proton number in GC can be improved to get a similar knowledge to the one in

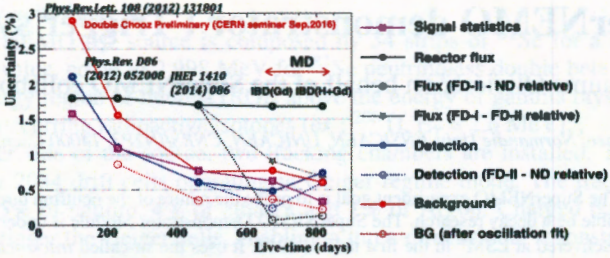

FIGURE 7. Systematic uncertainty evolution during the different analyses developed by DC. MD refers to the two θ_{13} measurements done with the two DC detectors and the last column of points reflects the systematic uncertainties for the Gd+H analysis.

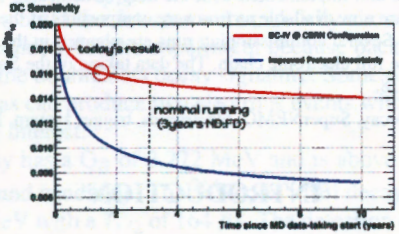

FIGURE 8. Double Chooz $sin^2(2\theta_{13})$ sensitivity evolution including the prospect for an improved proton number estimation.

the NT. A total uncertainty on $sin^2(2\theta_{13})$ below 0.01 could be achieved.

DC data taking will go on until the end of 2017, so the experiment will show new accurate measurements in the near future. Moreover the new DC data with the near detector will also allow more detailed studies of the neutrino spectrum and might help to find the explanation of the data-MC 5 MeV distortion.

REFERENCES

1. Y. Abe et al. (Double Chooz Collaboration), *Phys.Rev.Lett.* **108**, 131801 (2012).
2. F.P. An et al. (Daya Bay Collaboration), *Phys.Rev.Lett.* **108**, 171803 (2012).
3. J.K. Ahn et al. (RENO Collaboration), *Phys.Rev.Lett.* **108**, 191802 (2012).
4. 51st Rencontres de Moriond EW (2016) *https://indico.in2p3.fr/event/12279/*
5. Y. Abe et al. (Double Chooz Collaboration), *Phys. Lett. B* **735**, 51 (2014).
6. Y. Abe et al. (Double Chooz Collaboration), *JINST* **11**, P08001 (2016).
7. Y. Abe et al. (Double Chooz Collaboration), *JHEP* **01**, 163 (2016).
8. Y. Abe et al. (Double Chooz Collaboration), *Phys.Rev. D* **87**, 011102(R) (2013).
9. A. Cabrera, *Double Chooz Improved Multi-Detector Measurements*, EP Seminar, Cern, (2016).
10. F. P. An et al. (Daya Bay Collaboration) *Phys. Rev. Lett.* **116** no.6, 061801 (2016). Erratum: [*Phys. Rev. Lett.* **118** no.9, 099902 (2017)]; S. H. Seo et al. (RENO Collaboration), arXiv:1610.04326 [hep-ex]; Y. J. Ko et al., *Phys. Rev. Lett.* **118** no.12, 121802 (2017).

SuperNEMO demonstrator : Trigger system

Guillaume Oliviéro[2] on behalf of the SuperNEMO collaboration

LPC Caen[3], Normandie Univ, ENSICAEN, UNICAEN, CNRS/IN2P3, 14000 Caen, France

Abstract. The SuperNEMO experiment goal is to probe the nature of the neutrino through the neutrinoless double beta decay research. The SuperNEMO Demonstrator Module is under construction and will be delivered at LSM[1] in the first half of 2018. It uses the so-called *tracko-calo* technique which allows not only to measure the energy of particle traversing the detector but also to reconstruct their track, time of flight and full kinematic. An important work on the radiopurity has been done in order to make SuperNEMO a background free experiment in the $\beta\beta0\nu$ decay channel. The trigger system, developed at LPC Caen and LAL, aims to maximize the data acquisition efficiency for $\beta\beta$ and background events of interest as well as to reduce the spurious event trigger rate. Some algorithms have been designed and implemented with the help of dedicated Monte-Carlo simulations and hardware tests. They are now available as firmware components of the detector's front-end and trigger electronics boards. Several commissioning runs are planned in the coming months in order to test the robustness of the full electronic chain. The data taking of the SuperNEMO demonstrator should start in summer 2018.

Keywords: double beta decay, SuperNEMO, electronics, trigger system, Monte-Carlo simulations

INTRODUCTION

The SuperNEMO Demonstrator Module uses about 7 kg of ^{82}Se to probe the Dirac or Majorana nature of the neutrino through the search of the $\beta\beta0\nu$ decay. The aim of the experiment's phase I is to reach a sensitivity of $T_{1/2}^{\beta\beta0\nu} > 6.10^{24}$ years for the $\beta\beta0\nu$ mass mechanism for ^{82}Se. This expected performance can be interpreted in term of an upper limit on the effective neutrino mass $m_{\beta\beta} < [200\text{-}550]$ meV. The SuperNEMO demonstrator is installed in the Modane underground laboratory. The detector uses the same tracko-calo technique as in its predecessor : the NEMO-3 detector. It couples a tracker (drift chamber in Geiger mode) with a calorimeter (scintillator + photomultiplier tubes) [1]. Thanks to this technique, e^-, e^+, γ, α, and μ particles can be identified and measured.

SUPERNEMO DEMONSTRATOR

The SuperNEMO demonstrator has a planar geometry of $6\times4\times2$ m^3. The experimental principle of the tracko-calo technique and an overview of the SuperNEMO demonstrator

[2] E-mail: goliviero@lpccaen.in2p3.fr

[3] Laboratoire de Physique Corpusculaire

[1] Laboratoire Souterrain de Modane

design is shown in figure 1.

The SuperNEMO $\beta\beta$ source is composed by 34 strips of ^{82}Se for a total mass of 7 kg. The Q value, equal to 2.998 MeV for ^{82}Se neutrinoless double beta decay would place the energy region of interest (ROI) above the energy of gamma rays from almost all naturally occurring radioactive isotopes (ex : ^{208}Tl, $E_\gamma = 2.6$ MeV).

From either side of the source, two tracking chambers are installed. The tracker is composed by 2034 drift cells operating in Geiger regime mode. The tracking gas is a mixture of 95% of helium, 4% of ethanol and 1% of Argon. Charged particles ionize the gas and trigger the Geiger cells, enabling a three-dimensional reconstruction of the particle tracks.

The calorimeter encloses the tracking volume. It is mainly composed by vertical walls for a total of 712 optical modules (OM). An optical module consists in the assembly of a plastic scintillator block and a low radioactivity photomultiplier tube (8" or 5" PMT). The energy resolution is 4% at $Q_{\beta\beta}$ (FWHM) [2].

The materials used to build the detector were carefully chosen with respect to radiopurity. This is a major concern for the experiment because backgrounds from natural radioactivity can mimic the double beta decay signature. Some physical processes involving electrons or gammas can produce two electrons events with a significant probability in the energy region of interest.

The ^{214}Bi beta decay has a Q_β of 3.272 MeV and is above the $Q_{\beta\beta}$ of ^{82}Se. This is a thus critical background candidate. The ^{214}Po, as ^{214}Bi decay product, decays with an alpha particle of 7.8 MeV with a $T_{1/2}$ of 164 μs. The detection of these BiPo radioactive cascades (BiPo) is possible if the detector is equipped with a proper trigger strategy. A well designed trigger system is crucial to identify, locate and measure some possible ^{214}Bi contamination of the experimental setup.

Individual detectors can also self-trigger because of their intrinsic noise. Typical single rate for a SuperNEMO tracker drift cell is about 0.2 Hz. For a calorimeter optical module, using a threshold of 15 mV (equivalent to 50 keV electron) the single rate is close to 10 Hz. Pathological instabilities of individual detection units can also increase the rate of spurious events.

The detector owns 2034 Geiger cells and 712 optical modules. The data acquisition system is not able to support a too high trigger rate without enduring a huge dead time. This is the reason why it is needed to implement tools to make smart decisions and optimize the response of the detector readout. This is the role of the trigger system.

SUPERNEMO TRIGGER STRATEGY

The design of the SuperNEMO trigger system implies the centralization of primary digitized data from the 2034 Geiger cells and 712 PMTs to take a global decision and initiate the data readout. The detection units (tracker cells and calorimeter OMs) are connected to 109 multichannel front-end boards (tracker : 57, calorimeter : 52) which retrieve the input analog signals. Using specific thresholds, trigger primitives signals are built and transmitted to six control boards, one per electronics crate, using a dedicated connection. The control boards then partially merge and reduce the amount of trigger primitives and send them to an unique trigger board through high bandwith links. The

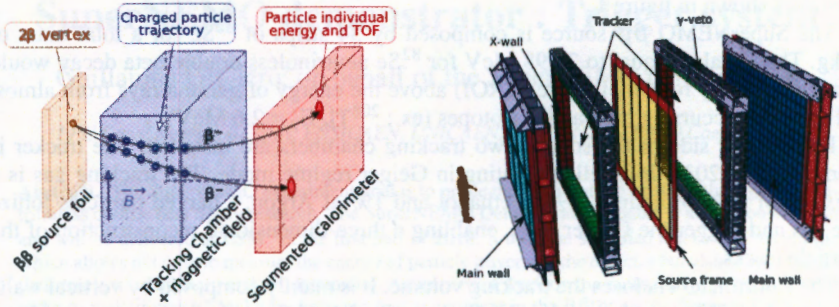

FIGURE 1. *Left :* Tracko-calo NEMO technique. *Right :* Overview of the SuperNEMO demonstrator.

trigger board uses embedded algorithms with various sets of criteria and policies and build a decision in order to engage the data readout. The central trigger clock uses a 1600 ns time tick. Given a typical event of interest ($\beta\beta$ decay or background decay), the trigger is able to make a decision within 10 microseconds.

Trigger design

Trigger algorithms are developed in *C++* using the SuperNEMO software framework for simulation and data analysis : *Bayeux* and *Falaise* [3]. The goal is to emulate the dynamic behaviour of the electronics in a realistic way in order to modelize the digital response of various boards and circuits in terms of trigger primitives production and final trigger decision. The algorithms have been designed in such a way it is possible to implement them as firmware components in FPGA circuits, taking into account hardware constraints and limitations. On the other hand, the software version of the algorithm can be integrated in the standard simulation tool uses by the SuperNEMO collaboration.

After the collection of the trigger primitives, three algorithms are available in the trigger board. The first one, called CARACO (CAlo tRAcker COincidence) tries to associate calorimeter and tracker hits using time and space coincidence criteria in order to identify well-shaped tracks from charged particles (electrons, positrons...). This first stage reject a large fraction of spurious events in the detector, corresponding to no event of physics interest. The main difficulty is to synchronized tracker hits with calorimeter hits in the same time scale. For an event of interest (an electron crossing the tracking volume and ending in a scintillator block), the typical time scale for calorimeter hits is below 100 ns whereas tracker anodic signals from Geiger cells occur in a 5 μs window. Cathodic signals are expected up to 70 μs. At the trigger board level, it is needed to take into account this various time scales to enable coincidence between calorimeter and tracker trigger primitives. Spatial association has also to be done to reduce fortuitous events. This implies the division of the detector geometry into several zones where

spatial coincidences are searched for collection of calorimeter and tracker hits.

The two other algorithms were designed for delayed alpha research due to the BiPo cascade which is a critical background for the SuperNEMO experiment. The approach of these algorithms is first to store in a dedicated memory buffer the signature of a CARACO event which has a signature compatible with ^{214}Bi beta decay, then to associate this signature with some isolated tracker hits produced by an alpha particle in the chamber near the first vertex. The association is performed in space using the typical length of the expected alpha track (< 40 cm) and in time up to 1 ms ($6 \times T_{1/2}(^{214}\text{Po})$). No calorimeter hit is required to identify an alpha particle in the detector. The APE (Alpha Previous Event) algorithm searches for a delayed alpha track as a cluster of Geiger cells while the DAVE (Delayed Alpha Veto Event) algorithm is able to detect only 1 or 2 cells close to the source foil after a CARACO event identified in the same location of the detector. These techniques make possible the detection of BiPo cascade background events with a good efficiency.

Implementation and tests

These algorithms have been implemented both in SuperNEMO official software framework and detector's front-end electronics. For the software version, the dedicated *Digitization module* is available in the SuperNEMO Falaise library. It emulates trigger primitives flowing from front-end boards to trigger board. The choice of the final trigger strategy was made from the results of simulation studies using realistic physics inputs and detector response. The firmware components have been implemented at LAL using the Verilog language on Altera Cyclone FPGA circuits.

Large sets of simulated events were produced thanks to the Falaise simulation software, based on the Geant4 framework. The *Digitization module* processes these events and computes the associated expected trigger output. The simulated events are also provided as mock input to the firmware version of the algorithm. Comparisons between the software and the firmware version of the trigger implementation were done in various cases of interest ($\beta\beta$ event, ^{214}Bi backgrounds, models of noisy hits).

RESULTS

Using the simulation framework, the efficiency of the trigger algorithm has been estimated and results are presented in table 1. For the different tests, Monte-Carlo events for several isotopes of interest are used as inputs. Using the CARACO algorithm, the readout efficiency for the $0\nu\beta\beta$ process is found to be very high. It is also very efficient to measure internal contamination of the source foil by ^{214}Bi or ^{208}Tl. It means that the SuperNEMO detector will be able to reach a good sensitivity while measuring its own radiopurity. As mentioned before, the detection of delayed alpha from the BiPo cascade is crucial to identify a possible ^{214}Bi contamination of the experimental setup. The APE and DAVE algorithms show good performance in the detection and identification of single alpha tracks. This will improve the rejection of background events which mimic the $0\nu\beta\beta$ signal. The results obtained in this work, base on realistic simulations, suggest

that the performances of the current design of the SuperNEMO trigger system are better than in the precedent detector : NEMO-3. However, several commissioning phases are needed with the real detector to validate these results and investigate new use cases.

TABLE 1. Trigger efficiency to different Monte-Carlo events. Several physical process of interest and vertex position were simulated.

Physical process	Vertex position	CARACO trigger efficiency (prompt e^-)	APE or DAVE trigger efficiency (delayed α)
$^{82}Se(\beta\beta 0\nu)$	source volume	$98{,}6 \pm 0{,}3$	-
$^{82}Se(\beta\beta 2\nu)$	source volume	$97.2 \pm 0{,}3$	-
^{208}Tl	source volume	$83{,}9 \pm 0{,}3$	-
^{214}Bi-^{214}Po	source surface	$75.8 \pm 0{,}2$	$97.7 \pm 0{,}1$
^{214}Bi-^{214}Po	field wire surface	$74.5 \pm 0{,}2$	$80.6 \pm 0{,}1$

CONCLUSIONS AND PERSPECTIVES

The trigger system is a central point of the readout system of the SuperNEMO demonstrator module. The main concern is to maximize the collection of physics event of interest ($\beta\beta$ decays, background events of interest) and to reject effectively spurious coincidences in order to not overload the data acquisition. Based on a constrained and realistic simulation, the results obtained in this work have permitted to design and implement different trigger algorithms now used in the trigger board firmware and the software framework. Several commissioning phases in year 2018 are planned to test the trigger system robustness in real running conditions.

ACKNOWLEDGMENTS

The author thanks the staff of the Modane Underground Laboratory for its technical assistance in building and operating the SuperNEMO detector. The SuperNEMO collaboration acknowledges the support by the funding agencies : CNRS/IN2P3 in France, Czech Republic, RFBR in Russia, STFC in U.K. and NSF in U.S.

REFERENCES

1. R.Arnold et al., *Probing New Physics Models of Neutrinoless Double Beta Decay with SuperNEMO, Eur. Phys. J. C* **80** , 927 (2010).
2. A.S.Barabash et al., *Calorimeter development for the SuperNEMO double beta decay experiment, Nucl.Instrum.Meth. A* **868**, 98-108 (2017).
3. F.Mauger, *The Bayeux library and the SuperNEMO software, GDR neutrino*, (2014). `https://github.com/SuperNEMO-DBD/Falaise`

Monte Carlo simulations of detectors background and development of AMS methods for radiopurity measurements

V. Palušová[1], R. Breier[1], M. Ješkovský[1], J. Kaizer[1], I. Kontul'[1], P. Loaiza[2], F. Piquemal[3], P. P. Povinec[1]

[1] *Department of Nuclear Physics and Biophysics, Comenius University, Bratislava, Slovakia*
[2] *LAL, Orsay, France*
[3] *Centre Etudes Nucleaires de Bordeaux, Gradignan, France*

Abstract. Natural radioactivity of construction materials of high-purity germanium detectors has been identified as the main component of detector background. A Monte-Carlo code was developed to evaluate the background of HPGe detector operating in the Modane underground laboratory (Laboratoire Souterrain de Modane, 4800 m w.e.). The measured background was by about 3 orders of magnitude higher than the simulated one when accounting only for its cosmic-ray components. Very low-radioactivity methods using AMS are under development at the CENTA facility in Bratislava. Preliminary studies of uranium analysis in electrolytic copper are presented.

Keywords: Monte Carlo simulation, HPGe detectors, background, radiopurity, AMS
PACS: 29.20.-c,29.40.Wk

1. INTRODUCTION

Low-radioactivity measurement techniques have been widely applied in nuclear physics experiments searching for rare nuclear events. The detectors used in these experiments should operate in deep underground laboratories where very low background is important pre-requisite. While long-lived radionuclides have been mostly analyzed by accelerator mass spectrometry (AMS) or inductively coupled plasma mass spectrometry (ICPMS) [1], analyses of short-lived radionuclides have been mainly carried out by gamma-ray spectrometry [2]. Large volume high-purity germanium (HPGe) detectors have been widely used in such measurements because of their high efficiency and good energy resolution. A background of these detectors is due to a radioactive contamination of its construction parts and of cosmic-ray component. At sea level three components of secondary cosmic-rays are observable: a hard component consisting of muons, a soft component consisting of electrons, positrons and photons, and a nucleonic component. The flux of hard component muons can be partially eliminated by using an anticosmic shield [3]. If detectors operate in deep underground laboratories, the cosmic-ray component should be negligible [4, 5, 6, 7, 8, 9], as all components of cosmic-ray induced background are substantially decreased by surrounding rock. The dominant part of the background is therefore a radioactive contamination of construction materials which is mostly represented by decay products in the ^{238}U and ^{232}Th decay series, and by ^{40}K [1, 5]. Radiopurity measurements of construction materials of underground detectors

have mostly been carried out by non-destructive gamma-ray spectrometry. Before construction of the Ge gamma-spectrometers, Monte Carlo simulations of their background should be carried out. A new generation of underground experiments (e.g. SuperNEMO experiment that searches for neutrinoless double beta-decay) require substantial improvements of their detection limits, therefore radiopurity of construction materials is a limiting factor.

2. MATERIALS AND METHODS

2.1 HPGe detectors and Monte Carlo simulations

The Ge detector under investigation was the Obelix (volume of 600 cm^3), which is operating in LSM. The passive shielding of the Obelix has an inner layer made of Roman lead of 12 cm thickness and an outer layer made of low-activity lead of 20 cm thickness [10]. The Ge crystal was placed in an aluminum cryostat.

GEANT4 and MuonSImulationCode (MUSIC) were used in Monte Carlo (MC) simulations [11]. GEANT4 was developed at CERN and is widely used for interaction simulations in nuclear physics [12]. MUSIC is a Fortran subroutine that simulates 3D transport of muons through a standard rock. The MC code for simulation of cosmic-rays has three parts: a muon generator, part describing transport of muons in surrounding rock, and simulation of the interaction of muons with the detector. Interaction model described in GEANT4 includes four mechanisms: muon ionization, muon bremsstrahlung, production of electron-positron pairs and muon photonuclear reactions. In investigation of different radionuclide contaminants, decay events should be simulated for different parts of the detector separately. Several million events per each radionuclide from the U and Th decay series and from ^{40}K were simulated. As a result we were able to compute background gamma-ray spectra.

2.2 SuperNEMO experiment

Similiar MC simulations can be performed for the SuperNEMO experiment searching for neutrinoless double beta decay in LSM using ^{82}Se as source. The basic detection strategy of the detector remains the same as it was for its predecessor, the NEMO-3 detector, but several improvements for detection components were accomplished [13, 14]. The detector technology offers a powerful tool for background rejection and combines tracking and calorimetry techniques. Background of the SuperNEMO detector consists of external (including cosmic-rays, contamination of the laboratory air and of construction materials) and internal (contamination of the internal construction parts and radon inside the tracker) sources. The most important are events that may imitate neutrinoless double beta decay [14].

Currently under investigation are gamma-rays from different origins: radioactivity of laboratory and surrounding rocks, and neutron capture and muon bremsstrahlung in rocks. It is expected, that these gamma rays have wide spectrum and will produce events in different topologies ($2e^-$, $1e^-1e^+$, crossing e^-, $1e^-$ 1gamma external) that

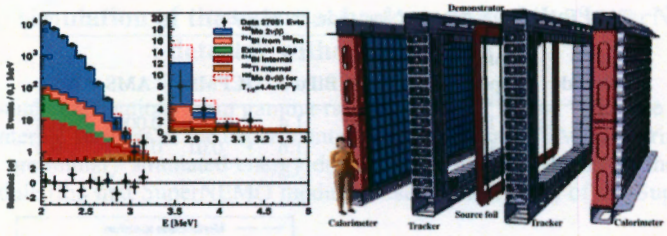

FIGURE 1. Sources of background in the NEMO-3 experiment (Arnold, 2015) and the block design of the SuperNEMO experiment

could imitate double beta-decay and neutrinoless double beta-decay. MC simulations of this external background will be done using the Falaise software (based on GEANT4), developed by the SuperNEMO collaboration.

2.3 Accelerator Mass Spectrometry (AMS)

Radiopurity of construction materials is important for reduction of background of detectors, therefore measurements of concentrations of radionuclides are of great importance for experiments that require very low background. Problem with gamma spectrometry is that analyzed radionuclides are also found in the background of the spectrometer. Alternative methods for these analyses have been under development, one of which is AMS. AMS is a technique for measuring long-lived natural and anthropogenic radionuclides that occur in the environment. It represents a change in the philosophy of counting - a direct atom counting is applied instead of waiting for decay products. A Centre for Nuclear and Accelerator Technologies (CENTA) has recently been established at the Comenius University in Bratislava. One of the goals of the CENTA laboratory is the development of the AMS technique for radiopurity measurements at levels below 1 nBq/g [15].

Very low-radioactivity measurements can be carried out mainly by AMS (Table 1), preferably without any chemical treatment of samples, as this process could add radioactive contamination from chemicals used during sample processing [16]. Tests were carried out in the CENTA laboratory using various uranium targets in the MC-SNICS ion source (multi cathode source of negative ions by caesium sputtering) and a double focusing injection magnet. Tests with analysis of uranium in wire targets made of electrolytic copper were carried out as well. The ^{238}U concentration in the wire was 10nBq/g [17].

TABLE 1. Comparison of detection limits (μBq)

Nuclide	Alpha-spec.	Gamma-spec.	BiPo-3	ICPMS	AMS	NAA
^{232}Th	100	2400	1.4	0.003	0.0002	0.08
^{238}U	100	2000	1.6	0.01	0.0001	0.2

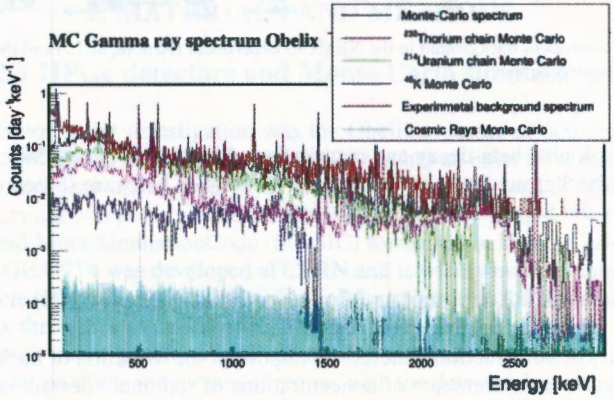

FIGURE 2. Monte Carlo simulations of background and contamination gamma-ray spectra for a HPGe detector operating in the Modane underground laboratory (4800 m w.e.)

3. RESULTS AND DISCUSSION

3.1 Gamma-ray spectra

The MC simulated background gamma-ray spectrum for the Obelix detector operating in LSM (4800 m w.e.) shows that the experimental spectrum is up to 3-orders of magnitude higher than the simulated cosmic-ray background. The difference is due to natural radioactivity in the construction parts surrounding the Ge crystal. Contributions to the Obelix detector background from environmental radionuclides (^{238}U and ^{232}Th decay products in respective chains and ^{40}K) found in various construction parts of the spectrometer were investigated. Background contributions from ^{40}K and from the ^{232}Th chain were lower than from the ^{238}U chain background continuum, except for the energies above 2000 keV, where ^{208}Tl from the ^{232}Th chain is dominant.

3.2 MC simulation of the external background of the SuperNEMO detector without shielding

Background contributions from gamma-rays of ^{214}Bi, ^{208}Tl and ^{40}K were simulated inside all internal surfaces of the experimental hall of the SuperNEMO experiment. Fig. 3 presents preliminary simulated energy deposition in the calorimeter of the Demonstrator module (the first SuperNEMO module presented in Fig. 1) of the SuperNEMO detector.

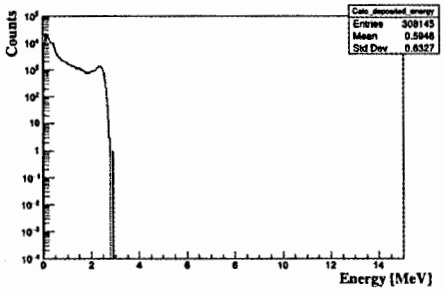

FIGURE 3. Deposited energy in the calorimeter of the SuperNEMO detector

Spectrum does not yet include neutron capture and muon bremsstrahlung in rocks, which will be covered later.

3.3 Investigations of uranium targets for AMS measurements

We did preliminary investigations with analysis of uranium in copper wire targets made of OFHC. Uranium and thorium ions extracted from the copper produce in the ion source negative ions either as uranium/thorium oxides, or as uranium/thorium compounds with copper. The ion clusters of ^{63}Cu and ^{65}Cu ($^{63}Cu_3^{65}$Cu, etc.) with masses of 254 (256), 319 (325) and 374 (388) were observed after the injection magnet, however, the UO and ThO_2 ions with masses of 254 and 264, respectively, should be expected in the first mass peak as well. This has been expected as U and Th oxides are the most frequently observed compounds of these two elements in the environment, and therefore they will make the most influential background contributions during AMS measurements. A more favourable case should be therefore a formation of negative molecules of UCu^- or $ThCu^-$ which would fall into the mass windows of 301 and 295, respectively, where they would be free of copper cluster interferences (Fig. 4). Further investigations are going on with optimization of ion production/acceleration and post-acceleration ion analyses. A work is in progress as well to separate radiochemically ^{238}U and ^{232}Th from the enriched ^{82}Se source which will be used in the SuperNEMO experiment for investigation of its neutrinoless double beta-decay.

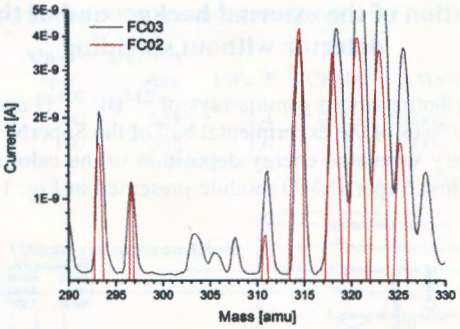

FIGURE 4. Uranium ions extracted from the copper were either as uranium oxides, or as uranium compounds with copper

4. CONCLUSIONS

MC simulation of background of the Obelix HPGe detector operating in LSM (4800 m w.e.) was carried out. When accounting only for cosmic-ray induced background the measured experimental spectrum was by about 3 orders of magnitude higher than the simulated one. The difference is due to radioactive contamination of the construction and surrounding materials placed around the Ge detector. This underlines the importance of using radiopure materials for construction of detectors used in experiments that require ultra low background. Briefly mentioned was the development of AMS technique for radiopurity measurements at CENTA in Bratislava.

ACKNOWLEDGMENTS

Colleagues from the SuperNEMO collaboration are acknowledged for fruitful collaboration. This study was carried out in the framework of the EU Research and Development Operational Program funded by the ERDF (Projects # 26240120012, 26240120026 and 26240220004, and partially also supported by the APVV (project # 15- 0576) and VEGA (project # 1/0891/17) Scientific Granting Agencies of Slovakia.

REFERENCES

1. Povinec, P.P., et al., Acta Phys. Slov. **58**, 1-154 (2008).
2. Povinec, P.P., Radioactivity in the Environment **6**, 237-294 (2003).
3. Povinec P.P., et al., Appl. Radiat. Isot. 61:85-9310 (2004).
4. Arnold et al., Phys. Rev. D **92**, 072011 (2015).
5. Heusser, G., Ann. Rev. Nucl. Part. Sci. **45**, 543-590 (1995).
6. Laubenstein, M., et al., Appl. Radiat. Isot. **61**, 167-172 (2004).
7. Heusser, G., et al., Eur. Phys. J. C **75**, 531-539 (2015).
8. Hult, M., et al., Phys. Rev. C **74**, 054311 (2006).
9. Budjas, D., et al., Appl. Radiat. Isot. **67**, 755-758 (2009).

10. Brudanin, V.B. et al.,JINST **12** (2017).
11. Kudryavtsev, V.A., Comp. Phys. Comm. **180**, 339-346 (2009).
12. Agostinelli, S. et. al., Nucl. Instrum. Methods Phys. Res. A **506**, 250-303 (2003).
13. Arnold, R., et al. Nucl. Instrum. Methods Phys. Res. A **536** , 79 (2005).
14. Povinec, P.P., Nucl. Instrum. Methods A **845**, 398-403 (2017).
15. Povinec, P.P., et al., Appl. Radiat. Isot. **126**, 26-30 (2017).
16. Povinec, P.P., et al., Nucl. Instrum. Methods Phys. Res. B **361**, 87-94 (2015).
17. Povinec, P.P., et al. , Nucl. Instrum. Methods Phys. Res. B **342**, 321-326 (2015).

Discriminating sterile neutrinos and unitarity violation with CP invariants

Philipp Sicking

Fakultät für Physik, TU Dortmund, Otto-Hahn-Str. 4, D-44221 Dortmund, Germany
E-mail: philipp.sicking@udo.edu

Abstract. We present a new method to analyze upcoming results in the search for CP violating neutrino oscillations. The CP violating amplitudes $\mathscr{A}_{\alpha\beta}^{kj}$ provide parametrization independent observables, which will be accessible by experiments soon. The strong prediction of a unique $\mathscr{A}_{\alpha\beta}^{kj}$ (the Jarlskog invariant) in case of the standard three neutrino model does not hold in models with new physics beyond the Standard Model. Nevertheless there are still correlations among the amplitudes depending on the specific model. Due to these correlations it is possible to reject specific new physics models by determining only 3 of the CP violating amplitudes.

Keywords: neutrino mixing, unitarity violation, neutrino oscillation, CP-violation
PACS: 14.60.Lm, 14.60.Pq, 14.60.St, 12.15.Ff

INTRODUCTION

A first hint for a maximal CP violation in neutrino oscillations has been reported by T2K [1, 2]. This situation cannot be understood as a proof of the minimal three neutrino picture, though. As has been shown by several authors, new physics models can fake a signal at current experiments which look like satisfying the three neutrino paradigm [3, 4, 5, 6, 7].
We present a novel approach to analyse upcoming neutrino oscillation data in the light of CP violation based on reference [8].
Neutrino oscillation probabilities are described by introducing the mixing matrix U, parametrizing the transformation from neutrino mass to flavor eigenstates, $|\nu_\alpha\rangle = \sum_k U_{\alpha k}|\nu_k\rangle$:

$$P_{\nu_\alpha\to\nu_\beta}(t) = \sum_{k,j} U_{\alpha k}^* U_{\beta k} U_{\alpha j} U_{\beta j}^* e^{-i\frac{\Delta m_{kj}^2 L}{2E}} \tag{1}$$

$$= \delta_{\alpha\beta} - 4\sum_{k>j}^{N} \mathrm{Re}(U_{\alpha k}^* U_{\beta k} U_{\alpha j} U_{\beta j}^*) \sin^2\left(\frac{\Delta m_{kj}^2 L}{4E}\right) + 2\sum_{k>j}^{N} \mathrm{Im}(U_{\alpha k}^* U_{\beta k} U_{\alpha j} U_{\beta j}^*) \sin\left(\frac{\Delta m_{kj}^2 L}{2E}\right), \tag{2}$$

where $\mathscr{A}_{\alpha\beta}^{kj} = \mathrm{Im}(U_{\alpha k}^* U_{\beta k} U_{\alpha j} U_{\beta j}^*)$. For antineutrinos the last term switches its sign, so the CP violation $P_{\nu_\alpha\to\nu_\beta} - P_{\bar{\nu}_\alpha\to\bar{\nu}_\beta}$ depends only on the CP violating amplitudes $\mathscr{A}_{\alpha\beta}^{kj}$.

Here, N indicates the number of light neutrinos involved in the oscillation process. If all neutrino mass eigenstates are small compared to the relevant energy scale at production and detection (for instance the pion mass) all eigenstates are involved in the oscillation process and the mixing matrix U is unitary. If, on the other hand, at least one mass eigenstate cannot be produced due to kinematics, or the heavy flavors can be integrated out, the resulting effective mixing matrix U can be non-unitary.

A common approximative parametrization used in the literature is based on a series expansion in $\alpha = \frac{\Delta m^2_{31}}{\Delta m^2_{21}} \ll 1$ and the unitarity of the 3×3 mixing matrix[9].

Here we rely on the exact expressions given in equation (2) instead, which is invariant under reparametrization. In particular the CP violating amplitudes $\mathscr{A}^{kj}_{\alpha\beta}$ are independent of the parametrization [10, 11] and can be determined in various extensions to the SM case.

A specific feature which had already been pointed out by Jarlskog [12],[13] is that in the case of exactly three flavors and a unitary mixing matrix U, all CP violating amplitudes $\mathscr{A}^{kj}_{\alpha\beta}$ have identical absolute values.

Inspired by previous work [10, 11] we take a closer look to sums and ratios of the CP violating amplitudes $\mathscr{A}^{kj}_{\alpha\beta}$ and find useful correlations among them. These correlations depend highly on the specific model and therefore provide a useful test for new physics in CP violating neutrino oscillations.

ANALYTIC TREATMENT OF 3+1 ν

A popular extension of the three neutrino model is to add one additional light sterile neutrino [14, 15]. In this model the mixing matrix U is now a 4×4 unitary mixing matrix but the 3×3 sub matrix is not unitary anymore. Although the resulting amplitudes are no longer unique, they are related due to the unitarity of the complete mixing matrix. By exploiting these relations it has been shown for four flavors that all amplitudes can be reduced to only three independent CP violating amplitudes [16].

In total there exist $4 \times 4 \times 4 \times 4 = 256$ ($\alpha, \beta \in \{e, \mu, \tau, s\}$ and $k, j \in \{1, 2, 3, 4\}$) different CP violating amplitudes $\mathscr{A}^{kj}_{\alpha\beta} = \mathrm{Im}(U^*_{\alpha k} U_{\beta k} U_{\alpha j} U^*_{\beta j})$, whereas the number is strongly reduced by the fact that $\mathscr{A}^{kj}_{\alpha\beta} = 0$ for $\alpha = \beta$ or $k = j$ and due to symmetry, $\mathscr{A}^{kj}_{\alpha\beta} = \mathscr{A}^{kj}_{\beta\alpha}$ and $\mathscr{A}^{kj}_{\alpha\beta} = \mathscr{A}^{jk}_{\alpha\beta}$. Therefore it is sufficient to only consider $\mathscr{A}^{kj}_{\alpha\beta}$ where $\alpha < \beta$ and $k > j$. Note that the previous relations hold due to the definition of $\mathscr{A}^{kj}_{\alpha\beta}$ regardless of the underlying U and are not specific for the 3+1ν model. This reduces the number of CP violating amplitudes to 36. These 36 amplitudes are not independent of each other and can be expressed via only nine amplitudes (see Appendix A in [8]). Again, these nine amplitudes can be expressed by three remaining amplitudes via analytical expressions (see [8] for all resulting relations).

To emphasize the differences between 3ν and $3+1\nu$ we want to highlight following

relations:

$$\mathscr{A}_{e\mu}^{31} = -\mathscr{A}_{e\mu}^{32} + \mathscr{A}_{e\mu}^{43} \tag{3}$$

$$\mathscr{A}_{e\tau}^{21} = -\mathscr{A}_{\mu\tau}^{32} + \mathscr{A}_{\tau s}^{43} \tag{4}$$

$$\mathscr{A}_{e\tau}^{31} = -\mathscr{A}_{e\tau}^{32} - \mathscr{A}_{\tau s}^{32} + \mathscr{A}_{\tau s}^{43} \tag{5}$$

The relations reduce to the 3ν case, if no mixing with the light neutrino takes place.

NUMERIC ANALYSIS OF STERILE NEUTRINOS AND NON-UNITARY SCENARIOS

The relations in the previous section rely on the unitarity of the resulting $3+1\nu$ model. In general these relations are, if possible, harder to find and more complicated. An easier approach is to use a numeric analysis of the correlations of the different amplitudes for different models. Therefore we pick random numbers for all parameters in the specific model. Since the elements of U are independent of the parametrization we are free to choose the standard parametrization from [17].

To check if the generated combination of parameters satisfy current experimental bounds, we compare the entries of the 3×3 sub matrix of U with the bounds presented in [18], where a global fit is performed without implying a unitarity of $U^{3\times3}$. For a viable combination of parameters all accessible amplitudes $\mathscr{A}_{\alpha\beta}^{kj}$ are calculated and extracted. For each model we extracted 100,000 viable combinations. To show the correlation we performed a kernel density estimation for different combination of amplitudes, i.e. estimating the underlying probability density function by summing up Gaussian kernels placed on every data point.

We compare 4 different approaches of neutrino physics beyond the three neutrino paradigm:

(i) a model of one additional light sterile neutrino $(3+1\nu)$,

(ii) a model of two additional light sterile neutrinos $(3+2\nu)$,

(iii) a scenario of non-unitarity without additional constraints (NU) realized by modifying the unitary matrix with a lower triangular matrix α[19, 20, 21]

$$U_{NU} = (I-\alpha)U^{3\times3} = \begin{pmatrix} 1-\alpha_{ee} & 0 & 0 \\ \alpha_{e\mu} & 1-\alpha_{\mu\mu} & 0 \\ \alpha_{\tau e} & \alpha_{\mu\tau} & 1-\alpha_{\tau\tau} \end{pmatrix} U^{3\times3}, \tag{6}$$

(iv) a scenario of non-unitarity where additional fermions trigger rare decays like $\mu \to e\gamma$. The corresponding constraints from rare decays and electroweak precision observables are presented in [22] ("minimal unitarity violation" (MUV), the non unitarity is parametrized as in scenario (iii))

RESULTS

The 95% CL of the generated kernel density estimates for oscillations of ν_μ are shown in figure 1. As can be seen clearly for the scenarios with additional light neutrinos and non unitarity without constraints, the corresponding parameter spaces allow for significant deviation from the SM prediction of uniform CP violating. The MUV scenario albeit provides only a comparatively small allowed region. The strong constraints for the unitary violating parameters α as priors strongly restrict deviations from the SM prediction. The allowed regions fulfill all current bounds and display the current uncertainties and the not yet determined CP phase(s).

The differences between the $3+1\nu$- and $3+2\nu$-model are negligible. Due to invariance under re-parametrization the amplitudes in the 3×3 sub matrix do not change by rotations in the 4-5-Plane in case of a $3+2\nu$-model. To investigate a difference between $3+1\nu$ and $3+2\nu$ scenarios, amplitudes with sterile states or additional mass squared differences have to be taken into account which are not expected to be accessible experimentally in the near future.

Comparing the models with additional light neutrinos with the scenario of unconstrained non-unitarity one can find large deviations. The scenario of non unitarity provides viable parameter sets which are far outside the 95% CL of the models with additional light neutrinos.

The MUV scenario provides only a small deviation from the SM due to the strong constraints from electroweak precision observables. The expected deviations are out of reach of current experiments. Therefore a sizable measured deviation from the SM has to have another source than the MUV scenario.

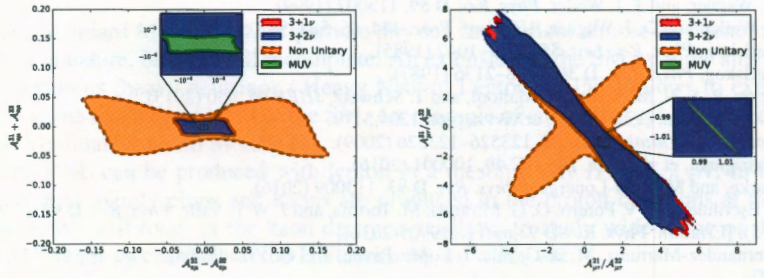

FIGURE 1. Kernel density estimates for the different scenarios: $3+1\nu$ in red, $3+2\nu$ in blue, Non-Unitarity in yellow and Minimal Unitarity Violation in green. In the left (right) panel it is shown the differences (ratios) of the 3 different CP violating amplitudes in the $\nu_e \to \nu_\mu$ ($\nu_\mu \to \nu_\tau$) -channel. The colored area corresponds to the 95% CL of the KDE.

CONCLUSION

We have presented a new method to test and discriminate the standard three neutrino paradigm and several extensions based on the study of various combinations of CP vi-

olating amplitudes $\mathscr{A}^{kj}_{\alpha\beta}$. These amplitudes are easily accessible via oscillation experiments searching for CP violation. The amplitudes and the relations among them have been translated into the notation commonly used in the neutrino community. Moreover, the concept has been generalized to scenarios with five neutrinos and non-unitary mixing matrices. Powerful discriminators between different scenarios of physics beyond the SM can be exploited once experiments determine three different amplitudes. In this case it is possible to rule out not only the three neutrino paradigm but also models of additional sterile light neutrinos or the scenario of MUV in large regions of the respective parameter spaces. On the other hand, a determination of a unique amplitude would be in agreement with both the three neutrino model but also with specific parameter combinations of new physics models.

Note, that these calculations rely on the vacuum values of neutrino properties. They are independent of specific mass differences.

REFERENCES

1. K. Abe, et al., *Phys. Rev.* **D91**, 072010 (2015).
2. H. T. for the T2K collaboration, Status, recent results and plans for T2K (2016), URL `http://neutrino2016.iopconfs.org/IOP/media/uploaded/EVIOP/event_582/Tanaka__Hirohisa.pdf`, presented at Neutrino 2016 conference.
3. S. Goswami, and T. Ota, *Phys. Rev.* **D 78**, 033012 (2008).
4. O. G. Miranda, M. Tortola, and J. W. F. Valle, *Phys. Rev. Lett.* **117**, 061804 (2016).
5. S.-F. Ge, P. Pasquini, M. Tortola, and J. W. F. Valle (2016), arXiv: hep-ph 1605.01670.
6. A. de GouvÃła, and K. J. Kelly (2016), arXiv: hep-ph 1605.09376.
7. D. Dutta, and P. Ghoshal, *JHEP* **09**, 110 (2016).
8. H. PÃd's, and P. Sicking, *Phys. Rev.* **D 95**, 075004 (2017).
9. M. Freund, *Phys. Rev.* **D 64**, 053003 (2001).
10. D. J. Wagner, and T. J. Weiler, *Phys. Rev.* **D 59**, 113007 (1999).
11. T. J. Weiler, and D. J. Wagner, *AIP Conf. Proc.* **444**, 46–58 (1998).
12. C. Jarlskog, *Phys. Rev. Lett.* **55**, 1039–1042 (1985).
13. C. Jarlskog, *Phys. Rev.* **D 36**, 2128–2136 (1987).
14. J. Kopp, P. A. N. Machado, M. Maltoni, and T. Schwetz, *JHEP* **05**, 050 (2013).
15. K. N. Abazajian, et al. (2012), arXiv: hep-ph 1204.5379.
16. T. Suzuki, *J. of Math. Phys.* **50**, 123526–123526 (2009).
17. C. Patrignani, et al., *Chin. Phys.* **C 40**, 100001 (2016).
18. S. Parke, and M. Ross-Lonergan, *Phys. Rev.* **D 93**, 113009 (2016).
19. F. J. Escrihuela, D. V. Forero, O. G. Miranda, M. Tortola, and J. W. F. Valle, *Phys. Rev.* **D 92**, 053009 (2015), [Erratum: Phys. Rev.D 93,no.11,119905(2016)].
20. E. Fernandez-Martinez, M. B. Gavela, J. Lopez-Pavon, and O. Yasuda, *Phys. Lett.* **B 649**, 427–435 (2007).
21. S. Antusch, C. Biggio, E. Fernandez-Martinez, M. B. Gavela, and J. Lopez-Pavon, *JHEP* **10**, 084 (2006).
22. M. Blennow, P. Coloma, E. Fernandez-Martinez, J. Hernandez-Garcia, and J. Lopez-Pavon (2016), arXiv: hep-ph 1609.08637.

Search for heavy neutrinos in the ND280 near detector of the T2K experiment

A. Izmaylov[1,2], S. Suvorov[1,3]

[1] *INR RAS, prospekt 60-letiya Oktyabrya 7a, Moscow 117312*
[2] *IFIC CSIC*
[3] *CEA/IRFU Saclay*
e-mail: suvorov@inr.ru

Abstract. The presence of Heavy Neutral Leptons (HNL, $M \approx O(1GeV)$), or heavy sterile neutrinos is proposed in various theories in order to solve current problems of the Standard Model (SM), e.g. the origin of (tiny) neutrino masses, dark matter, baryon asymmetry etc. The T2K experiment provides intense neutrino beam from both pion and kaon parents and hence allows to carry out experimental search for the HNL of < 500 MeVs mass range. We have performed the search of the HNL based on the usage of the low-density region in ND280, Time Projection Chambers (TPC) with MC data. This article provides the summary of the MC simulation, event selection, systematics study. We obtain that with the T2K data we can expect the improvements of the limits on the HNL mixing elements for the high mass region ($M_{HNL} > 0.42$ GeV) and the cross-check of the previous results for lower masses.

Keywords: T2K, neutrino, heavy neutrino
PACS: 13.35.Hb; 14.60.Pq; 14.60.St.

INTRODUCTION

Heavy neutral leptons

The Standard Model (SM) of particle physics can explain almost all phenomena observed in nature, but it is still incomplete. An extension of the SM by three singlet massive fermions (heavy neutrinos / Heavy Neutral Leptons - HNL) allows to explain the phenomena that cannot be fit to the SM. An example of such theory is the νMSM (neutrino Minimal Standard Model) [1].

The HNL can be produced with lepton in a meson decay $H \to \ell_{e,\mu,\tau} N$. In the T2K experiment mainly pions and kaons are produced in the proton collisions at the target station. We will focus at the kaon decay as it allows to study wide range of the HNL mass. The decay channels of the HNL with $M_{HNL} < M_K$ are:

$$N \to \ell\pi \tag{1}$$

$$N \to \ell\ell\nu \tag{2}$$

$$N \to \gamma\nu, \qquad N \to 3\nu, \qquad N \to \nu\pi^0 \tag{3}$$

We will study 2-body decays (1) and 3-body decays (2). Daughter particles from decays (3) are practically undetectable. The Fig. 1 shows reactions of the HNL production and decay, that we are going to study and heavy neutrino mass region for each process.

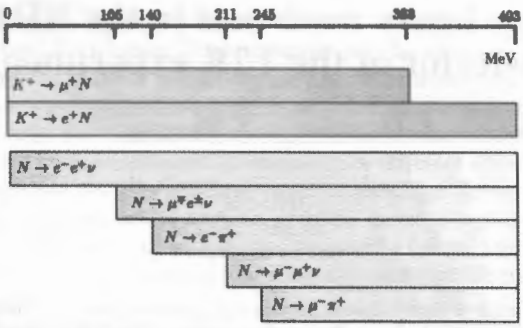

FIGURE 1. Summary of the production and the detection processes of the heavy neutrino. The horizontal axis corresponds to the HNL mass.

The T2K experiment

In our work we study a possibility of the improvement of the constraints on mixing elements in the T2K experiment. It is accelerator long-baseline neutrino oscillation experiment. Details of the experiment setup can be found in the Ref. [2]. The neutrino beam is produced in the mesons decay in the decay volume. The mesons are born in the interactions of the protons from the 30 GeV J-PARC accelerator at the target station. The ND280 is the off-axis detector located 280 m from the target station. The detector consists of: π^0 detector (P0D); three Time Projection Chambers (TPC) alternating with Fine Grained Detectors (FGD) that forms tracker; an electromagnetic calorimeter (ECal) that surrounds the tracker; and the recycled UA1 magnet instrumented with scintillator to perform as a muon range detector (SMRD). The overall view of the ND280 is presented in the Fig. 2.

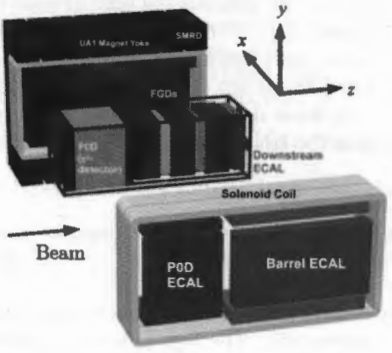

FIGURE 2. An exploded view of the ND280 off-axis detector.

ANALYSIS STRATEGY

The main background processes for the HNL decay are interactions of the active neutrinos. For background suppression we decided to use only fiducial volume of the TPCs. The difference of the density between the gas (TPC) and the scintillator (FGD) is significant. As number of the active neutrino interactions depends on the density, this method provides significant background reduction.

The rate of background processes (the cross-section of active neutrino interactions in gas, kaon production, etc.) is very poor studied. Because of this, we are going to develop a cut sequence to suppress the background as much as possible, then interpret all the events observed in data as a signal and put the constraints on mixing elements. Thus our analysis will be completely independent from the neutrino interactions models. The statistical approach to the low level signal analysis is described in Highland and Cousins paper [3]. Both HNL production and decay rate are $\propto |U_i|^2$, as we are looking for heavy neutrino decay the number of expected events is $\propto |U_i|^4$. Thus constraints on mixing elements looks like:

$$|U_i|^2_{limit} = \sqrt{\frac{U_n}{N_{events}}} \tag{4}$$

$$U_n = U_{n0}\left(1 + E_n\frac{\sigma^2_{Acc}}{2}\right)\left(1 + \left(\frac{E_n\sigma_{Acc}}{2}\right)^2\right) \tag{5}$$

where $i = e, \mu$; U_{n0} is 90% C.L. Poisson limit for n observed events, $E_n = U_{n0} - n$, σ_{Acc} is the acceptance error and N_{events} is expected number of signal events assuming $|U|^2 = 1$.

HNL SIMULATION

To estimate the sensitivity to the mixing elements in our experiment we need to evaluate the expected number of events from the HNL decay. First of all we need to estimate the HNL flux at the ND280. The results of the MC modeling of the beam were used. Thus we got all the information about neutrinos, that have entered the ND280, and their parent mesons. We assume that instead of ordinary neutrinos parent mesons decay into the heavy ones. So the kinematics and branching ratio were recalculated and the HNL spectra were obtained. From the spectra of the heavy neutrinos, we can estimate the expected number of events from HNLs decays, assuming the long life-time of the heavy neutrino ($\tau \gg 1\mu s$).

Based on estimated number of signal events we concluded that we can improve the limits on mixing elements only in 2-body decay modes. So for the following study we will concentrate on them.

ANALYSIS OF HNL EVENTS

Event selection

For selection of the HNL signal events and for background reduction the cut sequence was designed:

1. Global vertex in the TPC fiducial volume.
2. Two different charged tracks associated with this vertex;
3. No activity in the upstream detector;
4. No other tracks start in the same TPC;
5. Proper particle identification as $e\pi$ or $\mu\pi$ using dE/dx in the TPC;
6. Invariant mass cut: $140MeV < M_{HNL} < 850MeV$ for the $e\pi$ mode and $250MeV < M_{HNL} < 750MeV$ for the $\mu\pi$ mode;
7. Polar angle for HNL candidate $\theta < 8.0°$ for the $e\pi$ mode and $\theta < 3.7°$ for the $\mu\pi$ mode, since the HNL direction should be extremely collinear to the neutrino beam;
8. Kinematic cut on the opening angle between daughter particles $cos\theta > 0$;

Applying all these cuts to the signal samples gives us the total selection efficiency that is presented on the Fig. 3.

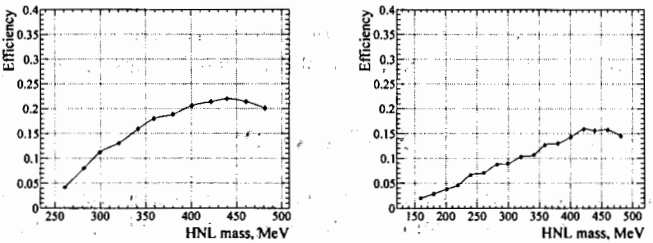

$K^+ \to e^+N \to e^+(\mu^\mp\pi^\pm)$ $K^+ \to e^+N \to e^+(e^\mp\pi^\pm)$

FIGURE 3. Selection efficiency for two body decays of HNL.

Applying the same selection cuts to MC samples for different neutrino generators (NEUT, GENIE, NuWro), we estimate the expected background: 1.13 events for mode $N \to \mu\pi$ and 0.77 for mode $N \to e\pi$.

Systematic uncertainties

The systematics uncertainties in our study come from the number of predicted events. The main sources of uncertainties are: parent meson flux, detector acceptance. Flux uncertainty was estimated based on the NA61 studies [4]. This systematics was estimated at level of 20% and one is dominating in our analysis. The detector acceptance uncertainty was obtained in the common way as for the standard T2K analysis. The technical

details of this methods can be found in the T2K paperThe total value of the detector systematics was estimated at level of 5%.

As we apply veto cuts (no activity in the upstream detector, no other tracks in the same TPC) the pile up is possible. We studied how often such pile ups were observed and apply the correction which is near 4%.

CONCLUSION

After studying the MC efficiency, background processes, systematics and pile ups, limits on mixing elements based on MC data can be estimated. The results are shown in Fig. 4, they are compared with previous constrictions made by PS191 [5].

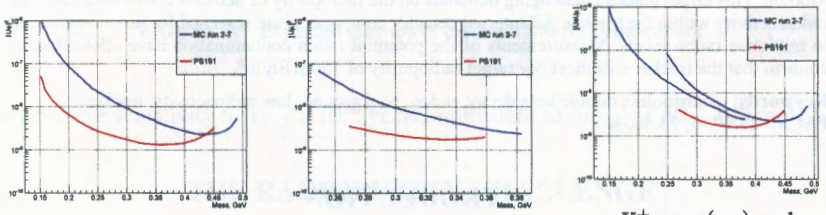

$K^+ \to e(e\pi)$ $K^+ \to \mu(\mu\pi)$ $K^+ \to \mu(e\pi)$ and $K^+ \to e(\mu\pi)$

FIGURE 4. Sensitivity to mixing elements $|Ue|^2, |U\mu|^2, |UeU\mu|$ for statistics $(6.2\nu + 6.29\bar{\nu}) \cdot 10^{20} POT$ based on MC data.

As one can see in the T2K experiment the improvements of the PS191 limits can be obtained with the current statistics.

REFERENCES

1. T. Asaka, and M. Shaposhnikov, *Physics Letters B* **620**, 17–26 (2005).
2. K. Abe, et al., *Nuclear Instruments and Methods in Physics Research Section A: Accelerators, Spectrometers, Detectors and Associated Equipment* **659**, 106–135 (2011).
3. R. D. Cousins, and V. L. Highland, *Nuclear Instruments and Methods A: Accelerators, Spectrometers, Detectors and Associated Equipment* **320**, 331–335 (1992).
4. N. Abgrall, A. Aduszkiewicz, Y. Ali, E. Andronov, T. Antićić, N. Antoniou, B. Baatar, F. Bay, A. Blondel, J. Blümer, et al., *The European Physical Journal C* **76**, 84 (2016).
5. G. Bernardi, G. Carugno, J. Chauveau, F. Dicarlo, M. Dris, J. Dumarchez, M. Ferro-Luzzi, J.-M. Levy, D. Lukas, J.-M. Perreau, et al., *Physics Letters B* **203**, 332–334 (1988).

Low Radon Background Techniques for the SuperNEMO Experiment

Fang Xie, on behalf of the SuperNEMO collaboration

Department of Physics and Astronomy, University College London, Gower Street, London WC1E 6BT, UK

Abstract. SuperNEMO is a tracker-calorimeter neutrinoless double beta decay experiment using ^{82}Se, which has a designed capability of reaching half-life sensitivity of $T_{1/2} > 10^{26}$ years, equivalent to an effective Majorana neutrino mass of $\langle m_{\beta\beta} \rangle < 50 - 100$ meV [1]. To achieve this sensitivity, SuperNEMO aims to be a zero background $0\nu\beta\beta$ experiment in the first phase Demonstrator Module. This target placed challenging demands on the radiopurity of detector components and the radon activity within the tracker. All internal detector components are screened for radon emanation to minimise radon levels. Measurements of the potential radon contamination have allowed us to confirm that the tracker will meet our target radiopurity of 150 μBq/m^3.

Keywords: neutrinoless double beta decay, radon, background, low radioactivity, tracker
PACS: 29.40.-n; 23.40.-s

INTRODUCTION

SuperNEMO [2] is an ultra-low-background tracker-calorimeter experiment improving upon the NEMO-3 design to look for the $0\nu\beta\beta$ decay. The baseline design of the SuperNEMO experiment will contain 20 identical modules, housing 100 kg of ^{82}Se in total. Unlike its predecessor the NEMO-3 experiment which had a cylindrical detector, the SuperNEMO modules, using the similar tracker-calorimeter technology, will have planar geometry. The first module, the demonstrator-which is currently under construction-contains a source frame, surrounded by a gas tracker which in turn is enclosed by a calorimeter. The general layout of the demonstrator module is shown below in Figure 1.

Initially, the source will be 7 kg of ^{82}Se mixed in a PVA base to create thin foils, suspended from the source frame. Other isotopes, such as ^{150}Nd and ^{48}Ca, can also be studied as this modular design allows us to change sources.

The tracker which consists of 2034 drift cells operating in Geiger mode, is arranged in rows of nine cells on both sides of the source foil. Each cell consists of a central anode wire in the centre, surrounded by 12 field wires, with copper cathode end caps on the two ends.

The demonstrator calorimeter consists of 712 PMTs with scintillator blocks in total. Two main walls, situated outside the tracker, consist of 520 high-resolution 8-inch radiopure PMTs coupled to scintillator blocks. Lower-resolution PMTs are placed around the bottom, top, and side edges of the tracker chamber to offer 4π acceptance.

Running for 2.5 years, the Demonstrator Module will have a sensitivity to the $0\nu\beta\beta$ half-life of $T_{1/2} > 6.5\times10^{24}$ years, equivalent to $\langle m_{\beta\beta} \rangle < 0.2 - 0.4$ eV. The full SuperNEMO detector with an exposure of 500 kg years (5 years, 100 kg of 82 Se) will

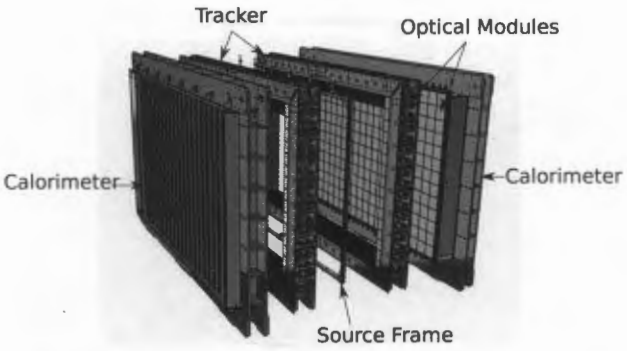

FIGURE 1. Expanded diagram of the SuperNEMO Demonstrator

improve our sensitivity to $T_{1/2} > 10^{26}$ years, equivalent to $\langle m_{\beta\beta} \rangle < 50 - 100$ meV.

THE RADIOPURITY CHALLENGE

All materials contain some trace of uranium (U) and thorium (Th) and their decay products, one of which is radon. Radon is a colourless, odourless inert gas with a long diffusion length. It can enter the detector either through diffusion, contamination during construction or emanation from the detector materials. Since the beta decays of its daughter isotopes, ^{214}Bi and ^{208}Tl, can mimic $0\nu\beta\beta$ due to their high Q_β value which is close to the characteristic $0\nu\beta\beta$ energy, radon is one of the largest backgrounds for the SuperNEMO experiment.

Simulations show that to achieve the designed sensitivity, the level of radon inside the tracker gas must be below 150 μBq/m^3. Additionally, source foil contamination should be below 10 μBq/kg for ^{214}Bi and below 2 μBq/kg for ^{208}Tl.

To achieve these challenging targets, all potential construction materials are tested with a High-Purity Germanium (HPGe) detector to verify their radiopurity levels. Materials directly exposed to the tracker were further measured for their radon emanation level as radon inside the tracker is one of the major contributions to detector backgrounds.

RADON DETECTOR AND EMANATION CHAMBERS

The radon level inside the tracker chamber should be less than 150 μBq/m^3. This is a significant challenge as even measuring such low levels is not trivial. The best commercial radon detectors can normally achieve the sensitivities down to 0.5 Bq/m^3, which is still four orders of magnitude above the SuperNEMO tracker gas radiopurity requirements. Therefore, a custom-made state-of-art electrostatic detector, capable of

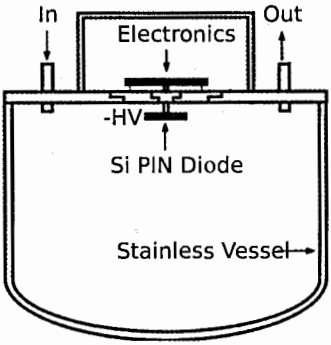

FIGURE 2. Electrostatic radon detector schematic

measuring down to levels of 1-2 mBq/m^3, was used in this work.

The detector, originally developed for the ELEGANT V experiment [3], consists of a 70-litre volume electro-polished stainless steel chamber with a silicon PIN diode placed on the top, as shown in Figure 2. The detector electronics are separated from the detection chamber by a sheet of perspex with a feedthrough for the PIN diode. The electronics applied a high negative voltage to the PIN diode, generating an electric field that was used to collect the positive decay products of radon. The gas flow input and output valves were coated with SBR to prevent radon diffusion.

Two 2.6 litre stainless steel chambers, developed at UCL with sensitivities of 100-200 μBq per sample, were used to isolate samples in order to measure their radon emanation. This allows us to make an accurate estimate of the radon level of the tracker via direct measurement of the radon emanation rate of components in their real-operation geometry.

RADON CONCENTRATION LINE

The sensitivity of the electrostatic detector is still an order of magnitude worse than required. Therefore, a new piece of apparatus named the radon concentration line (RnCL) was developed at UCL to monitor and confirm the radon levels within the sub-tracker modules (C-sections) during their construction. The design of the RnCL is similar to the MoReX line [4] developed in Heidelberg, however, the design has been simplified for portability [5].

The RnCL takes large volumes of gas and absorbs the radon content before transferring the concentrated sample from a radon trap into the electrostatic detector. The concept is to concentrate radon by pumping a large volume of gas through a 3 nm particle filter and then through a -40°C cold ultra-radiopure charcoal trap where the radon is stored. The trap is then heated, releasing the concentrated sample, which is then transferred to the electrostatic detector. The sample should now be at a concentration high enough that it can be measured by the electrostatic detector. The RnCL is calibrated us-

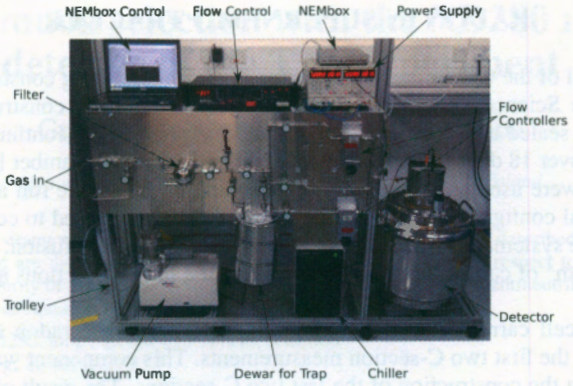

FIGURE 3. RnCL in real-life operation

ing a flow-through type source with known activity. In a typical calibration run, a known amount of radon is flushed into the detector to determine the detection efficiency. The gas, carrying radon, is then purged through the cold trap to absorb radon, and then to exhaust. In the final step, radon is released from the heated trap and purged into the detector using helium, to determine the trapping and transfer efficiency, see Figure 4 (left). The sensitivity of the RnCL can be calculated for a set gas volume of constant activity. The detection efficiency depends on the isotope and the carrier gas. With 11 m^3 of helium as the carrier gas, the RnCL sensitivity to the radon levels is as low as 15 $\mu Bq/m^3$ (90% CL) (see Figure 4 (right)).

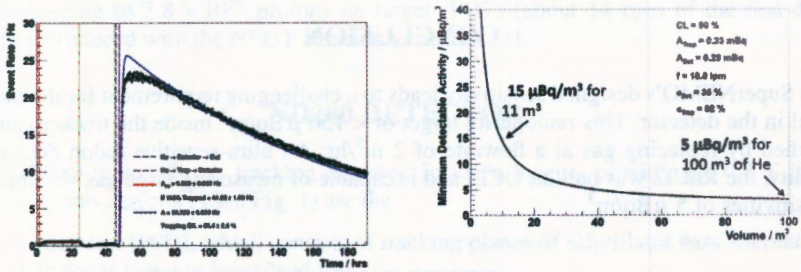

FIGURE 4. Typical calibration of RnCL trapping efficiency (left). Minimum detectable activity of the RnCL to a gas supply of constant activity over the duration of trapping as a function of gas volume (right).

A gas pre-purification trap was installed prior to the RnCL in order to minimise systematics coming from radon contamination of the carrier gas. It consists of two freezers, one at - 50°C and the other at - 80°C, with 4 kg charcoal cartridges in total. It was designed and built at Center for Particle Physics of Marseilles (CPPM) and it is capable of suppressing radon by a factor of 20 for Nitrogen and 10^{10} for Helium [6].

RADON IN SUPERNEMO TRACKER

The radon level of the C-sections was monitored via RnCL during construction at UCL Mullard Space Science Laboratory (MSSL). After being fully constructed, each C-section is then sealed and kept under a constant overpressure by continuously flushing with nitrogen over 18 days to remove residual radon inside the chamber [5]. Special gas sealing plates were used as a temporary replacement of the source foil and calorimeter wall of the final configuration. An anti-radon tent was also applied to cover C-sections to minimise the systematics coming from environmental radon diffusion. Each measurement used $\sim$8 m^3 of carrier gas. Results from the first three C-sections are summarised in Table 1.

The geiger cell carriers that contributed significantly to the radon emanation was identified after the first two C-section measurements. This component was immediately replaced during the construction of the last two C-sections. The result of C2 shows the radon level was significantly reduced.

Taking an average radon level for the final sub-tracker C3, the activity of the full demonstrator can be estimated at 41.3 ± 4.7 mBq. During operation, this radon level can be reduced by constantly flushing the tracker with purified gas from a pre-purification trap. At a gas circulation rate of 2 m^3/hr, the target activity of <150 μBq/m^3 is reached.

TABLE 1. Radon activity inside SuperNEMO C-Sections.

C-Scection	Activity (mBq/m^3)
C0	11.37 ± 1.44
C1	$15.26^{+2.5}_{-4.0}$
C2	4.36 ± 1.31

CONCLUSION

The SuperNEMO's designed sensitivity leads to a challenging requirement for the radon level in the detector. This radiopurity target of < 150 μBq/m^3 inside the tracker can be reached by replacing gas at a flowrate of 2 m^3/hr. An ultra-sensitive radon detection facility, the RnCL, was built at UCL, and is capable of measuring large gas volumes to sensitivities of 5 μBq/m^3.

REFERENCES

1. R. Saakyan on behalf of the SuperNEMO Collabration, *Phys. Conf. Ser.* **179**, 012006 (2009).
2. R. Arnold, et al. *Eur. Phys. J. C* **70**, 927 (2010).
3. E. Choi, et al *Nucl. Instr. Meth. A* **459**, 177 (1996).
4. G. Heusser, et al. *Appl. Rad. Isot.* **52**, 691 (2000).
5. X.R. Liu on behalf of the SuperNEMO Collaboration, *J. Phys. Conf. Ser.* **888**, 012085 (2017).
6. X.R. Liu on behalf of the SuperNEMO Collaboration, *AIP Conf. Proc.* **1672**, 070002 (2015).

Antimuon selection with the ND280 near detector of the T2K experiment

Grzegorz Żarnecki for T2K Collaboration

National Centre for Nuclear Research, 05-400 Otwock, Poland

Abstract. The strategy of antimuon selection in the T2K near detector is described and ideas for its improvement are discussed. Different approaches are compared with respect to the selection efficiency and purity of the antimuon sample. Presented results refer to the antineutrino beam mode running, where antimuon is a signature of antineutrino CC interaction.

Keywords: ND280, long baseline experiment, selection
PACS: 13.15.+g; 29.40.-n; 29.85.Fj

INTRODUCTION

T2K (Tokai-to-Kamioka) [1] is a long-baseline neutrino oscillation experiment situated in Japan. The beam source and near detectors (*off-axis* ND280 and *on-axis* INGRID relative to the neutrino beam) are located in the J-PARC facility in Tokai, while the *off-axis* far detector is Super-Kamiokande in Kamioka, 295 km away.

The beamline design allows for using neutrino or antineutrino beam mode. The prediction of the oscillated spectrum at the far detector is based on the beam simulation and cross section models. They are improved by fitting samples of charged-current (CC) interactions at ND280, which also allows for decrease of systematic uncertainties. [2]

This article presents the results of the study of the ND280 selection optimisation for the antineutrino beam mode running. The results are obtained using Monte Carlo corresponding to 3.8×10^{21} protons on target (POT) (about 14 runs of the real-data taking), produced with the NEUT neutrino generator [3].

ND280 DETECTOR

The ND280 is an *off-axis* tracking detector. Inside a magnet providing a 0.2 T field following sub-detectors (See Fig. 1) are the:

- π^0 detector (POD), which consists of tracking planes of scintillator bars alternating with water target or brass/lead foil.
- Tracker, consisting of two Fine-Grained Detectors (FGDs) which consist of scintillator bars layers and three Time Projection Chambers (TPCs) - gaseous detectors allowing for three dimensional track reconstruction.
- Electromagnetic Calorimeter (ECAL), which consists of scintillator bars alternating with lead absorber layers.

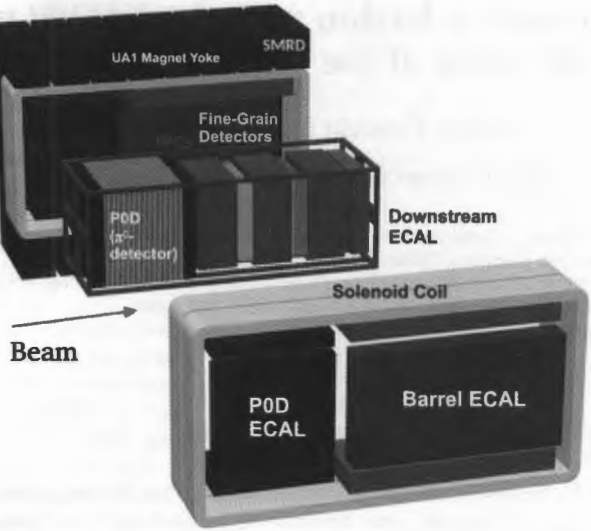

FIGURE 1. Cut-away drawing showing sub-detectors of the ND280.

- Side Muon Range Detector (SMRD), consisting of scintillator modules inserted into gaps in the magnet yokes, measuring muons which escape the inner detectors perpendicularly to the beam direction.

THE TPC'S ROLE IN μ^+ SELECTION

Identification of μ^+ is a crucial task for ND280 as it is the signature of the antineutrino CC interaction: $\bar{\nu}_\mu + N \rightarrow \mu^+ + X$.

The μ^+ selection is based on two stages. The first is preselection, when the most energetic positive track in the event is identified. It must contain enough TPC segments and its vertex must lay within the FGD fiducial volume. After the preselection, TPC particle identification (TPC PID) is executed. The basic information used for the TPC PID step is the measured particle's energy loss per unit length which is compared with the expected energy loss for a certain particle hypothesis: muon, electron, proton or charged pion ($i = \mu, e, p, \pi$). Knowing the uncertainty on the energy deposit, one can estimate the pull variable δ_i, which is normally distributed for the correct hypothesis. The pull variable is obtained separately for each TPC crossed by the track. Then the corresponding likelihood L_i is calculated: [4]

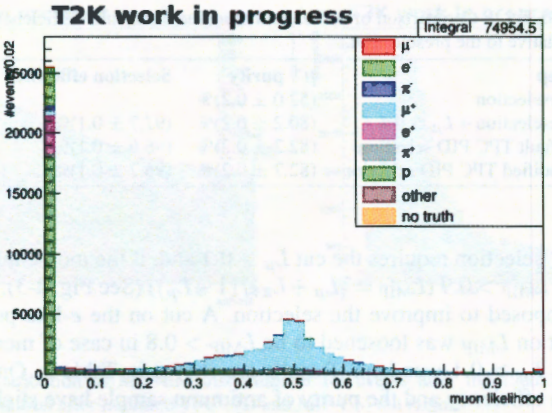

FIGURE 2. Muon likelihood L_μ distribution after preselection. The cut on this variable is the most important element of the TPC PID selection.

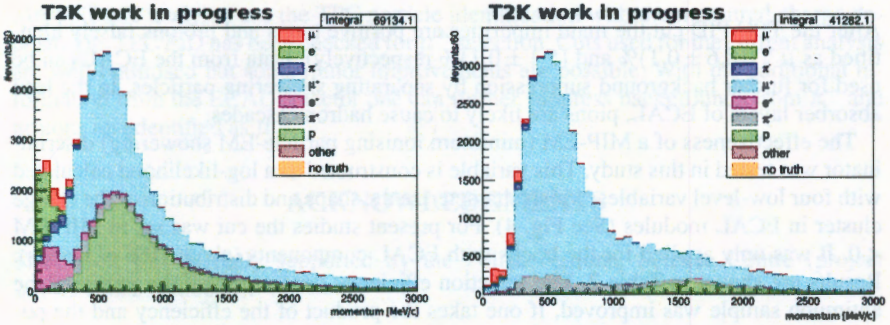

FIGURE 3. Momentum distribution after preselection (left); Momentum distribution after default TPC PID selection (right).

$$L_i = \frac{P_i}{P_\mu + P_e + P_p + P_\pi}, \tag{1}$$

where the probability density functions are defined as:

$$P_i = \frac{1}{\sqrt{2\pi}\sigma_i} \exp[-\frac{\delta^2_{i,\mathrm{TPC2}}}{2} - \frac{\delta^2_{i,\mathrm{TPC3}}}{2}] \tag{2}$$

(if the track crosses only one TPC, then only one $\delta_{i,j}$ is used in the formula above. Note that TPC1 is not considered, as it is situated upstream from the FGDs.)

TABLE 1. Comparison of default and modified cut results. Efficiency is relative to the preselection.

Step	μ^+ purity	Selection efficiency
preselection	$(52.0 \pm 0.2)\%$	
preselection + $L_\mu > 0.1$	$(80.2 \pm 0.2)\%$	$(97.7 \pm 0.1)\%$
default TPC PID selection	$(82.2 \pm 0.2)\%$	$(96.6 \pm 0.1)\%$
modified TPC PID selection	$(82.7 \pm 0.2)\%$	$(96.7 \pm 0.1)\%$

The default μ^+ selection requires the cut $L_\mu > 0.1$ and, if the momentum < 500 MeV the additional cut $L_{\mathrm{MIP}} > 0.9$ ($L_{\mathrm{MIP}} = (L_\mu + L_\pi)/(1 - L_p)$) (See Fig. 2-3). An alternative approach was proposed to improve the selection. A cut on the e-like pull $\delta_e < 0$ was added and the cut on L_{MIP} was loosened to be $L_{\mathrm{MIP}} > 0.8$ in case of momentum < 200 MeV. The cut on $L_\mu > 0.1$ was kept. Results are shown in Table 1. One can see that both the selection efficiency and the purity of antimuon sample have slightly improved, though in case of the efficiency the difference lays within statistical uncertainty.

ECAL USAGE FOR μ^+ SELECTION

After the TPC PID cut the main impurities are positive pions and protons falsely identified as μ^+ ($(8.6 \pm 0.1)\%$ and $(5.1 \pm 0.1)\%$ respectively). Data from the ECAL can be used for further background suppression by separating showering particles. In the lead absorber layers of ECAL, pions are likely to cause hadron cascades.

The effectiveness of a MIP-EM (minimum ionising particle-EM showering) discriminator was tested in this study. This variable is constructed as a log-likelihood calculated with four low-level variables, which characterize the shape and distribution of the charge cluster in ECAL modules (See Fig. 4). For present studies the cut was set to MIP-EM < 0. It was only applied for the tracks with ECAL components (about 70% of events). Results are shown in Table 2. The selection efficiency decreased, but the purity of the antimuon sample was improved. If one takes the product of the efficiency and the purity as a figure of merit, then the selection is slightly improved; however the difference lies within the statistical uncertainty. The product's value changes from 0.800 ± 0.002 to 0.802 ± 0.002.

Usage of ECAL information results in additional systematic uncertainties and is currently under discussion.

TABLE 2. Result of adding MIP-EM cut. Efficiency is relative to the preselection.

Step	μ^+ purity	Selection eff.	π^+ fraction	p fraction
modified TPC PID selection	$(82.7 \pm 0.2)\%$	$(96.7 \pm 0.1)\%$	$(8.6 \pm 0.1)\%$	$(5.1 \pm 0.1)\%$
modified TPC PID + MIP-EM cut	$(84.9 \pm 0.2)\%$	$(94.5 \pm 0.1)\%$	$(7.3 \pm 0.1)\%$	$(4.7 \pm 0.1)\%$

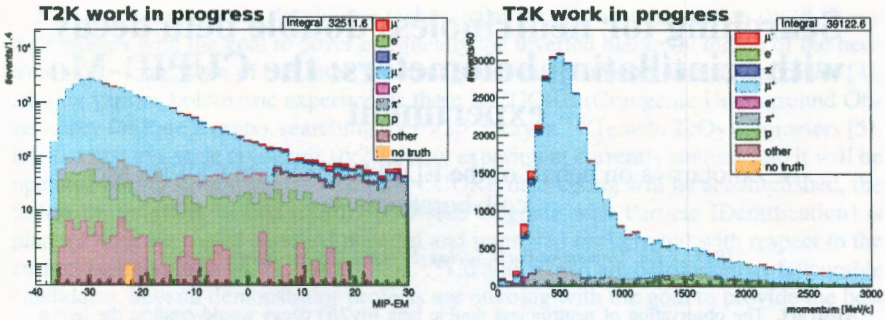

FIGURE 4. Distribution of MIP-EM discriminator for events after modified TPC selection (left); Momentum distribution after modified TPC PID and MIP-EM cut (right).

CONCLUSIONS

Most ND280 analyses use the TPC particle identification with the measured charge deposit. The TPC PID has been checked for μ^+ selection. Cuts used for the current analysis are well optimised but some minor improvements are possible. With the additional information from the ECAL detector one can further suppress backgrounds from π^+ and protons misidentified as μ^+.

ACKNOWLEDGMENTS

This work was partially supported by the Polish National Science Centre (project 2014/14/M/ST2/00850).

REFERENCES

1. K. Abe *et al.* [T2K Collaboration], "The T2K Experiment," Nucl. Instrum. Meth. A **659**, 106 (2011).
2. K. Abe *et al.* [T2K Collaboration], "Combined Analysis of Neutrino and Antineutrino Oscillations at T2K," Phys. Rev. Lett. **118**, no.15, 151801 (2017).
3. Y. Hayato, "A neutrino interaction simulation program library NEUT," Acta Phys. Polon. B **40**, 2477 (2009).
4. L. Magaletti, "Measurement of $\bar{\nu}_\mu$ CC interactions with the ND280 detector of the T2K experiment," Eur. Phys. J. Plus **130**, no.8, 167 (2015).

Searching for neutrinoless double beta decay with scintillating bolometers: the CUPID-Mo experiment

A. Zolotarova on behalf of the EDELWEISS and CUPID-Mo collaborations

IRFU, CEA, Universite Paris-Saclay, F-91191 Gif-sur-Yvette, France

Abstract. The observation of neutrinoless double beta ($0\nu2\beta$) decay would confirm the lepton number violation and would give us answers to questions as the nature (Dirac or Majorana) and the absolute mass scale of the neutrinos. The LUMINEU project has developed a mature technology of $Li_2^{100}MoO_4$ scintillating bolometers to search for $0\nu2\beta$ decay. The results, obtained in multiple tests, demonstrated a well reproducible detector technology with high performance and radiopurity. In run, performed with 4 enriched crystals (0.2 kg each) with an exposure of 0.04 kg×y of ^{100}Mo we obtained the most precise half-life value for $2\nu2\beta$ decay mode of ^{100}Mo: $T_{1/2}^{2\nu2\beta} = (6.92 \pm 0.06(\text{stat}) \pm 0.36(\text{syst})) \times 10^{18}$ y. Reasonably high sensitivity to the $0\nu2\beta$ decay was achieved ($\lim T_{1/2}^{0\nu2\beta} = 0.7 \times 10^{23}$ y) even with considerably low statistics (0.06 kg×y). In the framework of the CUPID-Mo experiment, which follows the successfully accomplished LUMINEU R&D, the measurement will be performed with 20 $Li_2^{100}MoO_4$ crystals. The goals for a six-months run are: obtaining 0-background in the region of interest and demonstrating the applicability of $Li_2^{100}MoO_4$ scintillating bolometer technology for a ton-scale follow-up of the CUORE experiment, named CUPID.

Keywords: double beta decay, scintillating bolometers, ^{100}Mo, $Li_2^{100}MoO_4$, enriched materials
PACS: 23.40.-s; 29.40.Mc; 29.40.Vj

INTRODUCTION

The neutrinoless double beta ($0\nu2\beta$) decay is a hypothetical nuclear transition, where two neutrons are simultaneously transformed into two protons with the emission of two electrons and no other particles [1]. The detection of this process would prove the lepton number violation and determine the Majorana nature of neutrino (neutrinos are equal to antineutrinos). Such features would clearly demonstrate new physics beyond the Standard Model (SM). In addition its observation would allow to define the absolute neutrino mass scale and give information about the mass hierarchy. This process has great interest not only for neutrino physics, but but also for understanding the origin of matter-antimatter asymmetry (see [1, 2] and references therein). The current most stringent lower limits for the $0\nu2\beta$ decay half-life are $T_{1/2}^{0\nu2\beta} > 10^{24} - 10^{26}$ y [1].

Another mode of this transition is two-neutrino double beta ($2\nu2\beta$) decay which is allowed by SM and energetically possible for 35 nuclei. Experimentally it has been measured in 11 nuclei. $2\nu2\beta$ decay is the rarest observed nuclear transition with a half-life range of $T_{1/2}^{2\nu2\beta} \approx 10^{18} - 10^{24}$ y [1].

Numerous projects are developing technologies for the next-generation $0\nu2\beta$ decay experiments with the goal to cover completely the inverted hierarchy region of the neutrino mass scale. One of the most promising methods is the bolometric approach [4]. Among various bolometric experiments there is CUORE (Cryogenic Underground Observatory for Rare Events), searching for $0\nu2\beta$ decay in ^{130}Te with TeO_2 bolometers [5]. It is the first ton-scale cryogenic $0\nu2\beta$ decay experiment currently running and it will be operated during several years. When the CUORE data-taking will be accomplished, the follow-up program, named CUPID (CUORE Upgrade with Particle IDentification) is planned with the use of enriched material and improved background with respect to the current configuration [6, 7]. ^{82}Se, ^{130}Te, ^{116}Cd and ^{100}Mo are considered as favourable candidates. Several demonstrator projects are ongoing with the goal to provide the best technology for CUPID.

Among these projects there is CUPID-Mo, described in this article, investigating the ^{100}Mo isotope with scintillating bolometer technology. The choice of this isotope is driven by the following advantages: favorable theoretical predictions on the half-life; possibility of enrichment in a large amount (by gas centrifugation); high transition energy ($Q_{\beta\beta}$ = 3034 keV), which is beyond the endpoint of the natural γ radioactivity (2615 keV), resulting in significantly reduced background in the region of interest.

A scintillating bolometer consists of an energy absorber (dielectric crystal) linked to a temperature sensor and coupled to a light detector. The signal from the absorber, collected at very low temperatures (around 10-20 mK), consists of a thermal pulse. Its amplitude is proportional to the energy deposited by a particle inside the crystal. If the source is embedded in the absorber, the so-called "source=detector" approach allows to significantly increase the efficiency ($\approx$100%). The scintillation light allows to discriminate α particles from γ/β band: for the same deposited energy, the amount of the emitted light is different for α and γ/β events.

The scintillating crystals to be operated as bolometers in the CUPID-Mo demonstrator are based on the compound $Li_2^{100}MoO_4$, equipped with NTD (Neutron Transmutation Doped) thermistors and coupled to Ge light detectors [8].

LUMINEU R&D

LUMINEU (Luminescent Underground Molybdenum Investigation for NEUtrino mass and nature) is a French-funded R&D project, performed during 2012-2017. In the framework of this project, the protocol of crystal production was developed, including Mo purification, optimization of the crystal growth and a program to control the content of ^{40}K (<5 mBq/kg). Grown crystals have uniform high optical quality, crystal yield and radiopurity [9] with possibility to enlarge the production rates, if required for a ton-scale experiment.

Multiple tests of $Li_2^{100}MoO_4$ scintillatig bolometers were performed in the EDELWEISS setup, located in the Laboratiore Souterrain de Modane (LSM), France [10].

As the background suppression is a crucial point for $0\nu2\beta$ decay experiments, special attention to material selection and assembly procedures was required to minimize the radioactive contamination of the detectors [4]. Each component, used for the assembly of the bolometers, was tested by HPGe detectors, checking the radioactivity levels. Light

detectors are made of disk-shaped ultrapure Ge crystals (44 mm in diameter and 0.17–0.3 mm thickness) supplied by UMICORE (Belgium). For the detector holders NOSV copper was used for its good thermal and mechanical properties, low hydrogen content and high radiopurity. As the surface contamination can also make a significant contri-

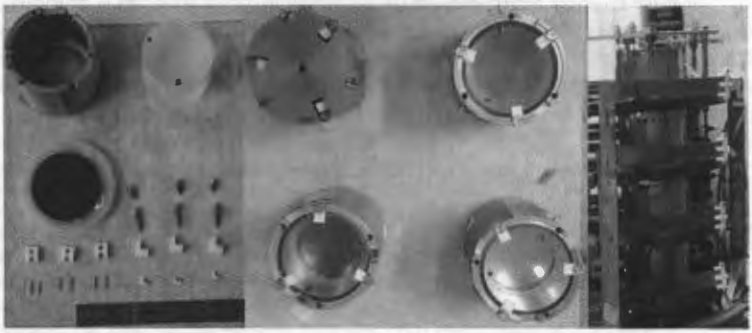

FIGURE 1. Elements, required to assemble one scintillating bolometer with $Li_2^{100}MoO_4$ crystal (left), and suspended tower inside the EDELWEISS cryostat(right). Suspension is used to suppress the microphonic noise. Such detector design will be used also for the CUPID-Mo demonstrator.

bution to the total background, a special cleaning procedure was established: all copper elements were treated with the commercial solution "micro-90"(produced by Sigma-Aldrich, [11]) in order to remove any kind of grease or oil (which are used during the machining of the elements) from the surface. Then the elements were etched using citric acid, removing about 15-20 micron of surface layer and eliminating possible radioactive contaminants, implanted in the surface. Such treatment allowed us to perform also copper surface passivation, making copper less reactive to environment and resistant to corrosion.

The PTFE spacers (see Fig. 1) were the only mechanical elements that have direct contact with the crystal, working as decoupling from the thermal bath. For PTFE elements and springs of the tower suspension a procedure of cleaning with ethanol in an ultrasonic bath was applied. The assembly procedure was performed in clean room environment.

Before and after the cryogenic runs, the enriched elements are kept under N_2 flux in LSM to avoid cosmogenic activation [4] and $Li_2^{100}MoO_4$ crystals have been brought to sea level only to perform the assembly of the detectors.

All multiple tests on natural and enriched crystals [8], including measurements with a four $Li_2^{100}MoO_4$ scintillating bolometer array, were highly successful: detectors demonstrated uniform high energy resolution, high level of radiopurity and full $\alpha/\gamma(\beta)$ separation, meeting the requirements for CUPID-Mo demonstrator (see Table 1). The LUMINEU R&D provides a mature technology of scintillating bolometers, suitable for mass production for future ton-scale experiment.

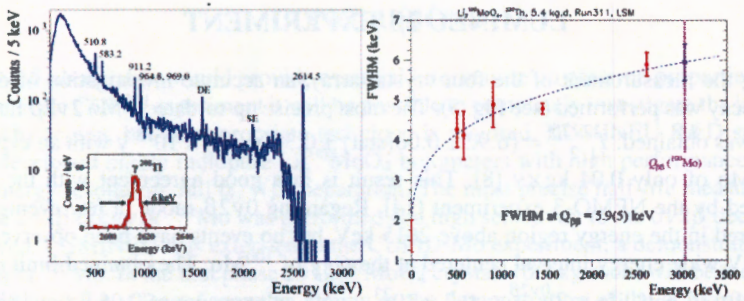

FIGURE 2. Energy spectrum of the ^{232}Th calibration (left) and energy dependence of the FWHM energy resolution (right) measured by a four-bolometer array.

TABLE 1. Performance of four $Li_2^{100}MoO_4$ scintillating bolometers in the underground run.

	$Li_2^{100}MoO_4$	crystal #		
	1	2	3	4
Crystal's mass, g	186	204	213	207
FWHM, keV at 2615 keV	5.8±0.6	5.7±0.6	5.5±0.5	5.7±0.6
LY, keV/MeV	0.41	0.38	0.73	0.74
α/β separation	9σ	9σ	14σ	14σ
Activity of ^{228}Th, μBq/kg	≤4	≤6	≤3	≤5
Activity of ^{226}Ra, μBq/kg	≤6	≤11	≤3	≤9

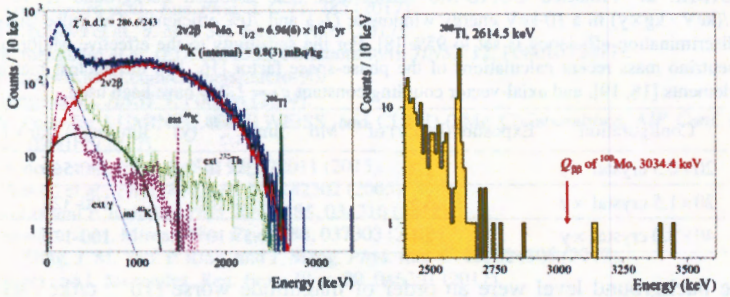

FIGURE 3. Left panel: The $\gamma(\beta)$ energy spectrum accumulated over 0.04 kg×y with fit by a simple model constructed from a distribution of the $2\nu2\beta$ decay of ^{100}Mo ($2\nu2\beta$) and other contributions of γ/β backgrounds. The $2\nu2\beta$ signal-to-background ratio above 1.5 MeV is 10:1. Right panel: The energy spectrum of (γ) events in the vicinity of $0\nu2\beta$ decay of ^{100}Mo extracted from the 0.11 kg×y background measurements [13].

LUMINEU 2β EXPERIMENT

During the measurement of the four crystal array, an accurate investigation of double beta decay was performed (see Fig. 3). The most precise up-to-date ^{100}Mo $2\nu2\beta$ half-life value was obtained: $T_{1/2}^{2\nu2\beta} = (6.92 \pm 0.06(\text{stat}) \pm 0.36(\text{syst})) \times 10^{18}$ y with an exposure of ^{100}Mo of only 0.04 kg×y [8]. This result is in a good agreement with the value obtained by the NEMO-3 experiment [14]. Regarding $0\nu2\beta$ mode, a few events were registered in the energy region above 2615 keV, but no events have been observed in a 200-keV-wide energy interval centered at the $Q_{\beta\beta}$ of ^{100}Mo. The obtained limit on the ^{100}Mo $0\nu2\beta$ half-life is $T_{1/2}^{0\nu2\beta} > 0.7 \times 10^{23}$ y with an exposure of 0.06 kg×y [8]. This limit is about one order of magnitude weaker than the NEMO-3 result(1.1×10^{24} [15]), however it was achieved over a factor 600 shorter exposure.

CUPID-MO

The successfully accomplished LUMINEU R&D is going to be extended to a CUPID-Mo $0\nu2\beta$ demonstrator with 5 kg of ^{100}Mo. In the first phase, the 20 $Li_2^{100}MoO_4$ crystals (⊘ 44×45 mm, ≈0.2 kg each, 2.34 kg of ^{100}Mo), assembled in five suspended towers, will be operated in the EDELWEISS set-up during 2018 at least for 6 months.

In Tab. 2 the projected CUPID-Mo sensitivities (90% C.L.) are listed with different configurations of the experiment. These sensitivities can be compared with the most stringent limits on the effective Majorana mass (60-600 meV), obtained by the most sensitive $0\nu2\beta$ experiments of current generation with typical exposures of 10-100 kg×y [1].

TABLE 2. Projected CUPID-Mo sensitivities. The assumed background is 10^{-3} c/(keV×kg×y) in a 10-keV energy window at $Q_{\beta\beta}$ and 70% efficiency. The pulse shape discrimination efficiency is set to 95% [8]. For the sensitivity to the effective Majorana neutrino mass recent calculations of the phase-space factor [16, 17], the nuclear matrix elements [18, 19], and axial-vector coupling constant $g_A = 1.269$ have been used.

Configuration	Exposure (kg×y) of ^{100}Mo	lim $T_{1/2}^{0\nu2\beta}$ (y)	lim $\langle m_{\beta\beta} \rangle$ (meV)
20×0.5 crystal ×y	1.2	1.3×10^{24}	330-560
20×1.5 crystal ×y	3.5	4.0×10^{24}	190-320
40×3.0 crystal ×y	14	1.5×10^{24}	100-170

If the background level were an order of magnitude worse (10^{-2} c/(keV×kg×y)), the sensitivity of CUPID-Mo phase I (20×0.5 crystal) would not change essentially. According to these calculations, the CUPID-Mo demonstrator can achieve significant physics results despite its relatively small scale.

CONCLUSIONS

The $0\nu2\beta$ observation would provide essential information on neutrino properties. With the ton-scale CUPID experiment it will be possible to completely investigate the inverted hierarchy region, but an appropriate technique is required. LUMINEU R&D successfully developed highly radiopure $Li_2^{100}MoO_4$ bolometers with high performance: a few keV energy resolution, full $\alpha/\gamma(\beta)$ separation. The most precise half-life measurement for the $2\nu2\beta$ decay of ^{100}Mo was performed and high sensitivity to the $0\nu2\beta$ decay was achieved. LUMINEU was extended to the CUPID-Mo experiment, a demonstrator with ≈ 5 kg of ^{100}Mo. In the first phase 20 $Li_2^{100}MoO_4$ crystals (0.2 kg each) will be measured underground for at least 6 months, aiming at the demonstration of the applicability of $Li_2^{100}MoO_4$ scintillating bolometer technology for CUPID.

ACKNOWLEDGMENTS

This work is supported by the "IDI 2015" project funded by the IDEX Paris-Saclay, ANR-11-IDEX-0003-02.

REFERENCES

1. J. D. Vergados, H. Ejiri, and F. Simkovic, *Int. J. Mod. Phys E* **25**, 1630007 (2017).
2. S. Dell'Oro, S. Marcocci, M. Viel, F. Vissani, *AHEP* **2016**, 2162659 (2016).
3. V.I. Tretyak and Yu.G. Zdesenko, *At. Data Nucl. Data Tables* **80**, 83 (2002).
4. D. Poda, A. Giuliani, *Int. J. Mod. Phys A* **32**, 1743012 (2017).
5. C. Alduino et. al. (CUORE collaboration), arXiv:1710.07988 [nucl-ex] (2017).
6. G. Wang et. al. (CUPID interest group), arXiv:1504.03599 physics.ins-det] (2015).
7. G. Wang et. al. (CUPID interest group), arXiv:1504.03612 physics.ins-det] (2015).
8. E. Armengaurd et al., *Eur. Phys. J. C* **77**, 785 (2017) .
9. V. Grigorieva et al., *J. Mat. Sci. Eng. B* **7**, 63 (2017).
10. E. Armengaurd et al. (EDELWEISS Collaboration), *JINST* **12**, P08010 (2017).
11. https://www.ipcol.com/cleaners/micro-90.
12. L. Berge et al., *JINST* **9**, P06004 (2014).
13. D.V. Poda for LUMINEU, EDELWEISS, and CUPID-0/Mo Collaborations, *AIP Conf. Proc.* **25**, 1894, 020017 (2017).
14. R. Arnold et al., *Phys. Rev. D* **92**, 072011 (2015).
15. R. Arnold et al., *Phys. Rev. Lett.* **95**, 182302 (2005).
16. J. Kotila and F. Iachello, *Phys. Rev. C* **85**, 034316 (2012).
17. S. Stoica and M. Mirea, *Phys. Rev. C* **88**, 037303 (2013).
18. L. S. Song, J. M. Yao, P. Ring, and J. Meng, *Phys. Rev. C* **95**, 024305 (2017).
19. J. Engel and J. Menendez, *Rep. Prog. Phys.* **80**, 046301 (2017).

AGENDA

Pontecorvo School 2017 – Agenda

Date	Lecture 1 9:00 - 10:30	Lecture 2 11:00 - 12:30	Lecture 3 14:00 - 15:30	Lecture 4 16:00 - 17:30
Su 20.8.	**Arrival; 18:30 - Welcome party; 19:00 – Dinner**			
Mo 21.8.	**Samoil Bilenky** *Introduction to Neutrino*	**Boris Kayser** *Neutrino oscillation phenomenology - I*	**Gary Feldman** *Long baseline neutrino oscillation experiments- I*	**Alexei Smirnov** *Solar Neutrinos: Theory and Experiments*
Tu 22.8.	**Barry Barish** *Observation of gravitational waves - I*	**Boris Kayser** *Neutrino oscillation phenomenology - II*	**Gary Feldman** *Long baseline neutrino oscillation experiments- II*	**Igor Tkachev** *Measuring of neutrino mass with tritium beta decay*
We 23.8.	**Barry Barish** *Observation of gravitational waves - II*	**Steve King** *Theory of neutrino masses and mixing - I*	**Steve King** *Theory of neutrino masses and mixing - II*	**Yifang Wang** *Oscillations of reactor neutrinos -I*
Th 24.8.	**Excursion and free time**			
Fr 25.8.	**Yifang Wang** *Oscillations of reactor neutrinos -II*	**Carlo Giunti** *Oscillations beyond 3 neutrino mixing*	**Jonathan Link** *Hunting for a sterile neutrino - I*	**Nicolao Fornengo** *Dark matter theory and experiments*
Sa 26.8.	**Jonathan Link** *Hunting for a sterile neutrino - II*	**Gianpiero Mangano** *Neutrino properties from cosmology - I*	**Gianpiero Mangano** *Neutrino properties from cosmology - II*	**Sacha Davidson** *Leptogenesis*
Su 27.9.	**Free day**			

Mo 28.8.	**Loredana Gastaldo** *Measuring of neutrino mass with EC of holmium*	**Alexander Barabash** *Neutrinoless double beta decay experiments -I*	**Christian Spiering** *Neutrino telescopes - I*	**Irene Tamborra** *Supernova neutrinos*
Tu 29.8.	**Alexander Barabash** *Neutrinoless double beta decay experiments -II*	**Petr Vogel** *Double beta decay NMEs*	**Christian Spiering** *Neutrino telescopes - II*	**David van Dyk** *Statistical quantification of discovery in neutrino physics - I*
We 30.8.	**Jan Sobczyk** *Neutrino-nucleus interactions-I*	**Petr Vogel** *Spectra of neutrinos from reactor*	**Eckhard Elsen** *Neutrino physics at CERN*	**David van Dyk** *Statistical quantification of discovery in neutrino physics - II*
Th 31.8.	**Alain Blondel** *Future Colliders*	**Jan Sobczyk** *Neutrino-nucleus interactions - II*	**Students presentations**	**Students presentations** **and** **Final panel discussion session**
Fr 1.9.	**Departure**			

Daily timetable

7:00-9:00		14:00-17:30
Breakfast	12:30-14:00	Afternoon sessions
9:00-12:30	Lunch	15:30-16:00
Morning session	Starting 18:30	Coffee break
10:30-11:00	Free time	17:30-18:30
Coffee break		Dinner

LIST OF PARTICIPANTS

List of Participants

Lecturers

1. Alexander Barabash (ITEP, Moscow)
2. Barry Barish (Caltech, Pasadena)
3. Samoil Bilenky (JINR, Dubna)
4. Alain Blondel (Univ. of Geneva)
5. Sacha Davidson (IPN de Lyon)
6. David A. van Dyk (Imperial College, London)
7. Eckhard Elsen (CERN, Geneva)
8. Gary Feldman (Harvard Univ., Cambridge)
9. Nicolao Fornengo (Univ. of Torino/INFN, Torino)
10. Loredana Gastaldo (Kirchhoff Inst. for Physics, Heidelberg)
11. Carlo Giunti (INFN, Torino)
12. Boris Kayser (Fermilab, Batavia)
13. Steve King (Univ. of Southampton)
14. Jonathan Link (Virginia Tech, Blacksburg)
15. Gianpiero Mangano (INFN, Naples)
16. Alexei Smirnov (MPI, Heidelberg)
17. Jan T. Sobczyk (Wrocław Univ.)
18. Christian Spiering (DESY, Zeuthen)
19. Irene Tamborra (Niels Bohr Inst., Univ. of Copenhagen)
20. Igor Tkachev (INR, Moscow)
21. Petr Vogel (Caltech, Pasadena)
22. Yifang Wang (IHEP, Beijing)

Students and young scientists

1. Allakhverdyan, Vladimir (JINR, Dubna)
2. Almazan, Helena (MPI, Heidelberg)
3. Antoshkina, Tatiana (JINR, Dubna)
4. Babič, Andrej (Czech Technical Univ., Prague)
5. Bardacova, Zuzana (Comenius Univ., Bratislava)
6. Bolshakova, Anastasia (JINR, Dubna)
7. Bormotova, Iryna (Silesian Univ., Opava)
8. Boschi, Tommaso (IPPP, Univ. of Durham)
9. Bourbeau, Etienne (Niels Bohr Inst., Univ. of Copenhagen)
10. Brunst, Tim (MPP, Munich)
11. Budaca, Radu (IFIN-HH, Bucharest)
12. Bulmus, Taygun (Mimar Sinan Fine Arts Univ., Istanbul)

13. Caracas, Ioana Alexandra (JINR, Dubna / Faculty of Physics, Univ. of Bucharest)
14. Čarný, Peter (Comenius Univ., Bratislava)
15. Centelles Chuliá, Salvador (Inst. de Física Corpuscular, Paterna)
16. Cervenkov, Daniel (Charles Univ., Prague)
17. Chen, Yifan (Univ. of Bern)
18. Cheng, Yaping (IKP-2, Forschungszentrum Jülich, Jülich / IHEP, Beijing)
19. Doering, Christian (MPI, Heidelberg)
20. Dohnal, Tadeáš (Charles Univ., Prague)
21. Dvořák, Martin (Charles Univ., Prague)
22. Dvornický, Rastislav (JINR, Dubna)
23. Fajt, Lukáš (IEAP CTU, Prague)
24. Fazliakhmetov, Almaz (MIPT, Moscow)
25. Fomina, Maria (JINR, Dubna)
26. Francois, Conor (Univ. of Bern)
27. Guo, Wan-Lei (IHEP, Beijing)
28. Inácio, Ana Sofia (LIP, Lisbon)
29. Kerényi, Peter (Comenius Univ., Bratislava)
30. Khan, Amir Nawaz (SYSU, Guangzhou)
31. Kowal, Beata (Univ. of Wrocław)
32. Lin, Heng (SJTU, Shanghai)
33. Macko, Miroslav (IEAP CTU, Prague/Comenius Univ., Bratislava/Univ. de Bordeaux)
34. *Mamedov, Fadahat (Czech Technical Univ., Prague)*
35. Mantegazzini, Federica (Heidelberg Univ., Kirchhoff Inst. for Physics, Heidelberg)
36. Miloradovic, Michael (Univ. of Zurich)
37. Mora Lepin, Luis Alberto (Pontificia Univ. Católica de Chile, Santiago)
38. Mosu, Toma Stefan (IFIN-HH, Bucharest)
39. Nae, Ştefan-Alexandru (LIP, Lisbon/ FCUL, Univ. de Lisboa)
40. Naumov, Dmitry (JINR, Dubna)
41. Navas Nicolás, Diana (CIEMAT, Madrid)
42. Nitescu, Ovidiu Vasile (IFIN-HH, Bucharest)
43. Oliviero, Guillaume (LPC, Caen)
44. Palušová, Veronika (Comenius Univ., Bratislava)
45. Parvu, Mikaela (Univ. of Bucharest)
46. Pestel, Valentin (LPC, Caen)
47. Ponomarev, Dmitrii (JINR, Dubna)
48. Roca, Christian (MPI, Heidelberg)
49. Rong, Shu-jun (Shaanxi Univ. of Technology, Hanzhong)

50. Rozov, Sergey (JINR, Dubna)
51. Rozova, Irina (JINR, Dubna)
52. Rukhadze, Ekaterina (CTU, Prague)
53. Sicking, Philipp (Technische Univ., Dortmund)
54. Sinská, Zuzana (Comenius Univ., Bratislava)
55. Smetana, Adam (CTU, Prague)
56. Smejkal, Jaroslav (CTU, Prague)
57. Suvorov, Sergey (INR RAS, Moscow)
58. Terasaki, Jun (CTU, Prague)
59. Tmej, Tomáš (Charles Univ., Prague)
60. Treskov, Konstantin (JINR, Dubna)
61. Vishneva, Alina (JINR, Dubna)
62. Wagaarachchi, Sachinthya Lapalu (Univ. of California, Berkeley)
63. Xie, Fang (Univ. College London)
64. Żarnecki, Grzegorz (NCBJ, Otwock)
65. Zolotarova, Anastasiia (IRFU, CEA, Saclay)

Organizing committee

1. Ivan Štekl (IEAP CTU, Prague)
2. Rupert Leitner (Charles U., Prague)
3. Alexander Olshevsky (INR, Dubna)
4. Fedor Šimkovic (Comenius U., Bratislava/JINR, Dubna)
5. Elena Kolganova (JINR, Dubna)

Научное издание

VII INTERNATIONAL PONTECORVO NEUTRINO PHYSICS SCHOOL

Proceedings of Student Poster Session

VII МЕЖДУНАРОДНАЯ ШКОЛА ПО ФИЗИКЕ НЕЙТРИНО ИМ. Б. М. ПОНТЕКОРВО

Труды студенческой постерной сессии

Ответственная за подготовку сборника к печати *А. В. Малых*.

Сборник отпечатан методом прямого репродуцирования с оригиналов, предоставленных оргкомитетом.

E1,2,4-2018-10

Подписано в печать 30.03.2018.
Формат 60×90/16. Бумага офсетная. Печать офсетная.
Усл. печ. л. 13,13. Уч.-изд. л. 20,69. Тираж 135 экз. Заказ 59354.

Издательский отдел Объединенного института ядерных исследований
141980, г. Дубна, Московская обл., ул. Жолио-Кюри, 6.
E-mail: publish@jinr.ru
www.jinr.ru/publish/